Technical University of Munich

Liquid Scintillator Studies for the JUNO Neutrino Experiment

Nonlinear Energy Response and Radiopurity

Konstantin Josef Schweizer

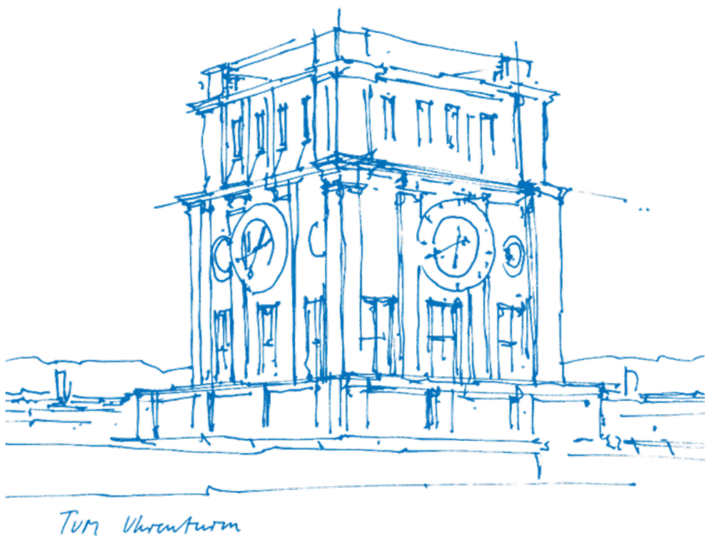

TUM School of Natural Sciences
Technische Universität München

Liquid Scintillator Studies for the JUNO Neutrino Experiment

Nonlinear Energy Response and Radiopurity

Konstantin Josef Schweizer

Vollständiger Abdruck der von der TUM School of Natural Sciences der Technischen Universität München zur Erlangung des akademischen Grades eines

Doktors der Naturwissenschaften (Dr. rer. nat.)

genehmigten Dissertation.

Vorsitz:
Prof. Dr. Alejandro Ibarra

Prüfer der Dissertation:
1. Prof. Dr. Lothar Oberauer
2. apl. Prof. Dr. Hubert Kroha

Die Dissertation wurde am 31.10.2024 bei der Technischen Universität München eingereicht und durch die TUM School of Natural Sciences am 28.11.2024 angenommen.

It is difficult to get a man to understand something, when his salary depends on his not understanding it.

- Upton Sinclair

Abstract

This thesis investigates two critical properties of liquid scintillators (LSs) in the context of the Jiangmen Underground Neutrino Observatory (JUNO): the nonlinearity of the light yield and the radiopurity. JUNO is a $20\,\mathrm{kton}$ liquid scintillator experiment designed primarily to determine the neutrino mass ordering. JUNO will measure the energy spectrum of electron antineutrinos from nearby nuclear power plants with unprecedented accuracy, which requires an excellent energy resolution and a detailed understanding of the LS properties.

The first part of this work addresses the uncertainty in Birks' constant (kB), a key parameter in modeling the nonlinear energy response function of scintillators. With a table-top experiment, I confirmed the spectral shape of the nonlinearity for electron energies between 10 - $180\,\mathrm{keV}$. Due to the smallness of the nonlinear effect, its quantitative determination is challenging and dominated by systematic uncertainties. I identified significant spatial inhomogeneities in the charge collection of the employed setup, varying by more than $10\,\%$. These inhomogeneities can likely explain the large uncertainties of $kB = 0.0111\,\mathrm{cm/MeV}$ to $0.0252\,\mathrm{cm/MeV}$ values observed in previous studies. Experiencing similar challenges, the results of other experimental groups fall in the same range. The fact that no convincing result exists yet underscores the need for improved experimental setups for future measurements.

The second part of the thesis is done in the framework of OSIRIS, the large-scale pre-detector built to ensure the radiopurity of JUNO's LS. The OSIRIS detector will measure the radiopurity of the LS one last time after all purification steps and just before filling it into the JUNO detector. I managed and developed the analysis framework for OSIRIS, which monitors scintillator purity in real-time by detecting so-called BiPo coincidences from the long-lived decay chain from ^{238}U.

Furthermore, I performed the first pulse shape discrimination (PSD) study on the JUNO scintillator in OSIRIS, showing that discrimination between α- and β-particles can achieve up to $70\,\%$ efficiency. Moreover, I analyzed the first data acquired by OSIRIS, showing the temporal evolution of the measured rates of BiPo and ^{210}Po decays in response to detector operations like LS circulations. I found - under the assumption of secular equilibrium - the measured ^{238}U and ^{210}Po mass concentrations w.r.t. to the LS mass to be $(1.1 \pm 0.4) \cdot 10^{-14}$ g/g and $(7 \pm 1) \cdot 10^{-23}$ g/g, respectively. These results are approximately one order of magnitude over the JUNO specifications for accidental events. For the very first time, I showed that the correlated background from ^{210}Po inducing $^{13}\mathrm{C}(\alpha, n)^{16}\mathrm{O}$ reactions contribute at most at the $1\,\%$-level to the antineutrino spectrum.

However, the latest data sets of OSIRIS using a fiducial volume cut and a different radiopurity measurement method (neutron activation analysis) determine an upper limit on the ^{238}U contamination to be close to $1 \times 10^{-15}\,\mathrm{g/g}$ suggesting that the OSIRIS background levels limit the detector's sensitivity. This thesis highlights the identification of potential instrumental limitations, enabling timely adjustments to the research strategy.

Zusammenfassung

Diese Arbeit untersucht zwei entscheidende Eigenschaften von Flüssigszintillatoren (LS) im Zusammenhang mit dem Jiangmen Underground Neutrino Observatory (JUNO): die Nichtlinearität der Lichtausbeute und die radioaktive Reinheit. JUNO ist ein Flüssigszintillator-Experiment mit einer Kapazität von 20 kton, das in erster Linie der Bestimmung der Neutrinomassenordnung dient. JUNO wird das Energiespektrum von Elektron-Antineutrinos aus nahe gelegenen Kernkraftwerken mit bisher unerreichter Genauigkeit messen, was eine hervorragende Energieauflösung und ein detailliertes Verständnis der Eigenschaften des Flüssigszintillators erfordert.

Der erste Teil dieser Arbeit befasst sich mit der Unsicherheit der Birks-Konstante (kB), einem Schlüsselparameter bei der Modellierung der nichtlinearen Energieantwort von Szintillatoren. Mit einem experimentallen Aufbau habe ich die spektrale Form der Nichtlinearität für Elektronenenergien zwischen 10 - 180 keV bestätigt. Aufgrund der geringen Auswirkung des nichtlinearen Effekts ist seine quantitative Bestimmung herausfordernd und wird von systematischen Unsicherheiten dominiert. Ich habe erhebliche räumliche Inhomogenitäten in der Ladungssammlung des verwendeten Aufbaus identifiziert, die um mehr als $10\,\%$ variieren. Diese Inhomogenitäten können wahrscheinlich die großen Unsicherheiten von $kB = 0.0111 - 0.0252\,$cm/MeV erklären, die in früheren Studien beobachtet wurden. Unter ähnlichen Herausforderungen leidend fallen die Ergebnisse anderer experimenteller Gruppen in denselben Bereich. Die Tatsache, dass es noch kein überzeugendes Ergebnis gibt, unterstreicht den Bedarf an verbesserten Versuchsaufbauten für zukünftige Messungen.

Der zweite Teil der Arbeit wird im Rahmen von OSIRIS durchgeführt, dem groß angelegten Vordetektor, der die radioaktive Reinheit des LS von JUNO zu gewährleisten soll. Der OSIRIS-Detektor wird die radioaktive Reinheit des LS ein letztes Mal nach allen Reinigungsschritten und kurz vor dem Einfüllen in den JUNO-Detektor messen. Ich leitete und entwickelte das Analysesystem für OSIRIS, das die Reinheit des Szintillators in Echtzeit überwacht, indem es die sogenannte BiPo-Koinzidenzen aus der langlebigen Zerfallskette von ^{238}U detektiert.

Außerdem habe ich die erste Studie zur Pulsformunterscheidung (PSD) mit dem JUNO-Szintillator in OSIRIS durchgeführt und gezeigt, dass die Unterscheidung zwischen α- and β-Teilchen bis zu $70\,\%$ Effizienz erreichen kann. Darüber hinaus habe ich die ersten von OSIRIS aufgenommenen Daten analysiert, die die zeitliche Entwicklung der gemessenen Raten der BiPo- und ^{210}Po -Zerfälle als Reaktion auf Detektoroperationen wie LS-Zirkulationen zeigen. Ich bestimmte - unter der der Annahme eines säkularen Gleichgewichts - die gemessenen ^{238}U- und ^{210}Po-Massenkonzentrationen im Verhältnis zur LS-Masse zu $(1.1 \pm 0.4) \cdot 10^{-14}$ g/g bzw. $(7 \pm 1) \cdot 10^{-23}$ g/g. Diese Ergebnisse liegen etwa eine Größenordnung über den JUNO-Spezifikationen für zufällige Hintergrundereignisse. Als Erster habe ich gezeigt, dass der korrelierte Hintergrund von ^{210}Po , der $^{13}\mathrm{C}(\alpha, n)^{16}\mathrm{O}$-Reaktionen induziert, höchstens mit $1\,\%$ zum Antineutrinospektrum beiträgt.

Die neuesten Datensätze von OSIRIS zusammen mit einer Volumenrestriktion und eine andere Methode (Neutronenaktivierungsanalyse) zur Messung der radioaktive Reinheit bestimmen jedoch eine obere Grenze der ^{238}U -Kontamination zu ca. $1 \times 10^{-15}\,$g/g, was darauf hindeutet, dass die OSIRIS-Untergrundereignisse die Empfindlichkeit des Detektors begrenzen. Diese Arbeit hebt die Identifizierung potenzieller instrumenteller Beschränkungen hervor und ermöglichte rechtzeitige Anpassungen der Forschungsstrategie.

Contents

Chapter 1

Neutrino Physics

Neutrino physics has become one of the most dynamic and intriguing research areas in modern particle physics. Neutrinos are elusive, nearly massless particles that interact with matter so weakly that they are incredibly difficult to detect. Despite being the least understood particles within the Standard Model (SM) of particle physics, they play a crucial role in unraveling some of the universe's deepest mysteries.

After discovering the neutrino, the Standard Electroweak Model, introduced by Weinberg and Salam in 1967, provided a theoretical framework to describe the interactions of fundamental particles with remarkable precision. Within this model, neutrinos are classified as uncharged leptons, existing in three distinct flavors—electron neutrinos (ν_e), muon neutrinos (ν_μ), and tau neutrinos (ν_τ)—each paired with their respective charged leptons. According to the SM, neutrinos are massless, exist only as left-handed particles and right-handed antiparticles, and interact solely through gravity and the weak force.

However, groundbreaking experiments like Super-Kamiokande and the Sudbury Neutrino Observatory (SNO) have challenged these long-held assumptions. These experiments revealed that neutrinos can oscillate, or change, between their flavors as they travel through space. This phenomenon, known as neutrino oscillation, provides clear evidence that neutrinos possess mass - an insight that contradicts the original predictions of the SM. This discovery signifies that neutrinos may be the key to unlocking new physics beyond the SM, a tantalizing possibility that has excited experimentalists and theorists.

The fact that neutrinos can oscillate between flavors implies the existence of mass differences among the neutrino types and, more broadly, suggests that our current understanding of particle physics is incomplete. This opens the door to questions that touch on some of the most profound areas of physics, such as the nature of dark matter, the matter-antimatter asymmetry in the universe, and whether neutrinos could help reveal new forces or particles.

In essence, neutrinos represent a potential "portal" to new physics, providing a unique opportunity to explore phenomena that lie beyond the scope of the SM. Their mysterious behavior has made them a focal point in the search for answers to fundamental questions about the universe.

1.1 Neutrino Oscillations

Neutrino oscillations are the effect that neutrinos can oscillate between flavors. The oscillation probability depends on their energy and distance traveled. This happens because the mass eigenstates - the eigenstates of the free Hamiltonian - of neutrinos differ from their flavor eigenstates, meaning the eigenstates w.r.t. the weak interaction [1, 2]. Let ν_e, ν_μ and ν_τ be the flavor eigenstates and ν_1, ν_2 and ν_3 the mass eigenstates. We can then write [3]:

$$\begin{pmatrix}\nu_e\\ \nu_\mu\\ \nu_\tau\end{pmatrix} = U \begin{pmatrix}\nu_1\\ \nu_2\\ \nu_3\end{pmatrix} = \underbrace{\begin{pmatrix}U_{e1} & U_{e2} & U_{e3}\\ U_{\mu 1} & U_{\mu 2} & U_{\mu 3}\\ U_{\tau 1} & U_{\tau 2} & U_{\tau 3}\end{pmatrix}}_{\text{PMNS-matrix}} \begin{pmatrix}\nu_1\\ \nu_2\\ \nu_3\end{pmatrix} \tag{1.1}$$

The unitary matrix U is called the Pontecorvo-Maki-Nakagawa-Sakata-(PMNS-) matrix [4]. Using a parametrization with three mixing angles θ_{12}, θ_{13} and θ_{23} and a CP-violating phase δ [3]. Then, the PMNS-matrix becomes [3]:

$$U = \begin{pmatrix} 1 & 0 & 0 \\ 0 & c_{23} & s_{23} \\ 0 & -s_{23} & c_{23} \end{pmatrix} \begin{pmatrix} c_{13} & 0 & s_{13}e^{-i\delta} \\ 0 & 1 & 0 \\ -s_{23}e^{i\delta} & 0 & c_{13} \end{pmatrix} \begin{pmatrix} c_{12} & s_{12} & 0 \\ -s_{12} & c_{12} & 0 \\ 0 & 0 & 1 \end{pmatrix}, \tag{1.2}$$

with s_{ij} and c_{ij} being abbreviations for $\sin\theta_{ij}$ and $\cos\theta_{ij}$.

Solving the Schrödinger equation assuming the neutrinos to be plane waves, the mass eigenstates develop like[1]:

$$|\nu_i(t)\rangle = e^{-iE_it}|\nu_i(t=0)\rangle\,, \tag{1.3}$$

with E_i being the energy of the mass eigenstate $|\nu_i\rangle$. For neutrino masses $m_\nu \approx 0$ and its corresponding momentum p_i, the energy of eigenstate i is:

$$E_i = \sqrt{p^2 + {m_i}^2} \overset{m_i \ll p}{\approx} p_i + \frac{{m_i}^2}{2p_i} \overset{p\approx E}{\approx} E_i + \frac{{m_i}^2}{2E_i} \tag{1.4}$$

Using Eq. 1.3 and 1.1, we can calculate the probability $P_{\nu_\alpha\to\nu_\beta}(t)$ that a neutrino which is produced in the flavor eigenstate $|\nu_\alpha\rangle$ becomes flavor $|\nu_\beta\rangle$ [5]:

$$P_{\nu_\alpha\to\nu_\beta}(t) = |\langle\nu_\beta|\nu_\alpha(t)\rangle|^2 \overset{\langle\nu_i|\nu_j\rangle=\delta_{ij}}{=} \left|\sum_{i=1}^{3} U_{\alpha i}U^*_{\beta i}e^{-iE_it}\right|^2 . \tag{1.5}$$

At ultrarelativistic speed $v \approx c$, we can use $t \approx L$, the distance traveled. With Eq. 1.4, we arrive at:

$$\begin{aligned} P_{\nu_\alpha\to\nu_\beta}(L) = \delta_{\alpha\beta} &- 4\sum_{i>j}\mathrm{Re}(U_{\alpha i}U^*_{\beta i}U^*_{\alpha j}U_{\beta j})\sin^2\left(\frac{\Delta m^2_{ij}L}{4E}\right) \\ &+ 2\sum_{i>j}\mathrm{Im}(U_{\alpha i}U^*_{\beta i}U^*_{\alpha j}U_{\beta j})\sin^2\left(\frac{\Delta m^2_{ij}L}{2E}\right), \end{aligned} \tag{1.6}$$

where $\Delta m^2_{ij} = m^2_i - m^2_j$ are the mass squared differences. Neutrino oscillations can happen if at least one mass $m_i \neq 0$. If oscillations are observed between all flavors [6], at least two mass eigenvalues must be different from zero. However, this is only true for neutrinos traveling in a vacuum. [7].

The oscillation probability is a function of L/E and the squared mass differences. While the squared mass differences determine the phase of the oscillations, the mixing angles regulate their amplitudes. Considering antineutrinos, we replace $U_{\alpha i}^{\to} U^*_{\alpha i}$ in Eq. 1.6. Consequently, the detection probabilities for neutrinos and antineutrinos are not equal in the case of a nonzero CP phase δ.

1.2 Neutrino Mass Ordering

We can express one of the mass squared differences Δm^2_{ij} in terms of the other two in the three neutrino picture, i.e.:

$$|\Delta m^2_{32}| = |\Delta m^2_{31}| \pm |\Delta m^2_{21}| \tag{1.7}$$

This leaves six free parameters of neutrino oscillations: the three mixing angles θ_{12}, θ_{13} and θ_{23}, the CP-violating phase δ and the squared mass differences Δm^2_{21} and Δm^2_{31}.

Super-Kamiokande [8] and SNO [1] found evidence that $|\nu_2\rangle$ is more massive than $|\nu_1\rangle$ by exploiting the matter effect which BOREXINO confirmed [9]. It follows that $m_2 > m_1$ and $\Delta m^2_{21} > 0$ [10]. The

[1] In the following $\hbar = c = 1$.

Normal Ordering	Inverted Ordering
$m_1 < m_2 < m_3$	$m_3 < m_1 < m_2$
$\lvert\Delta m^2_{31}\rvert = \lvert\Delta m^2_{32}\rvert + \lvert\Delta m^2_{21}\rvert$ $\rightarrow \Delta m^2_{31} > \Delta m^2_{32}$	$\lvert\Delta m^2_{31}\rvert = \lvert\Delta m^2_{32}\rvert - \lvert\Delta m^2_{21}\rvert$ $\rightarrow \Delta m^2_{31} < \Delta m^2_{32}$

Table 1.1 Differences between the mass ordering possibilities.

sign of Δm^2_{32}, however, remains undetermined. As Δm^2_{31} is almost two orders of magnitude larger than Δm^2_{21}, it can be approximated that $|\Delta m^2_{31}| \approx |\Delta m^2_{32}|$ in many applications.

The two possible arrangements of the neutrino masses are called the normal ordering (NO) and the inverted ordering (IO), which are shown in Table 1.1.

Fig. 1.1 shows a schematic representation of the two possible orderings. The mass eigenstates are ordered from lowest mass to highest. The colors represent the flavor content according to the measured oscillation parameters [11]. The ν_μ and ν_τ contents depend on the value of the CP-violating phase, which is unknown. The not-vertical borders between the red and yellow bands indicate this. However, the possible values of this phase were restricted by a global analysis. The values to the right of each mass eigenstate bar show the possible values that differ for the two mass ordering cases. The mass differences are not to scale.

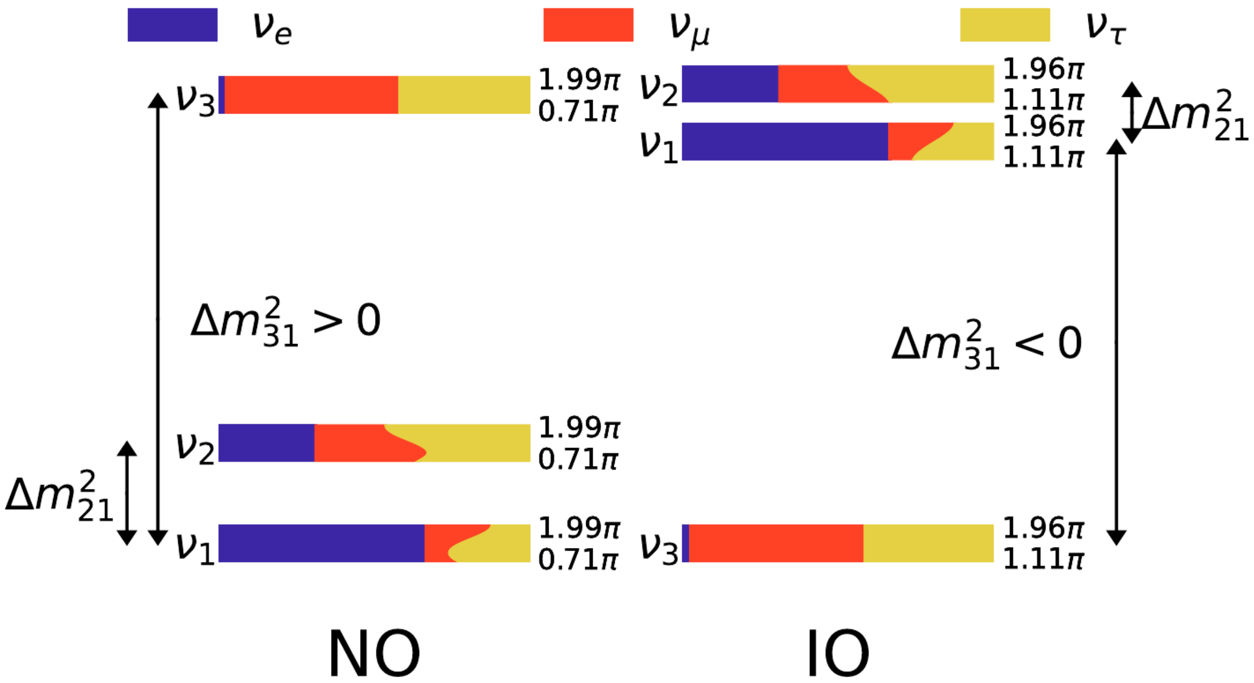

Figure 1.1 Graphical representation of the possible mass orderings. The colors represent the flavor content as a function of the assumed CP-violating phase. The minimal and maximal values of the CP-violating phase are indicated to the right of each mass eigenstate. The differences are not to scale. Source: [12, 11].

Note that the mass squared difference m^2_{32} in Fig. 1.1 differs between the NO and IO. This leads to a difference in the survival probability of, e.g., $\bar{\nu}_e$ [13, 14]:

$$P_{\overline{\nu_e}\rightarrow\overline{\nu_e}} = 1 - \sin^2 2\theta_{13}(\cos^2\theta_{12}\sin^2\Delta_{31} + \sin^2\theta_{12}\sin^2\Delta_{32}) - \cos^4 2\theta_{13}\sin^2 2\theta_{12}\sin^2 2\Delta_{21}\,, \tag{1.8}$$

where $\Delta_{ij} \equiv \Delta m^2_{ij} L/4E$.

Δm^2_{32} appears in the second term of Eq. 1.8. Since Δm^2_{32} determines the frequency of one term, we can interpret the difference between the two neutrino mass ordering (NMO) as a retardance or advancement of the phase of the oscillation as shown in Fig. 2.3. This figure shows the neutrino survival probability as a function of the neutrino 'frequency' L/E for both cases of the NMO: NO (blue) and IO (red). By resolving the positions of the minima and maxima, the NMO can be experimentally determined [13].

The knowledge of the NMO is important for many fundamental questions, e.g., Fig. 1.1 shows that the available values for the CP-violating phase in the lepton sector depend on the NMO. Further examples are:

- The knowledge of the NMO enables model building, e.g., in cosmology [15], astrophysics [16], and neutrino mass generation [17].
- The available parameter space of the effective neutrino mass $m_{\beta\beta}$ in neutrinoless double beta decay experiments. A lower limit for this parameter exists for the IO, which can be reached with next-generation experiments. However, in the case of the NO, the value of $m_{\beta\beta}$ can theoretically be arbitrarily low, and its existence can never be excluded.
- The discovery potential of experiments measuring the CP-violating phase δ is greatly hindered as long as the NMO remains unknown.

See [13, 18] for a more thorough analysis.

Another possibility to determine the NMO is - as in the case of solar neutrinos and Δm^2_{21} - using the matter effect of atmospheric [19] or long-baseline neutrino beams [20, 21] passing through Earth. A combined analysis of the results of this approach together with the energy spectroscopy to measure the phase shift described above vastly increases the sensitivity to the NMO [22, 23].

Thus, experiments that can measure the NMO are highly anticipated. The JUNO experiment - for which Fig. 2.3 was created - is such a project and will be discussed next.

Chapter 2

Jiangmen Underground Neutrino Observatory: JUNO

This chapter serves the description of the Jiangmen Underground Neutrino Observatory (JUNO) experiment. I review the detector design in Sec. 2.1. Sec. 2.2 is dedicated to the detection channels of neutrinos, while Sec. 2.3 describes their applications in a selection of JUNO's physics program.

2.1 Detector Design

The JUNO experiment [13, 24] is under construction in Guangdong Province, South China. Aboveground facilities for the experiment were constructed while the detector is being commissioned in an excavated cavern below. Located under Dashi Hill with a $650\,\mathrm{m}$ rock overburden, a reduced muon flux of $4.1 \times 10^{-3}\,\mathrm{s}^{-1}\mathrm{m}^{2}$ will reach the detector. Fig. 2.1 gives an overview of the detector. The central detector (CD) are $20\,\mathrm{kton}$ of LS, filled into a $12\,\mathrm{cm}$-thick acrylic sphere with a $35.4\,\mathrm{m}$ inner diameter. The sphere rests in a stainless steel (SS) truss, which also holds the photo-multiplier tubes (PMTs). The water pool surrounds the whole construct. It is a $35\,\mathrm{kton}$ ultra-pure water pool, equipped to be a water Cherenkov detector (WCD) and acting as an active muon veto. The veto is predicted to detect more than $99.5\,\%$ of muons and will shield the CD from external backgrounds. The calibration house sits on top of the water tank.

The LS is a mixture of the solvent linear alkylbenzene (LAB), $2.5\,\mathrm{g/L}$ of the fluor 2,5-diphenyloxazole (PPO) and $3\,\mathrm{mg/L}$ of the wavelength shifter 1,4-bis(2-methylstyryl) benzene (bis-MSB). It emits scintillation and Cherenkov light when particles deposit energy, which the PMTs collect. There are 17612 20-inch large PMTs (LPMTs) and 25600 3-inch small PMTs. 5000 LPMTs are Hamamatsu Photonics K. K. manufactured dynode PMTs. The rest are micro-channel plate Photomultiplier Tubes built by Northern Night Vision Technology Co. All LPMTs were extensively tested and characterized [25]. The LPMTs have an acrylic protection cover of $10\,\mathrm{mm}$ to prevent chain reaction explosion events should a PMT break due to the high water pressure. Together, the PMTs achieve a CD coverage of $78\,\%$. The WCD is equipped with an additional 2,400 LPMTs for Cherenkov light detection.

The top tracker (TT) will help with the muon track reconstruction by measuring the direction of muons with an angular resolution of $0.2°$ [26] The TT reuses the plastic scintillator plates of the OPERA experiment [27] to cover $60\,\%$ of the WCD's top area. The expected trigger rate due to the natural radioactivity of the rock cavern is $8\,\mathrm{MHz}$, which is too high to handle for the detector electronics. Therefore, a sophisticated triggering strategy will decrease the trigger rate to approximately $2\,\mathrm{kHz}$. A further reduction to a few Hz will be possible with an offline muon track reconstruction program. The tracks of about $1\,\%$ of the events identified as muons have an angular resolution worse than $0.2°$. The collaboration expects these to be mostly from misidentified cross-talk and noise events. It might be possible to reject these by incorporating WCD and CD data. In [26], the scintillation light degradation due to the aging of the plastic scintillator was quantified, and it agrees with the expectation.

As alluded to in Sec. 1.2, JUNO's main goal is the determination of the NMO using reactor $\bar{\nu}_e$ by measuring the maxima and minima of the oscillation pattern (Fig. 2.2). The interaction channel for the neutrino detection is the inverse beta decay (IBD) $\bar{\nu}_e + p \rightarrow e^+ + n$, explained below. The $\bar{\nu}_e$ flux originates from eight cores of two nuclear power plants (Yangjiang and Taishan), with a combined thermal power of $26.6\,\mathrm{GW}$. They are on average $52.5\,\mathrm{km}$ away from the detector. This is the optimal

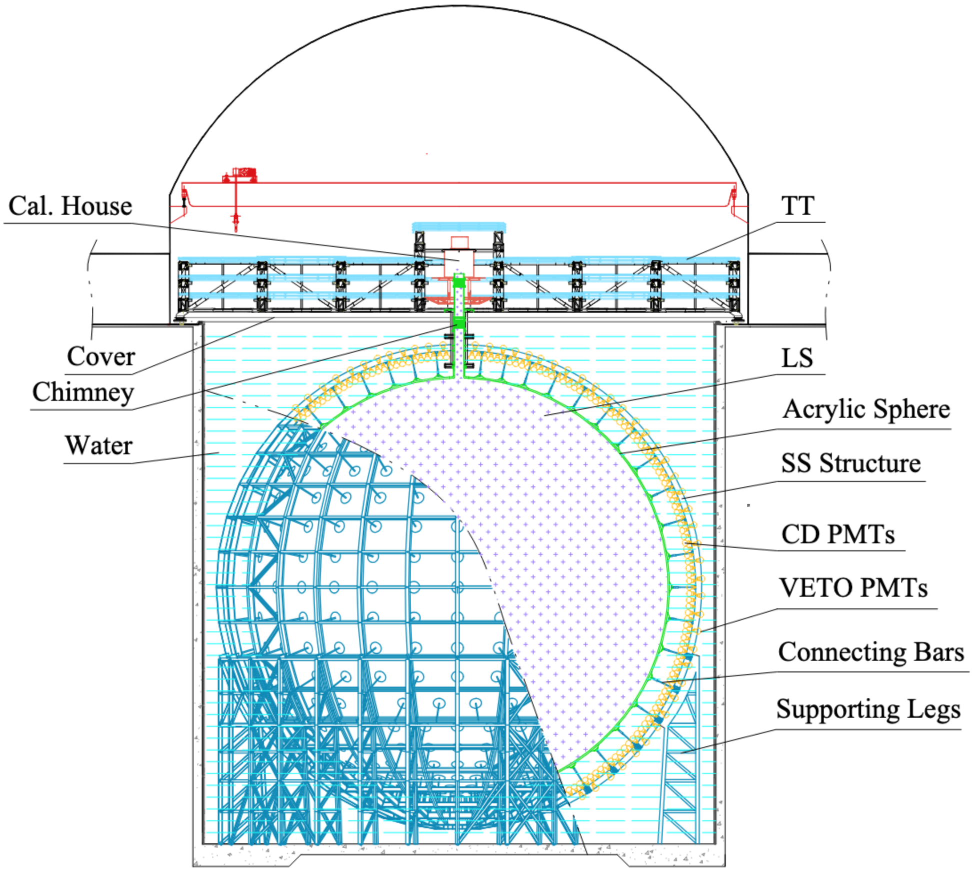

Figure 2.1 An overview of the JUNO detector.

distance for the NMO determination because the differences between the NO and the IO are the most pronounced for reactor neutrinos, which mostly have energies below $10\,\mathrm{MeV}$.

Nuclear reactors are a source of a strong and pure $\bar{\nu}_e$-flux. The fission of plutonium and uranium isotopes and the subsequent decays of their fragments yield $\bar{\nu}_e$ with a continuous energy spectrum. The flux can be controlled by fuel management. The energy spectrum ends at roughly $8\,\mathrm{MeV}$ [28]. Since JUNO measures these neutrinos, it is an electron antineutrino disappearance experiment[1]

The resolution of the exact positions of the maxima and minima of the survival probability of $\bar{\nu}_e$ is very challenging. It requires an energy resolution of the detector of $3\,\%$ at $1\,\mathrm{MeV}$. Taking into account the PMT coverage of the CD, the light yield of the LS must be better than $10\,000\,\mathrm{photons}/\mathrm{MeV}$, which translates to $1345\,\mathrm{p\,e}\,/\mathrm{MeV}$. Moreover, the attenuation length of the LS must exceed $20\,\mathrm{m}$ to guarantee that photons produced in the middle of the CD can reach the PMTs. Additionally, the LS's radiopurity has stringent demands. The LS is the topic of Chapter 3.

To make certain that the LS radiopurity is good enough just before filling the CD, the OSIRIS (Online Scintillator Internal Radioactivity Investigation System) [29] detector will measure the LS. OSIRIS is the main focus of this work and will be discussed in detail in Chapter 4 and the following. Another satellite detector of JUNO is TAO (Taishan Antineutrino Observatory) [30], which is located very close - less than $100\,\mathrm{m}$ - to one of the Taishan nuclear power plant reactor cores. It utilizes a novel detector principle in neutrino physics by cooling its Gadolinium-doped LS to $-50\,°\mathrm{C}$ and registering scintillation light with silicon photomultipliers. It will provide the reactor neutrino energy spectrum with unprecedented precision due to its energy resolution of better than $2\,\%$ at $1\,\mathrm{MeV}$. This spectrum will be an invaluable reference input for the NMO determination of JUNO.

[1] The available energies are to too low to enable $\bar{\nu}_\mu$ or $\bar{\nu}_\tau$ appearance.

The JUNO collaboration plans to finish the CD construction and fill the detector by the end of 2024. OSIRIS has been operational and filled with LS since March 2024. TAO is currently in commissioning.

2.2 Neutrino Detection Channels

To determine the NMO, it is sufficient to detect reactor $\bar{\nu}_e$ only in the IBD channel. Since JUNO is a massive detector, neutrinos from other sources and of other flavors will interact with the target in significant numbers. This opens up the opportunity to use JUNO for many more areas of research than just the NMO determination. In the following, I will list the main neutrino interaction channels relevant in JUNO.

2.2.1 Inverse Beta Decay

Neutrinos can interact via IBD inside the scintillator: [24]

$$\overline{\nu}_{\mathrm{e}} + \mathrm{p} \rightarrow \mathrm{n} + \mathrm{e}^{+}$$

which is the 'golden' channel for detecting MeV electron antineutrinos. The reaction produces a positron and a neutron. The positron loses its energy quickly to the LS and annihilates with an electron into two $511\,\mathrm{keV}$ gammas, providing the prompt signal. The neutron creates the delayed $2.2\,\mathrm{MeV}$ γ-signal when it is captured by a proton after thermalization. The average time the thermalization and capture take is $\sim 200\,\mu\mathrm{s}$. The coincidence between the prompt and the delayed signal are the signature of an electron antineutrino. Selection cuts efficiently reduce the contributing background sources [13]. They include a fiducial volume cut, an energy cut on the prompt and delayed energies, a maximum time and spatial difference between prompt and delayed signal, and a muon veto.

The IBD requires a minimum neutrino energy of $1.8\,\mathrm{MeV}$. Since the majority of the neutrino's energy is transferred to the positron, the neutrino energy can be reconstructed as

$$\begin{aligned} E_{\mathrm{visible}} &= E_\nu - 1.8\,\mathrm{MeV} + 2 \cdot 511\,\mathrm{keV} \\ &= E_\nu - 784\,\mathrm{keV}, \end{aligned}$$

where E_{visible} is the detected visible energy.

The IBD detection channel is used for measuring reactor, supernova (SN), and geoneutrinos as well as the diffuse supernova neutrino background (DSNB).

2.2.2 Charged Current Interactions

The charged current (CC) interactions summarize all reactions between neutrinos and the target which are mediated by a $W^{\pm}$-boson. This obviously includes the above IBD, which is discussed separately due to its eminent importance for JUNO. Examples are: [31]

$$\nu_e +^{12}\mathrm{C} \rightarrow e^- +^{12}\mathrm{N}(1^+;\mathrm{gnd}) \quad (2.1)$$

$$\nu_e +^{13}\mathrm{C} \rightarrow e^- +^{13}\mathrm{N}\left(\frac{1}{2}^-;\mathrm{gnd}\right) \quad (2.2)$$

$$(2.3)$$

These reactions always require a minimum energy of the neutrino, e.g., $16.83\,\mathrm{MeV}$ for the first one. To reliably tag these reactions, they need a coincidence signature otherwise they become a component of the single event spectrum. For example, $\nu_e +^{13}\mathrm{C} \rightarrow e^- +^{13}\mathrm{N}(\frac{1}{2}^-,\mathrm{gnd})$ shows a prompt signal due to the released electron and a delayed signal when the ^{13}N nucleus decays via a delayed β^+-decay ($Q = 2.2$ MeV, $\tau = 863$ s [31].

The applications of CC reactions are solar and SN neutrinos.

2.2.3 Neutral Current Interactions

When the weak interaction proceeds under the exchange of a Z-boson on a nucleus, we refer to it as a neutral current (NC) reaction. Therefore, all neutrino flavors have the same cross-section for processes like: [24, 31]

$$\nu +^{12} \mathrm{C} \rightarrow \nu +^{12} \mathrm{C}^*(1^+; 15.11\,\text{MeV}) \tag{2.4}$$

$$\nu +^{13} \mathrm{C} \rightarrow \nu +^{13} \mathrm{C}^* \left(\frac{3}{2}^-; 3.69\,\text{MeV}\right) \tag{2.5}$$

$$\nu +^{13} \mathrm{C} \rightarrow \nu + n +^{12} \mathrm{C}^*(2^+; 4.44\,\text{MeV}) \tag{2.6}$$

$$\nu + p \rightarrow \nu + p \tag{2.7}$$

While many NC reactions are possible on the isotopes in the LS, the challenge is finding those with a clear signature. If this is impossible the signal has to be identified in the singles spectrum, e.g., the γ-line from $\nu +^{13} \mathrm{C} \rightarrow \nu +^{13} \mathrm{C}^*(\frac{3}{2}^-; 3.69\,\text{MeV})$ for the ^{8}B analysis presented below.

As described below, NC reactions are utilized in solar and SN neutrino searches. The elastic scattering (ES) on protons is especially important in the case of a galactic SN event.

2.2.4 Elastic Scattering

While it is theoretically a NC or CC reaction, ES processes are often considered separately because they have no intrinsic energy threshold: [31, 32]

$$\nu_x + e^- \rightarrow \nu_x + e^-. \tag{2.8}$$

Electron neutrinos can interact via CC and NC, while ν_μ and ν_τ only have the NC interaction available. Therefore, the cross-section is roughly six times larger for ν_e than for the other flavors [32]. In the ES reaction, the LS emits light after the neutrino transfers a fraction of its energy to an electron, which ionizes and excites the LS molecules. The directional information of the neutrino could be recovered by the Cherenkov light which the electron produces in the LS. Unfortunately, the scintillation light vastly dominates the Cherenkov light in JUNO, making this impossible. The visible energy is distributed on a continuous spectrum even for mono-energetic neutrinos due to the scattering kinematics. The visible energy is approximately proportional to the kinetic energy of the electron, especially for larger energy transfers between the neutrino and the electron.

ES interactions play an important role in detecting solar neutrinos as described below.

2.3 Physics Potential

JUNO's primary goal is the determination of the NMO, but it also has a rich physics program pertaining to many other fields of neutrino research. With roughly 60 reactor neutrinos being detected per day, the 1×10^5 neutrinos required for the NMO determination will be detected in six to seven years. Solar neutrino physics will be possible due to thousands of solar neutrinos interacting in JUNO every day. The collaboration expects a few atmospheric neutrinos measured per day. A galactic core-collapse Supernova would cause thousands of neutrinos to register in a few seconds. Four hundred geoneutrinos will be detected annually, and - depending on unknown parameters - a few dozen events from the Diffuse Supernova Neutrino Background. The physics program also comprises searches for proton decay events, sterile neutrinos, and other physics beyond the SM.

2.3.1 Neutrino Mass Ordering

As mentioned above, JUNO's primary goal is the resolution of the NMO question utilizing reactor $\bar{\nu}_e$ by measuring the maxima and minima of the oscillation pattern (Fig. 2.2). The interaction channel is the IBD $\bar{\nu}_e + p \to e^+ + n$, explained above. Two nuclear power plants (Yangjiang and Taishan) provide the $\bar{\nu}_e$ flux with eight cores and a combined thermal power of 26.6 GW. The reactor cores are at the optimal distance for the NMO determination, which is 52.5 km.

The JUNO collaboration reevaluated the sensitivity to the NMO [33]. Compared to the original study [13], multiple assumptions changed: Due to excavation problems, the rock overburden is smaller by 60 m because the detector hall had to be shifted to a higher location, which increases the muon flux. Also, the original planning involved more reactor cores and, therefore, a higher reactor neutrino flux. However, positive developments counter these detrimental effects. The most important change is the introduction of the TAO detector. Its reactor neutrino reference spectrum will improve the spectral shape uncertainty. Additionally, the PMT optical model was improved, and the average photon detection efficiency of many LPMTs is higher than anticipated. With a better detector simulation, the detector resolution expectation sharpened from $3\,\%$ to $2.9\,\%$ at 1 MeV. Finally, revised methods boosted the muon detection efficiency from $83\,\%$ to $91.6\,\%$.

As discussed in Sec. 1.2, the survival probability of reactor $\bar{\nu}_e$ has a slightly different oscillation pattern depending on the NMO. Eq. 1.8 shows that the oscillation pattern exhibits a phase shift between the NMO cases. Fig. 2.2 shows the impact of the neutrino oscillation parameters on the expected energy spectrum (top) and neutrino survival probability (bottom) in the JUNO detector: The dotted line represents the case of no oscillations - scaled to one-seventh of its actual height in the top figure for illustration. The dashed line shows the case without the fast oscillation introduced by $\sin^2\theta_{13}$. The blue and red lines illustrate the impact of this parameter for the NO and IO cases, respectively. If JUNO can resolve the exact positions of the minima and maxima of the wiggles, it can answer the question of the NMO. The bottom figure shows the impact of several neutrino oscillation parameters, exhibiting how JUNO can measure and improve their values.

To reach this goal, the energy resolution must be better than $(3\,\%/\sqrt{E})$. Additionally, large statistics $(O(100\mathrm{k}))$ and excellent knowledge of the detector's absolute energy response (better than 1%) are necessary.

I show JUNO's NMO sensitivity in Fig. 2.3 (from [33]). Red is for NO, and blue is for IO. The dashed/solid lines show the predictions without/with taking the systematic uncertainties into account. We assume that TAO will be online at the same time as JUNO. JUNO will achieve $3\,\sigma$ significance for the NMO after 7.1 years for the NO of data-taking under the assumption of reactor duty cycles of 11/12. JUNO has a slightly increased sensitivity for the IO case. The right side shows the impact on the $3\,\sigma$ threshold of the uncertainty on several oscillation parameters as reported by PDG2020 [34].

The reactor antineutrino measurements will also help JUNO to achieve the most precise measurement of the oscillation parameters θ_{12}, Δm^2_{21}, θ_{13}, and Δm^2_{32} for the foreseeable future [35]. The more precise determination of the oscillation parameters enables testing the unitarity of the PMNS matrix. This is an important test of the SM as a deviation from unitarity would be further proof of unknown physics. Such a discovery would strongly point towards the existence of sterile neutrinos or non-standard interactions [36].

2.3.2 Solar Neutrinos

The Sun produces electron neutrinos during the hydrogen-to-helium fusion. Two reaction chains take part in the fusion: the proton-proton (pp) chain and the CNO cycle. The CNO cycle uses carbon, nitrogen, and oxygen as catalyzers, but its contribution to the total energy production in a star is highly dependent on its mass. Since the Sun is a comparatively light star, only about $1\,\%$ of the energy is

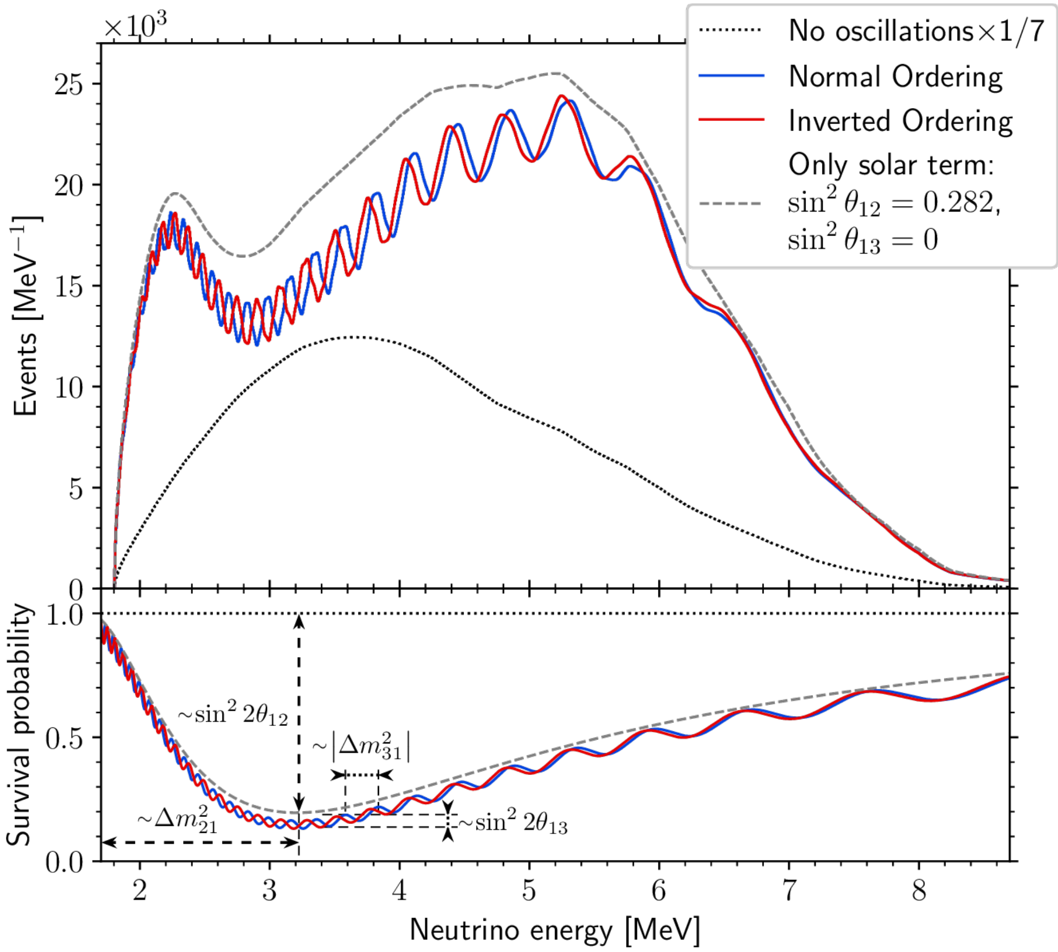

Figure 2.2 The expected reactor $\bar{\nu}_e$ energy spectrum detected (top) and survival probability (bottom) at the JUNO site. The dotted line is for the case of no oscillations - scaled to one-seventh of its height for illustration in the top figure. The dashed line shows the case without the fast oscillation introduced by $\sin^2\theta_{13}$. The blue and red lines illustrate the impact of $\sin^2\theta_{13}$ for the NO and IO case, respectively. Figure taken from [33].

produced in the CNO cycle; the rest comes from the pp chain [37]. The contribution of the CNO cycle has a large uncertainty because of the lack of knowledge of the Sun's metallicity.

The produced neutrinos have different energies depending on the production reaction, as shown in Fig. 2.4. The vast majority of solar neutrinos are pp neutrinos ($\approx 6.0 \times 10^{10}\,\mathrm{cm^{-2}s^{-1}}$), coming from the primary reaction of the pp-chain with a maximum energy of 0.42 MeV. The pp-chain also produces ^{7}Be, pep, ^{8}B, and hep neutrinos. ^{7}Be neutrinos are always mono-energetic, but they can have two distinct energies: 0.862 MeV and 0.384 MeV with a production branching ratio of 0.8949 and 0.1051, respectively[2]. The total flux of ^{7}Be neutrinos is $\approx 5 \times 10^9\,\mathrm{cm^{-2}s^{-1}}$. The last mono-energetic line are pep neutrinos at 1.44 MeV with a flux of $\approx 1.4 \times 10^8\,\mathrm{cm^{-2}s^{-1}}$. The hep neutrinos can have the highest energies (18.8 MeV); however, they remain a theoretical possibility until measured by an experiment due to their tiny flux. The ^{8}B neutrino spectrum ends at slightly lower energies (16.5 MeV) and it has a low flux of $\approx 5 \times 10^6\,\mathrm{cm^{-2}s^{-1}}$. CNO cycle and pep neutrinos have a comparable flux similar with energies reaching 1.74 MeV, when considering ^{13}N, ^{15}O, and ^{17}F decays.

The Standard Solar Model (SSM) describes stars like the Sun when they are in hydrostatic equilibrium. With it, we can calculate observables of the Sun, e.g., the expected neutrino fluxes. However, no conclusive result exists on which available models best describe the Sun (e.g., the discussions in [31, 32]). Precise measurements of the neutrino fluxes, especially those produced in the CNO cycle, would be valuable to decide between high-metallicity (HZ) and low-metallicity (LZ) models [32].

[2]The difference is that the resulting ^{7}Li can be produced in a excited or in the ground state.

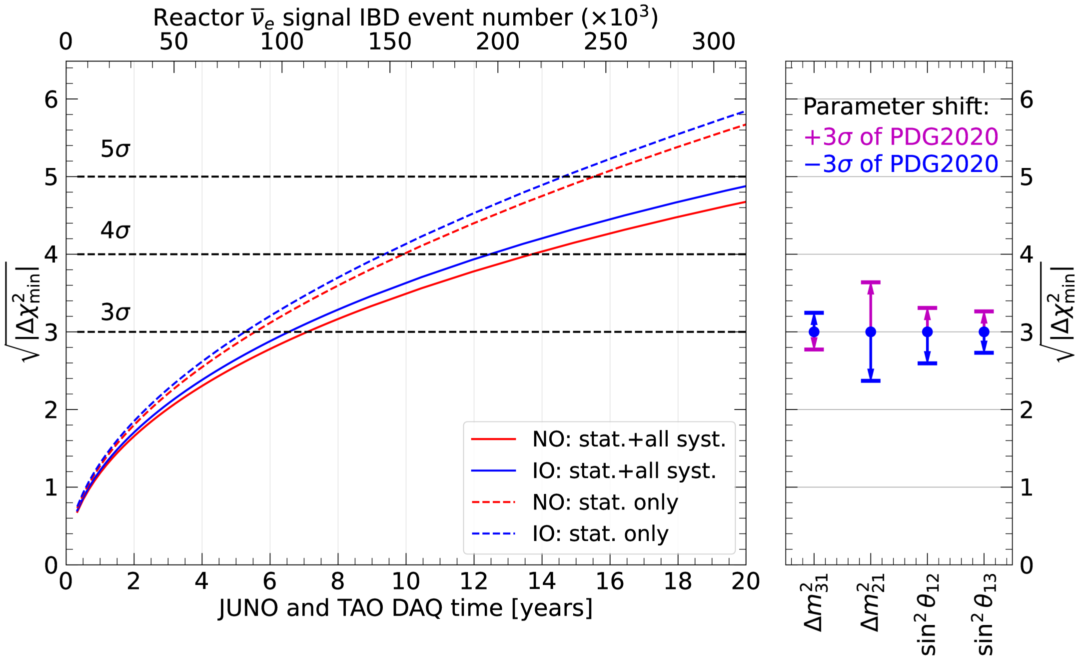

Figure 2.3 The NMO discriminator $\Delta\chi^2_{\text{min}}$ as a function of simultaneous JUNO and TAO data taking time for the NO (red) and IO (blue) ([33]). The horizontal black dashed lines represent $3\,\sigma$, $4\,\sigma$, and $5\,\sigma$ significances. The dashed lines show the predictions with only statistical uncertainties, while the solid lines also include systematic uncertainties. The time (x-axis) takes the presumed 11/12 reactor duty cycle into account. After 7.1 years of data taking, JUNO can resolve the neutrino mass ordering with $3\,\sigma$ significance when NO is true. If IO is true, the sensitivity is slightly better. The right panel shows how the sensitivity changes w.r.t. the true values of the oscillation parameters. We used the values reported in PDG2020 [34] and shifted them by $3\,\sigma$ from the nominal values to calculate their impact. The used exposure is the same as for reaching $3\,\sigma$ for the NO.

In [32], the JUNO collaboration has evaluated JUNO's impact on the advancement of solar physics. The paper concentrates on pep, ^{7}Be, and CNO neutrinos, which will be measured via the ES channel (see above). JUNO's performance will depend on the radiopurity of its LS, see Sec. 3.6. If JUNO can produce a LS better than the minimum requirement by at least one order of magnitude, the experiment will improve the precision of all neutrino flux values. Only for the CNO measurement would JUNO not outperform Borexino if only the minimum radiopurity were reached. Additionally, JUNO can enhance the determination of possible periodic (day/night) modulations and solar seismic waves.

Moreover, ^{8}B neutrinos provide the opportunity to probe the solar neutrinos independently of the solar model. Like SNO [1], JUNO could be able to measure solar neutrinos in all channels described above: CC, NC, and ES.

2.3.3 Proton Decay

Baryon number conservation is an ad hoc introduction to the SM, but not strictly required. However, no experiment has found evidence for its violation [38]. Many theories beyond the SM postulate baryon number violation leading to the decay of the free proton.

As JUNO is a large-scale experiment, it consists of many protons that could decay, assuming that proton decay exists. JUNO focuses on the decay mode $p \rightarrow \bar{\nu}K^+$ to which SuperKamiokande, which has 2.5 times more mass, is not very sensitive [39] because the kaon is below the detection threshold. Unlike SuperKamiokande, JUNO can detect the emitted kaon in its LS. The signature of the decay would be a triple coincidence structure between the kaon energy deposition, the μ^+ from the kaon decay $K^+ \rightarrow \mu^+\nu_\mu$ and the positron from the subsequent muon decay $\mu^+ \rightarrow e^+\bar{\nu}_\mu\nu_e$. The JUNO

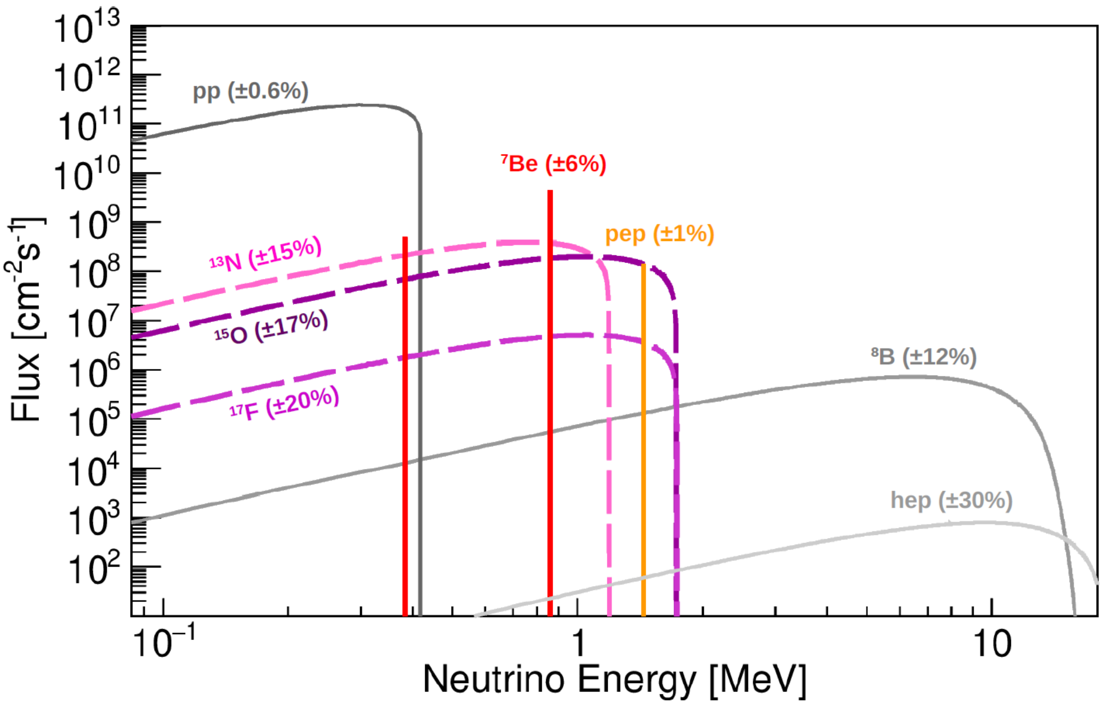

Figure 2.4 HZ-SSM predicted [37] energy spectra of solar neutrinos from the pp chain (solid lines) and CNO cycle (dashed lines). The continuous spectra have 1 MeV bins. The relative theoretical uncertainties of the fluxes are shown in the brackets. Source: [32] and references therein.

collaboration has examined the detector's sensitivity to this proton decay channel [40]. The background to this signal can be suppressed well due to the detector's supreme energy resolution. When allowing for a background of only 0.2 events after 10 years of data taking, the detection efficiency for $p \to \bar{\nu} K^+$ can be $36.9\,\%$. This leads to an exposure of 200 kton years, which translates to being sensitive to proton lifetimes of 9.6×10^{33} years, which is similar to the current best limits.

JUNO's physics program includes many more topics like dark matter searches [41], supernova neutrinos [42], diffuse supernova neutrino background [43], geoneutrinos [44], PMNS-matrix unitarity tests [45], atmospheric neutrinos [46], new physics [47], and more.

All of these measurements only work if the target material, the LS, has the correct properties. In the next chapter, I explain the mechanisms of liquid scintillators, some of the requirements of the JUNO scintillator, laboratory measurements to determine the nonlinearity of its energy response to electrons, and the required radiopurity as well as how the collaboration plans to reach this radiopurity.

Chapter 3

Liquid Scintillators: In General and in JUNO

Like the experiments Double Chooz [48], Borexino [49], and KamLAND [50], JUNO will detect neutrinos using organic liquid scintillators. JUNO's organic liquid scintillator is easy to handle, relatively cheap in production, and has a high light yield.

In this chapter, I first explain the functionality of LSs, focusing on the mechanism of scintillation in Sec. 3.1, wavelength shifters in Sec. 3.2, and the nonlinear energy response in Sec. 3.3. Sec. 3.4 describes the experimental setup and its results used in this thesis to precisely measure the LS nonlinearity. In Sec. 3.5, I lay out the principles of pulse shape discrimination (PSD). JUNO's LS radiopurity requirements in Sec. 3.6 and the employed procedure to achieve them in Sec. 3.7 end the chapter.

3.1 The Electronic Structure and Scintillation Mechanism of Liquid Scintillators

As mentioned above, the LS is a mixture of the solvent LAB, $2.5\,\mathrm{g/L}$ of the fluor PPO and $3\,\mathrm{mg/L}$ of the wavelength shifter bis-MSB. LAB is an organic liquid with $\sim 88\,\%$ of its mass being carbon and $\sim 12\,\%$ hydrogen.

The scintillation light of an organic LS depends on the electronic structure of the molecular bonds. The JUNO LS comprises conjugated aromatic molecules, i.e., benzene rings. Their electronic makeup and the mechanism generating scintillation light are the focus of this section.

3.1.1 The Electronic Structure of Liquid Scintillators

In a benzene ring, the electrons of the carbon atoms change their electronic configuration from $\mathrm{1s^2 2s^2 2p^2}$ [51] when a C atom is isolated to $\mathrm{1s^2 2s^1 2p^3}$ [52]. The bound C atom forms three equal hybrid *σ-orbitals* composed of the 2s and two of the 2p electrons. These orbitals lie in one plane with a $120°$ angle between each. Six carbon atoms bind to each other to create an equilateral hexagon. The corners are the C atoms, and the edges are the *σ-bonds*, which are the bound state of two σ-orbitals of two connected C atoms. Fig. 3.1a shows this schematically.

The third σ-orbital of each C atom binds to a hydrogen atom or another part of the molecule. This leaves one 2p electron unbound for each C atom. They create three fully delocalized *π-orbitals*, which engulf the ring symmetrically as indicated in Fig. 3.1b. The π-orbital is weakly bound and can release scintillation light in the optical spectrum $\lambda > 200\,\mathrm{nm}$ [53]. The σ-bonds require more energy to excite them, resulting in shorter wavelength scintillation light [52].

3.1.2 The Excitation States of π-Bonds and Light Emission

Ionizing particles entering the LS lose energy by exciting and ionizing the molecules. When excited π-electrons deexcite, they may emit a luminescence photon [52]. The wavelength of this photon depends on the energy level to which the π-electron was excited before. To illustrate the energy level, a Jabłoński diagram is useful, as in Fig. 3.2 [54].

The spins of the two electrons forming the π-bond can be antiparallel or parallel. Singlet states have antiparallel and triplet states parallel spins. The solid lines indicate the excited states, S_i or T_i, and the dotted lines represent their vibrational substates, S_{ij} or T_{ij}, where i, j are natural numbers. S_0 is the ground state. Singlet and triplet states have different energy levels, and the transition from triplet to

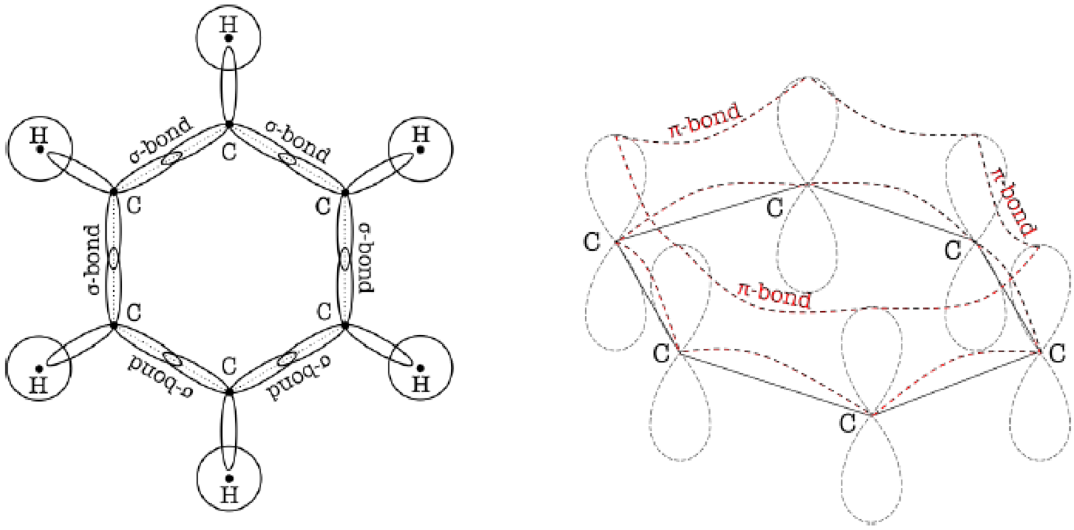

(a) **(b)**

Figure 3.1 Simplified electronic structure of benzene according to [52]. (a) shows the σ-bond structure, and (b) the π-orbitals of a benzene ring.

single states is forbidden because it requires a spin flip. The energy differences between excited states are in the range of 2 eV to 4.5 eV, while the vibrational substates differ by ~ 0.1 eV [52].

All states above S_{10} rapidly decay via radiationless internal conversion to it or one of its vibrational substates S_{1j} with lifetimes $O(1 \times 10^{-11}$ s) [52]. S_{1j} thermalize to S_{10} with lifetimes $O(1 \times 10^{-12}$ s). The *luminescence* of such a scintillator has two components: the fast *fluorescence* and the slow *phosphorescence*. The transition from S_{10} to S_{0j} occurs via photon emission, making up the fluorescence. The lifetime of the S_{10} state is in the range 1×10^{-9} s to 1×10^{-8} s.

Phosphorescence can be as slow as 1×10^{-4} s as it originates from the forbidden transition $\mathrm{T}_{10} \to \mathrm{S}_{0j}$. Generally, states higher than T_{10} decay analogously to the singlet states. Spin-orbit coupling makes *inter-system crossing* from $\mathrm{S}_1 \to \mathrm{T}_1$ possible despite the necessary spin flip. The ground state cannot be excited to a triplet state via photons. However, upon ion recombination after ionization, mainly (ca. $75\,\%$) triplet states are populated [52].

Delayed fluorescence is caused by triplet state deexcitation with reduced lifetimes in the range of 1×10^{-7} s to 1×10^{-6} s. This can happen due to external factors. If the thermal energy is high enough, T_1 can return to S_1, decreasing the lifetime. It is also possible that two T_1 states interact via

$$\mathrm{T}_1 + \mathrm{T}_1 \to \mathrm{S}_0\mathrm{S}_i \to \mathrm{S}_0 + \mathrm{S}_0 + \text{fluorescence}. \tag{3.1}$$

The probability of this process depends on the density of triplet states. The delayed fluorescence is the reason for the slow component of the scintillation light.

3.2 Wavelength Shifters

The absorption and emission spectra of fluorescence-emitting substances of aromatic or conjugated molecules usually have a large overlap. This causes reabsorption of the scintillation photons. In large-scale detectors, this can cause a significant decrease in the detectable light yield. As mentioned above, the JUNO scintillator not only consists of the LS LAB but has $2.5\,\mathrm{g/L}$ of the fluor PPO and $3\,\mathrm{mg/L}$ of the wavelength shifter bis-MSB admixed. Table 3.1 shows the most important information on each LS component.

PPO has a similar absorption spectrum to LAB, but its emission spectrum is shifted towards longer wavelengths due to *internal quenching* [52]. An excited solvent molecule transfers the excitation en-

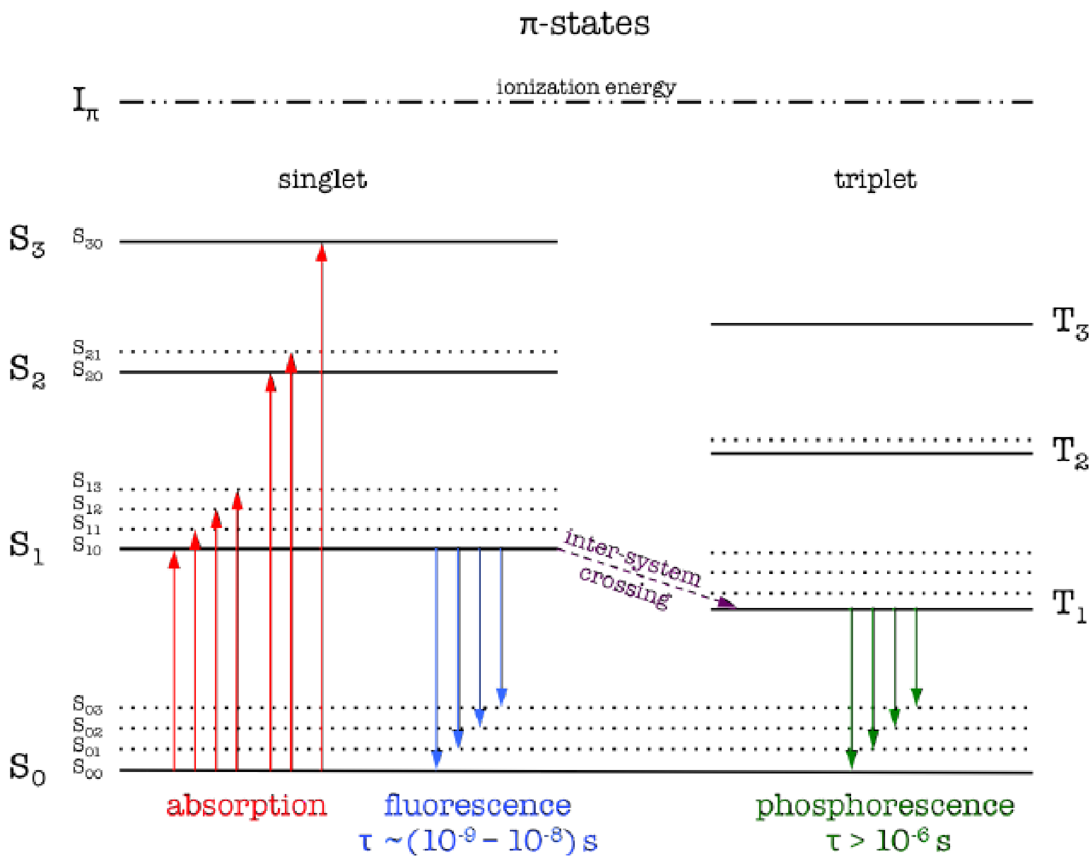

Figure 3.2 Jabłoński diagram illustrating energies of singlet $\mathrm{S_i}$ (left) and triplet $\mathrm{T_i}$ (right) states of π-electrons in an organic liquid scintillator according to [52]. The dashed lines show the vibrational sub-levels. Radiative deexcitation of the singlet state $\mathrm{S_1}$ to vibrational sub-levels of the ground state leads to fluorescence photons. Phosphorescence photons originate similarly but from the triplet state $\mathrm{T_1}$, which has a much longer lifetime. The ionization energy is shown as $\mathrm{I_\pi}$.

ergy via long-range dipole-dipole interaction to the fluor, a non-radiative process [55]. While the fluor can also transmit the energy to the wavelength shifter with this process, the even lower concentration of wavelength shifter molecules makes this a rare process. Therefore, it also happens via radiative transfer, meaning the wavelength shifter absorbs the deexcitation photon emitted by the fluor. Since the fluor has a much lower concentration in the LS than LAB, the probability of selfabsorption of the emitted photon is small.

By adding a fluor (and a wavelength shifter), the LS becomes transparent to the scintillation light. Additionally, PMTs often have detection efficiency spectra that do not coincide with the emission spectrum of the solvent. By adding wavelength shifters, the scintillation light can be adjusted to fit the PMT [56].

3.3 Light Yield Nonlinearity

As Sec. 3.1.2 mentions, the deexcitation processes leading to the S_1 or T_1 state occur non-radiatively. This means that this energy is undetectable and cannot be emitted as scintillation light [58]. This alone would not pose a large problem for any experiment since it would be easy to calibrate. *Ionization quenching* describes the nonlinear behavior caused by other effects which can pose a larger challenge.

An excited molecule can encounter another excited molecule, and one or both lose their energy in a nonradiative process, e.g. [56]:

$$\mathrm{S}^* + \mathrm{S}^* \rightarrow \mathrm{S}^+ + \mathrm{S}_0 + e^-$$

Name	LAB Linear alkylbenzene	PPO 2,5-diphenyloxazole	bisMSB 1,4-bis(2-methylstyryl)benzene
Structural formula	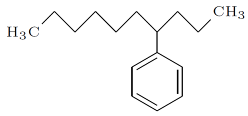	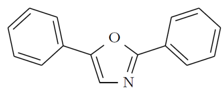	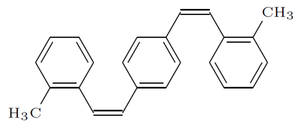
Chemical formula	$C_9H_{12}(CH_2)_n$ $(n = 7 - 10)$	$C_{15}H_{11}NO$	$C_{24}H_{22}$
Density	$0.863\,g/cm^3$	-	-
Emission max. Absorption max.	$283\,nm$ $260\,nm$	$365\,nm$ $303\,nm$	$420\,nm$ $345\,nm$

Table 3.1 The most important properties of the components of the JUNO LS. The emission and absorption spectra maxima wavelengths are given according to [57, 56]. The densities of the fluor (PPO) and wavelength shifter (bisMSB) are negligible due to their small concentrations in the LS.

Additionally, triplet states only lose part of their energy via delayed fluorescence, as shown in Eq. 3.1. Higher ionization densities lead to less light as molecules recombine more often to triplet states. More interactions producing this effect are listed in [52, 59].

A semi-empirical model describing scintillator nonlinearity is Birks' law: [52]:

$$\frac{dL}{dx} = \frac{S \cdot \frac{dE}{dx}}{1 + kB \cdot \frac{dE}{dx}}\,, \tag{3.2}$$

where S is the absolute light yield, dE/dx is the differential energy deposition per unit length, and kB is Birks' factor. Each different scintillator has a different value of this constant, which usually also differs for different particle types.

The absolute light yield is [56]

$$L(E_0) = \int_0^{E_0} \frac{dL}{dx} \cdot \frac{dx}{dE} \cdot dE = \int_0^{E_0} \frac{S}{1 + kB \cdot \frac{dE}{dx}} \cdot dE\,. \tag{3.3}$$

If $kB \to 0$, the quenching is insignificant, and the relationship between the deposited energy and the emitted amount of light is linear.

In the following, I obtain the energy deposition per path length dE/dx from the so-called Berger-Seltzer formula, which can describe the energy loss of low energy electrons and positrons in matter: [60, 61]

$$\frac{dE}{dx} = 2\pi r_e^2 mc^2 n_{el} \frac{1}{\beta^2} \left[\ln \frac{2(\gamma+1)}{(I/mc^2)^2} + F^{\pm}(\tau, \tau_{up}) - \delta \right]\,. \tag{3.4}$$

r_e is the classical electron radius $r_e = e^2/(4\pi\epsilon_0 mc^2)$, mc^2 the mass of the electron and, n_{el} denotes the electron density of the material. I is the mean excitation energy in the material, $\gamma = E/mc^2$, $\beta^2 = 1 - (1/\gamma^2)$, and $\tau = \gamma - 1$. The parameter τ_{max} is $\tau/2$ for electrons, $\tau_{up} = \min(\tau_c, \tau_{max})$, and F^- - for electrons - is given by: [60]

$$F^- = -1 - \beta^2 + \ln[(\tau - \tau_{up})\tau_{up}] + \frac{\tau}{\tau - \tau_{up}} + \frac{1}{\gamma^2}\left[\frac{\tau_{up}^2}{2} + (2\tau + 1)\ln\left(1 - \frac{\tau_{up}}{\tau}\right)\right]\,. \tag{3.5}$$

δ is the density effect function, which I assume to be negligible in this work due to the low energy of the investigated electrons.

The equations also imply that disproportionally less light is emitted for less energetic particles when they are not minimal-ionizing. The reason is that they lose more energy per distance traveled, thus causing higher excitation and ionization densities and increasing the amount of energy lost to nonradiative processes.

3.4 Measurements of the Liquid Scintillator Nonlinearity

The LS nonlinearity can profoundly impact the NMO determination capabilities of JUNO. Fig. 3.3 shows the impact of different values of kB on the energy spectrum of reactor $\bar{\nu}_e$ in JUNO. The figure shows the expectation from the simulation discussed in [62] for the NO. The nonlinearity parameter kB causes the minima and maxima positions of the spectrum to shift. The NMO determination relies on these positions, causing a potential misidentification of the NMO if the nonlinearity is unknown.

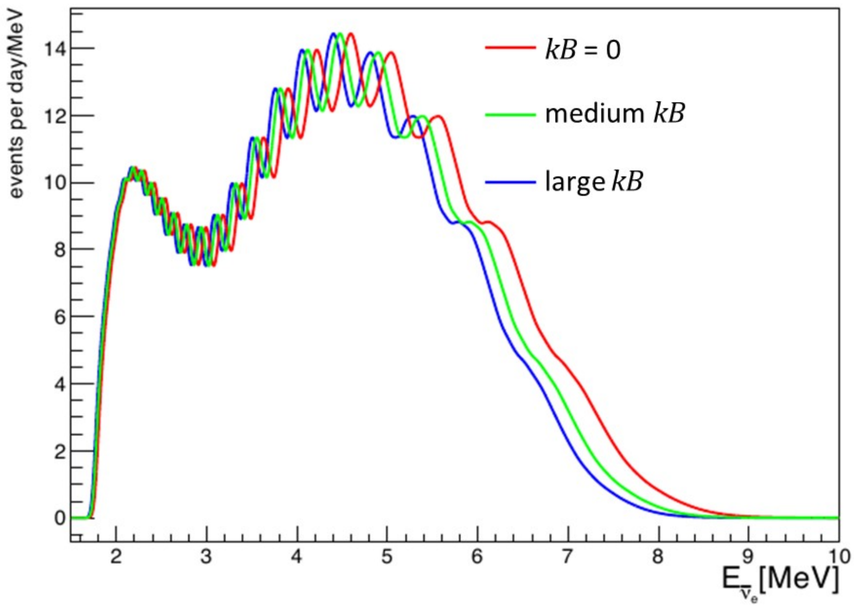

Figure 3.3 Simulation of kB's influence on the JUNO experiment's expected signal for the NO [62]. The expected energy spectrum case in the JUNO detector depends on the scintillator light yield nonlinearity parameter kB. Different values of kB cause a shift of the maxima and minima of the energy spectrum. Since the NMO determination relies on the exact position of these extrema because they differ for NO and IO, the knowledge of the nonlinearity function is critical.

The nonlinearity varies for different scintillation materials and depends on the interacting particle and its energy. Gamma radiation produces scintillation light by transferring part or all of its energy to ionizing particles in the medium, i.e., electrons. Due to the nonlinearity, the light yield of one electron is larger than that of two electrons carrying half the energy. Therefore, the light yield of photons depends on the amount of scattering processes and how the energy transfers are distributed among the electrons. The energy deposition difference between electrons and positrons is negligible [63]. This means that electrons and positrons solely differ by the gammas emitted in the positron annihilation.

While it is possible for large-scale experiments to measure the nonlinearity using fitting radioactive sources [64], it is important to have independent measurements from, e.g., laboratory-scale experiments. Using electron energies below 200 keV, the nonlinearity can be measured in a region where large-scale detectors cannot reach due to their energy thresholds. Additionally, the nonlinear effect becomes stronger at lower energies, allowing for an easier measurement. Moreover, electrons start to produce Cherenkov radiation at roughly 180 keV in JUNO's LS. This increases the light yield and spoils the calculations of the nonlinearity parameter. Staying below this energy threshold avoids having to deal with Cherenkov light. Since large-scale detectors usually have higher energy thresholds than $180\,\mathrm{keV}$, they always have to model the Cherenkov light contribution.

3.4.1 Previous Measurements

The experiment described in [65] was set up to measure the value of kB for the JUNO LS. I continued the work in the context of the thesis at hand. However, the results remain inconclusive. I will concentrate on the measurement principle and the conclusions. For more details on the setup, refer to [65].

To measure Birks' factor kB, the light yield has to be determined as a function of the deposited energy. This can be done for electrons by illuminating a LS sample with a mono-energetic γ-source. By detecting the γ in another detector after the scattering process and measuring its remaining energy, the energy deposited in the LS can be inferred. Fig. 3.5a shows the measurement principle. A PMT attached to a cell containing the LS sample detects the scintillation light. When the scattered γ hits the nearby high-purity germanium (HPGe) detector, the PMT and the HPGe detector register a coincidental signal. The γ-source is ^{137}Cs, which has a mono-energetic peak at $662\,\mathrm{keV}$. The laboratory setup is shown in Fig. 3.5b.

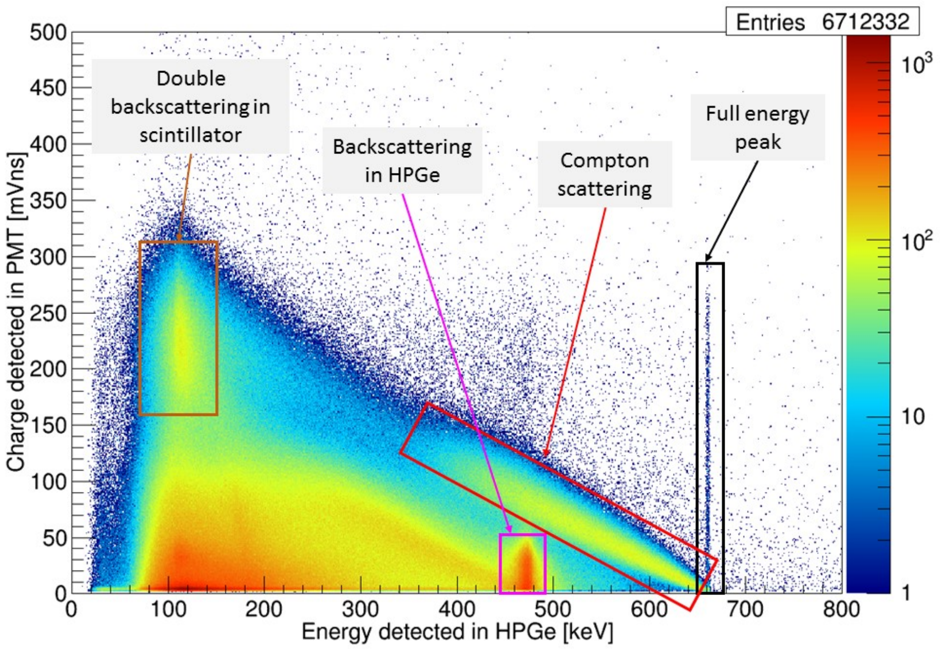

Figure 3.4 The charge-energy spectrum of a coincidence measurement with the source in the middle above the scintillation detector. Each point is one registered event. The z-axis on the right shows the color coding of the number of events in each bin. The energy deposited in the LS is the ^{137}Cs full energy minus the energy detected in the HPGe. The region of interest is inside the red box, where small energy depositions happened in the LS. The events in the black box are accidental coincidences, while the γ was fully absorbed in the HPGe detector. The brown box indicates events where the γ underwent nearly $180°$ scattering in the LS before hitting the HPGe detector. Finally, the pink box contains events where the γ back-scattered first in the HPGe detector and then deposited energy in the LS.

The setup's geometry determines which energies can - primarily - be deposited in the LS. The γ must interact via Compton scattering. The energy transfer depends on the scattering angle in this process [66]. Without taking multiple scattering processes into account, the geometry between γ-source, LS target, and HPGe detector dictate which scattering angles, i.e., energy transfers, lead to a coincident signal in both detectors.

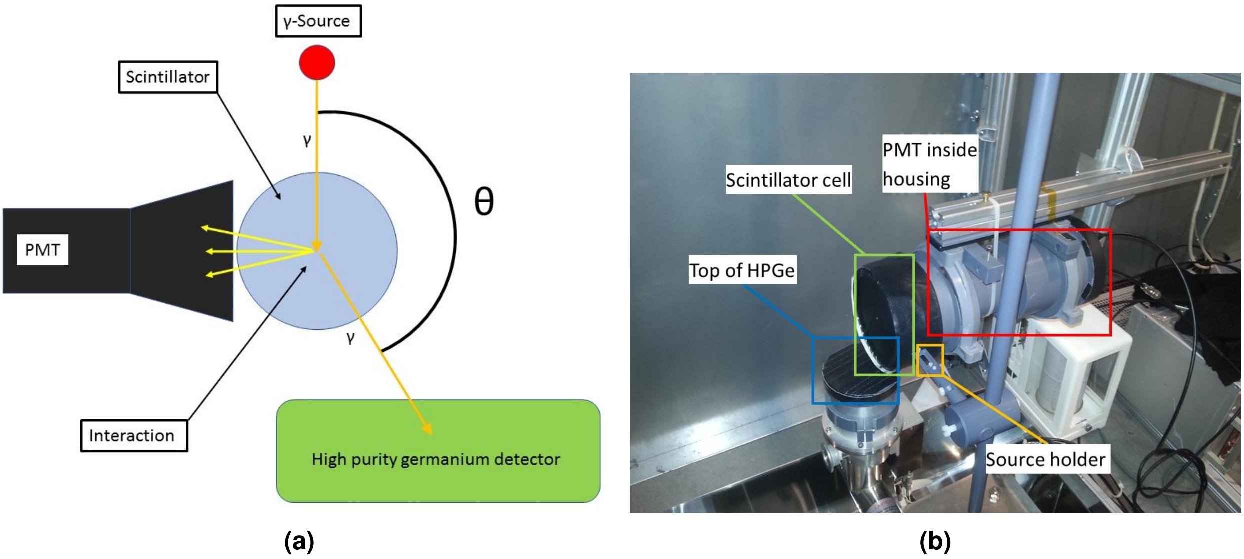

Figure 3.5 The nonlinearity measurement principle (a) and its realization in the laboratory (b).

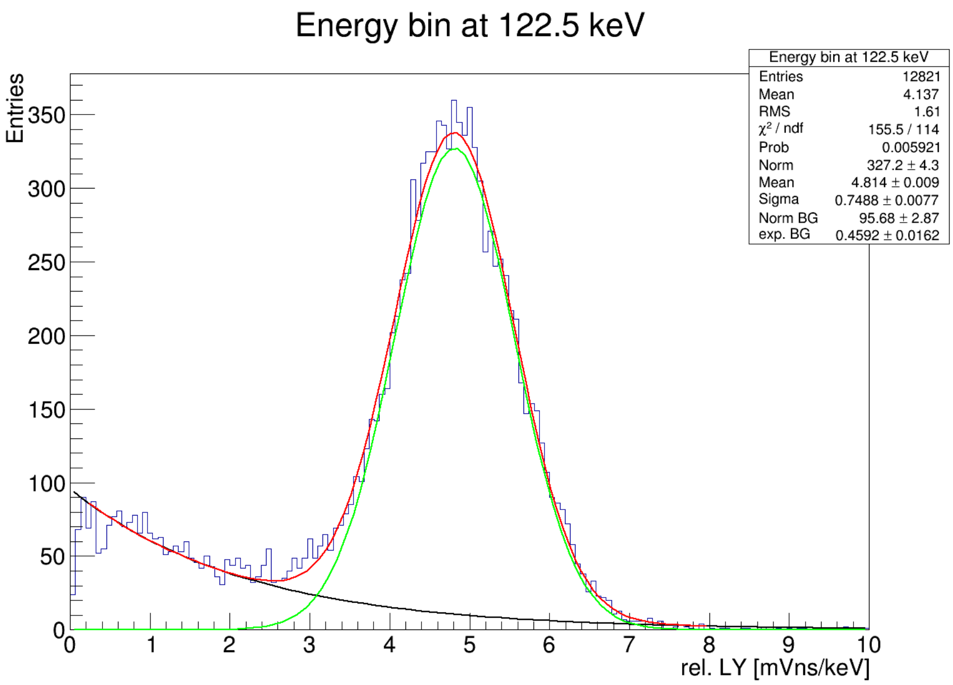

Figure 3.6 The relative light yield (RLY) spectrum for the energy slice of Fig. 3.4 from $120\,\mathrm{keV}$ to $125\,\mathrm{keV}$. The RLY is the charge divided by the mean of the energy slice - $122.5\,\mathrm{keV}$ in this case. The RLY of this energy range is obtained by fitting a Gaussian signal plus an exponential background function to the data. The mean μ is defined as the RLY.

Since the experiment aims to measure the very low energy range, positioning the scintillation detector above the HPGe detector and the source above both allows energy depositions up to ~ 200 keV. Fig. 3.4 displays the resultant energy spectrum of this configuration. The red box contains the events of interest. The projections of energy slices of 5 keV onto the PMT charge axis yield charge spectra. These are converted to RLY spectra by dividing the charge by each event's measured energy. Fig. 3.6 shows the RLY distribution in the 120 keV to 125 keV energy slice. The red line represents the Gaussian signal plus exponential background fit. The mean μ of the Gaussian is taken as the RLY of this energy slice.

Fig. 3.7a shows the resulting RLYs as a function of the deposited energy for all energy slices in the region of interest for multiple measurements. To extract Birks' constant kB, the RLY curve is fitted with Birk's formula (Eq. 3.3). The best-fit values for kB are shown in units cm/MeV.

The light yield quenching is an intrinsic property of the LS. All measurements must arrive at the same value for kB. To test the reproducibility of the setup, the measurements were repeated, and they were done for different positions of the radioactive source w.r.t the detectors. From the front, the scintillator cell is a circle. By moving the source around the edge of the circle - with $0°$ being at the top, the resulting charge-energy spectrum changes due to the different possibilities for the Compton scattering angle. However, the RLY as a function of the energy should stay the same.

Fig. 3.7a shows seven different measurements - some at the same source positions - with vastly differing resulting kB values, from 0.008 cm/MeV to 0.025 cm/MeV. The data follows the expected shape of Birks' nonlinearity formula, but they feature a large systematic uncertainty. This is an unexpected result but reproducible in its irreproducibility.

3.4.2 Investigation of the Systematic Uncertainties

Inspired by another group within JUNO trying to determine the nonlinear behavior, inhomogeneous light collection properties of the light detector (LS cell with the PMT) w.r.t. the light emission location came into the focus of the investigation. If the amount of collected light depends on where the energy deposition happened in the cell, moving the source and, thereby, irradiating other parts of the cell more strongly can change the result.

One reason for the light detector's inhomogeneity can be the PMT's photocathode. It is known that the probability of converting a photon to a photoelectron can be position-dependent on the photocathode [67]. Additionally, the probability of a photoelectron reaching the first dynode normally decreases towards the cathode's edge due to the electric field's shape that accelerates the electrons [67]. Moreover, magnetic fields can drastically affect the probability of photoelectrons reaching the first dynode because the magnetic field can deflect them off the foreseen flight path [67]. While the Earth's magnetic field is constant and the PMT is shielded by a mu-metal shield, surrounding laboratories might work with strong magnetic fields. Due to the relative fragility of the mu-metal shield, its efficacy might have been damaged without visible exterior damage.

To test possible position dependencies, I used the following procedure: A ^{241}Am source emitting very low energy γ's (59.5 keV) is placed directly on the front of the scintillator cell at a few positions. Fig. 3.8 shows the used source positions as the yellow dots. ^{241}Am is suitable because its γ's have low energies that they often deposit fully in the LS. The comparison between the resulting charge spectra at different source positions can reveal the detector's inhomogeneities.

At first, a Cu collimator (3 cm diameter) restricted and focused the γ-flux to a small volume of the scintillation cell. However, the measured charge spectrum was not distinguishable from a background spectrum without the radioactive source. Removing the collimator opens the whole LS cell up to irradiation. However, by placing the source at the edges of the cell and as close to it as possible, most interactions are close to the source location.

The measurements were taken with as little interruption as possible. One measurement was recorded with the source in each location and one without the source to record the background spectrum. Multiple measurement series were done, all yielding very similar results.

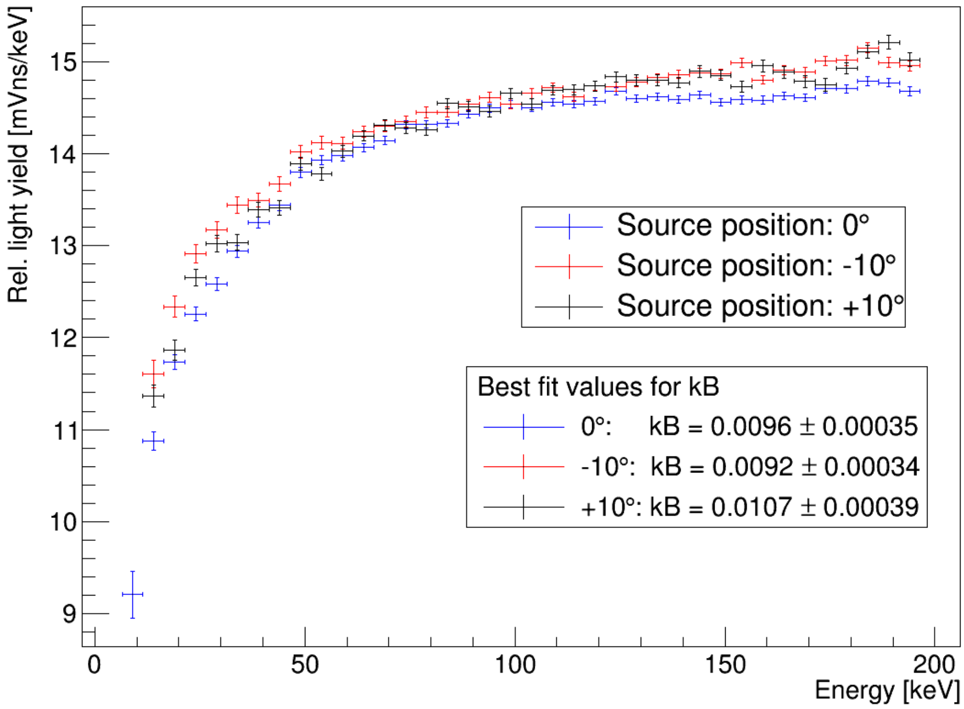

(a)

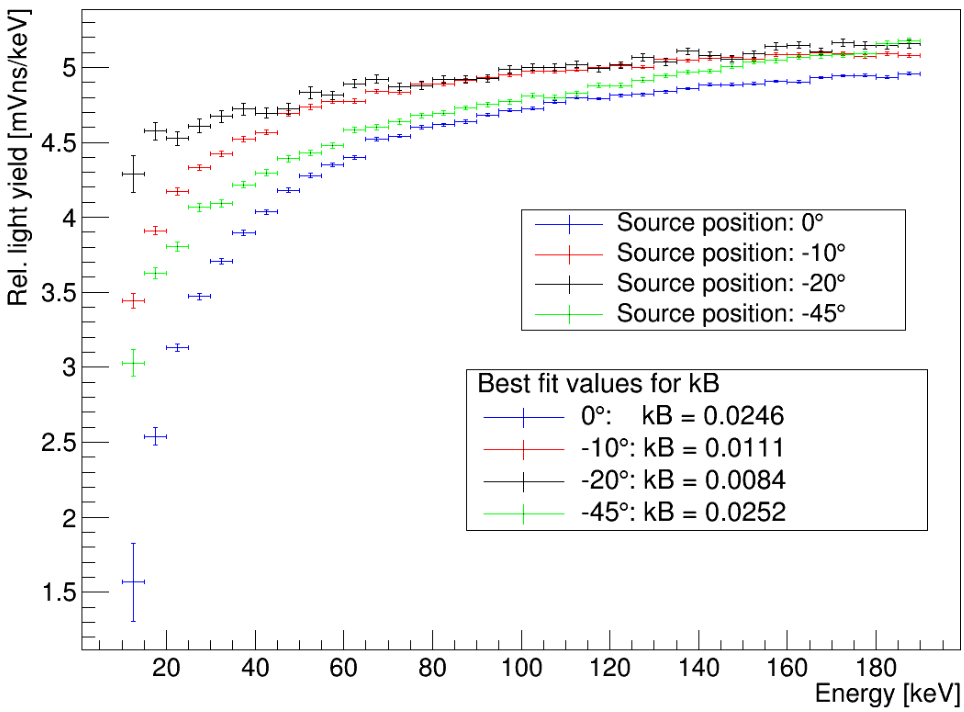

(b)

Figure 3.7 Two sets of LS nonlinearity measurements. The angles indicate where the source was positioned. The angle 0° is at the top when looking at the front of the scintillation detector. Birks' law (Eq. 3.3) fits each data set. The result for the best-fit value of kB should be the same for all measurements. The fact that the values vary greatly points to problems with the measurement setup.

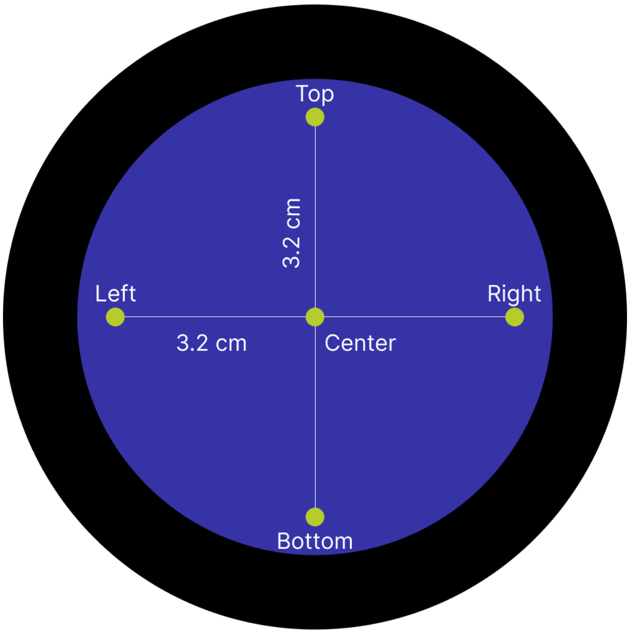

Figure 3.8 A schematic view onto the front of the scintillation detector. The dimensions of the scintillator cell are blue, and the black circle represents the detector's housing. The yellow dots mirror the investigated source positions as in Fig. 3.9 and Fig. 3.10.

Fig. 3.9 shows the resulting charge spectra. The data underwent cuts on the baseline mean and standard deviation. The cuts had similar values, which is reassuring since the baseline shouldn't change between measurements. All spectra are normalized w.r.t. the integral over all bins. For all data sets with the source, I scaled the background spectrum to match the recording time and subtracted it statistically bin-by-bin.

To visualize the variations between these distributions, Fig. 3.10 shows the differences of six pairs. (a) - (d) show the differences between the side and the central spectra. The central position features fewer events until the peak at roughly $0.7\,\mathrm{mV\,ns}$, but more from there to $5\,\mathrm{mV\,ns}$. From this point onward, the spectra don't differ, but the amount of events in this region is very small. (e) illustrates the difference between the top and bottom, while (f) is the left minus the right spectrum.

The large peak is the full-energy peak of the ^{241}Am γ's. Due to the closeness of the source to the scintillator cell, pile-up events are abundant. The bump around $0.8\,\mathrm{mV\,ns}$ in Fig. 3.9 is due to the complete absorption of two γ's, which corresponds to $119\,\mathrm{keV}$. Larger energy depositions are due to multi-γ events. Fig. 3.10 shows that the differences between positions level out around $5\,\mathrm{mV\,ns}$, which corresponds to $\sim 300\,\mathrm{keV}$. The nonlinearity measurements probe energy depositions up to $180\,\mathrm{keV}$. Therefore, the nonlinearity measurement is inside the inhomogenous regime.

Moreover, the difference between two positions swaps its sign as a function of the deposited charge. Around the two-γ absorption ($0.8\,\mathrm{mV\,ns}$), the difference is zero, while it was positive before, and has a negative minimum around $2\,\mathrm{mV\,ns}$. The left-to-right (f) difference varies between 0.042 ± 0.006 at $0.225\,\mathrm{mV\,ns}$ and -0.024 ± 0.004 at $1.775\,\mathrm{mV\,ns}$. At $0.225\,\mathrm{mV\,ns}$, the mean absolute value of the charge distribution between the left and right positions is 0.396, resulting in a relative difference of $(10.6 \pm 1.5)\,\%$. At $1.775\,\mathrm{mV\,ns}$, the mean absolute value of the charge distribution between the left and right positions is 0.163, making the relative difference between these positions $(-14.7 \pm 2.5)\,\%$. The relative differences between the charge distributions are all of the order of $10\,\%$.

Comparing the red and green data points in Fig. 3.7b, we note that the green points are roughly $10\,\%$ smaller than the red ones. Despite this, the kB values derived from the data, 0.0111 and $0.0252\,\mathrm{cm/MeV}$, are more than a factor of two apart. I conclude that the detector inhomogeneity can explain the large variability of the inferred value of kB. While I quantified the position dependencies, I

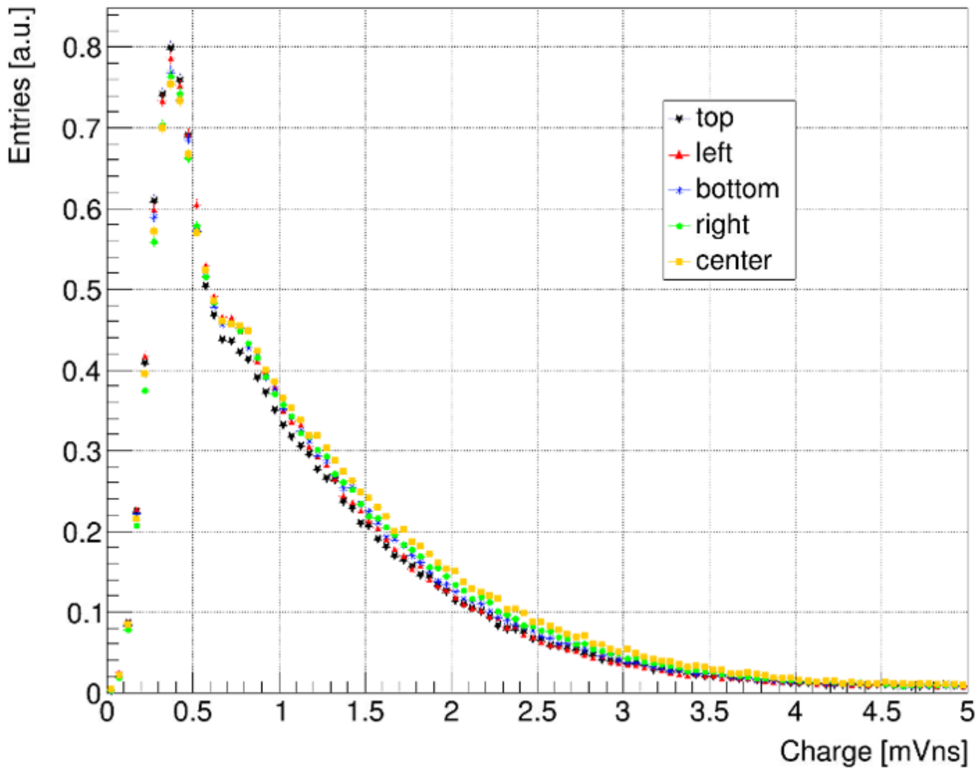

Figure 3.9 The charge spectra of the scintillation detector with the ^{241}Am source at the location indicated in Fig. 3.8.

cannot use these values to correct the kB measurement data because it is unknown where each event happened.

3.4.3 Discussion of the Nonlinearity Measurements

The measurements of the electron light yield nonlinearity of the JUNO LS do not return a reliable result. I can only give a range of values: $0.008\,\mathrm{cm/MeV}$ to $0.025\,\mathrm{cm/MeV}$. The range agrees with measurements of similar scintillators of other experimental groups or publications. Table 3.2 provides a selection of these values. However, this is not good enough for the later interpretation of JUNO data and needs improvement.

Daya Bay used the same LS mixture as JUNO. The comparison to their measured value of the nonlinearity parameter would make the most sense. Unfortunately, the values cannot be compared because their model includes experiment-specific simulation parameters.

The range of values presented in this thesis, $0.008\,\mathrm{cm/MeV}$ to $0.025\,\mathrm{cm/MeV}$, agrees with most of the electron nonlinearity measurements. However, it does not agree with the measurement of the most similar LS of SNO$+$, possibly due to lacking uncertainties.

It is striking that the electron nonlinearities cover a much larger range of values than the proton values, especially if the last value in the proton section is excluded. Comparing the two values of the commercial EJ-301 scintillator shows a large discrepancy, while all three LAB measurements of proton interactions are very similar.

While this work showed that the light detector features inhomogeneities, which might explain the large systematic uncertainties, I cannot provide a quantitative measurement. Additionally, this work couldn't find the source of the inhomogeneity, be it the PMT or, e.g., reflection issues of the scintillator cell. Such a determination might help to model the experimental setup. However, there is no way to determine the position where an event happened inside the cell. Moreover, while the large angular acceptance with the source close to the light detector enables the determination of kB in one measurement, it has

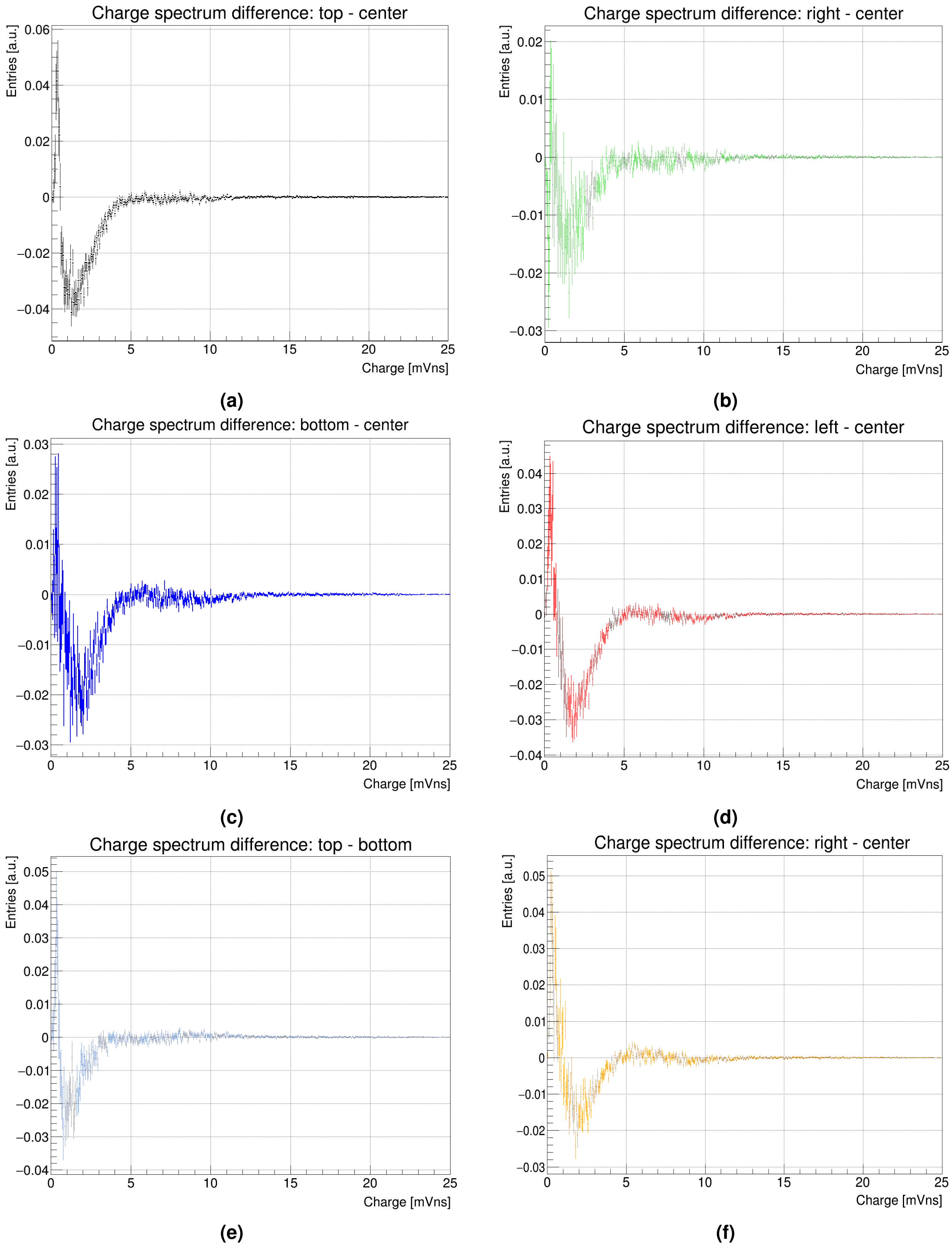

Figure 3.10 The bin-by-bin differences between pairs of the charge spectra at different positions.

a large disadvantage: Multi-Compton scattering while retaining the detector coincidence is very likely. This skews the result, ironically, because of the nonlinearity.

It is possible that the proton nonlinearity measurements (see Table 3.2) have a much smaller variance because their experimental setups - except for [68] - used small angular acceptances by placing the coincidence detector far away. However, this type of measurement almost certainly requires a pulsed beam of the incident particle to ensure that only one particle at a time interacts with the target.

Experiment, Solvent	Reported kB [cm/MeV]	Publication
Electron interactions		
This work	0.008 to 0.025	-
Commercial, EJ-301	0.0217 ± 0.0011	[69]
Commercial, EJ-301	0.0161	[70]
Double Chooz, 5 different LS	$(0.015$ to $0.028) \pm 0.0009$	[71]
SNO+, LAB-PPO (Nd-doped)	0.0074 (0.0091)	[70]
Daya Bay, LAB	$17.6 \pm 3.1^{*}$	[64]
Proton interactions		
JUNO, LAB	$(0.0098$ to $0.0110) \pm 0.0012$	[56]
JUNO, LAB	0.0089 ± 0.0001	[68]
SNO+, LAB (Te-doped)	0.0090 ± 0.0003	[72]
Borexino, PC	$(0.0101$ to $0.0120) \pm 0.0012$	[56]
Double Chooz, DCTarget ([73])	$(0.0122$ to $0.0133) \pm 0.0012$	[56]
PC + TMB	0.0153 ± 0.0002	[74]

Table 3.2 Various measurements of LS nonlinearity parameters kB. The ranges indicate that multiple measurements with differing results or slightly different LS mixtures are listed in the quoted work. Uncertainties are not available for all entries.
*The Daya Bay value cannot be compared: "It is not practical to compare the best-fit values with those of other experiments due to the dependence on simulation parameters." [64]

Despite the efforts of at least four groups within the JUNO collaboration, none have presented a convincing result for the electron nonlinearity. Apart from the measurements at the Technical University of Munich presented here, a group from INFN Milano, another from Charles University in Prague, and a fourth from IHEP Beijing have attempted to determine the electron nonlinearity with high precision. This speaks to the difficulty this measurement method seems to entail. For this reason, the JUNO collaboration has yet to publish a paper on the matter.

Based on the experience with the setup presented in this work, an improved version is under commissioning in Mainz, Germany. The setup features a cylindrical scintillator cell with PMTs attached to both flat sides. The hope is that this reduces detector inhomogeneity by increasing the number of sensitive surfaces. Additionally, the setup features a stepper motor, allowing for more exact and theoretically in-situ movements of the radioactive source.

3.5 Pulse Shape Discrimination

The *pulse shape* is the light emission profile over time after an energy deposition occurs in a scintillator. When an ionizing particle passes through the LS, many molecules transition to an excited state. The deexcitation of each molecule proceeds via the mechanisms laid out in Sec. 3.1.2. The number $N(t)$ of light-emitting transitions $\mathrm{S}_{10} \rightarrow \mathrm{S}_{0j}$ is subject to an exponential decay law

$$N(t) = N_0 \cdot e^{-t/\tau}, \tag{3.6}$$

where N_0 is the number of S_{10} states at time $t = 0$ and τ the lifetime of S_{10} : $\tau \sim 1\text{-}10$ ns. This is the fast component of the pulse shape.

The slow component comprises mainly the deexcitation of the triplet states T_{10}. The transition to the ground or singlet states is forbidden, as described in Sec. 3.1.2. The effects explained there enable these transitions and cause delayed fluorescence. However, due to their more complicated nature, the deexcitation of T_{10} states does not follow a simple exponential law.

A common approach to model the complete pulse shape is the sum of multiple exponential decays, one of which is the fast component:

$$N(t) = \Sigma_{i=0}^{N_{\max}} N_i \cdot e^{-t/\tau_i} \tag{3.7}$$

with N_i and τ_i the number of excited states at $t = 0$ and their lifetime of component i, respectively. Three to four components are usually sufficient to describe the pulse shape [75, 57].

Heavier particles cause higher population fractions of triplet states [56]. This results in enhanced slow components of the pulse shape. These differences between different particle types can be exploited to identify the ionizing particle by the scintillation profile alone. This is called PSD. Fig. 3.11 shows typical pulse shapes of protons, α-, and β-decays schematically. Different techniques to quantify pulse shapes and their application to OSIRIS data are discussed in Sec. 6.3.

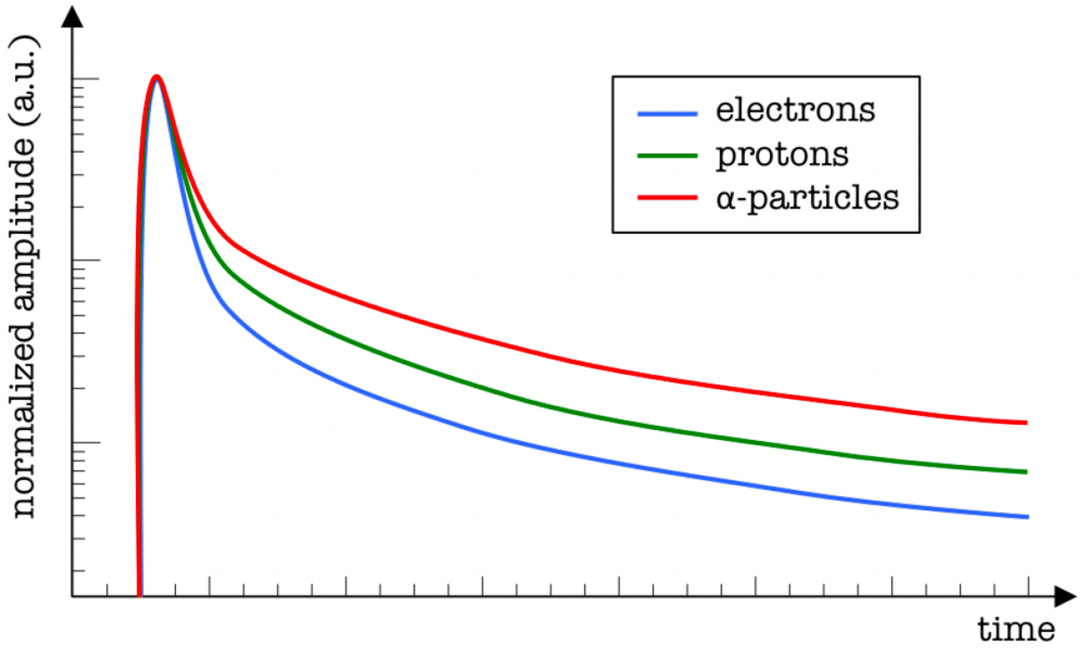

Figure 3.11 Illustration of the qualitative differences of pulse shapes for protons, α-, and β-particles. The y-axis is logarithmic, and the pulses are normalized to the pulse height maximum. Figure taken from [56].

3.6 Radiopurity Requirements

The physical events described in Sec. 2.3 can be overshadowed by signals from internal radioactive contaminations in the LS. To avoid spoiling the detector's sensitivity with too much internal background, the LS must fulfill requirements on its radiopurity.

The JUNO collaboration has identified limits on the radiopurity under which the LS radiopurity should lie for different physics goals [32]. The most important threshold is the *IBD scenario*. Having the LS being this clean or better ensures that the main goal of JUNO, the NMO determination, is not endangered. Table 3.3 shows the necessary values for this scenario. The contamination has the units $\mathrm{g/g}$, which refers to the mass in grams of the respective isotope per gram of the LS. The other limit -

the *solar scenario* - requires two orders of concentration less than in the IBD scenario because many detection channels don't have a coincidence signature that helps suppress backgrounds.

In general, all analyses can suffer from internal radiation signals. For single-event analyses, any signal can be an accidental background if it survives the selection cuts. If the investigated signal has a coincidence structure, background events can be misidentified as a signal event if multiple decays occur with the same structure accidentally or if they have a similar signature themselves. Of course, coincident signals have fewer accidental backgrounds because two or more decays are less likely to happen while also satisfying the coincidence conditions. ^{238}U and ^{232}Th are the mother isotopes of two extremely long-lived decay chains. They appear in almost any material, and the chains include many α-, β-, and γ-decays. If the concentration of these isotopes is too high, the accidental rate can become too large even for coincidence searches. Chapters 6 and 7 contain more information. While ^{210}Pb and ^{222}Rn are isotopes in the ^{238}U chain, they are often out of equilibrium with the chain. They or their daughters are α-decays, which can undergo the α-n-reactions, which are correlated backgrounds and problematic for IBD analyses as discussed below and in Sec. 7.2. Therefore, these isotopes are quoted separately below. ^{40}K is another long-lived abundant isotope. It emits highly energetic γ's (1.46 MeV).

The only problematic radiogenic background for IBD events from the LS that is predicted to survive the data cuts are $^{13}\mathrm{C}(\alpha, n)^{16}\mathrm{O}$ events. However, predictions show they only play a marginal role for the NMO and neutrino oscillation parameter analyses [33, 35]. In this reaction, a α-particle from internal radioactivity creates ^{16}O when it hits a ^{13}C nucleus. The ^{16}O is in an excited state, and its deexcitation mimics the prompt signal of the IBD signature. Additionally, the neutron is thermalized by elastic scattering on protons, which produces more immediate scintillation light. The released neutron then creates the delayed signal after thermalization. The rate of this signal is expected to only be $0.05\,\mathrm{day}^{-1}$ [33].

For solar neutrinos, the detection channels depend on which solar neutrino branch is investigated. In [31], the solar scenario for the radiopurity is identified to be sufficient for the ^{8}B neutrino investigation (see Sec. 2.3). [32] shows the impact of different radiopurity scenarios on ^{7}Be, CNO, and *pep* neutrinos after 6 years of data taking. The uncertainty on ^{7}Be neutrinos will be improved to the percent level even in the IBD scenario. The *pep* neutrino uncertainty depends on the background scenario ranging between $3\,\%$ to $17\,\%$ but is improved w.r.t. the best result in every case. CNO neutrino results will be better than Borexino [76] if the radiopurity is at least one order of magnitude improved w.r.t the IBD scenario.

Target contamination [g/g]	^{238}U	^{232}Th	^{40}K	^{210}Pb/^{222}Rn
IBD scenario	1×10^{-15}	1×10^{-15}	1×10^{-16}	1×10^{-22}
Solar scenario	1×10^{-17}	1×10^{-17}	1×10^{-18}	1×10^{-24}

Table 3.3 The targeted concentrations in the LS of the JUNO detector. The IBD scenario refers to the required radiopurity to successfully determine the NMO, which is the minimal requirement. The solar scenario is for physics with solar neutrinos, which often don't have coincidence signatures to suppress backgrounds and, therefore, need less internal radioactivity [32].

3.7 Liquid Scintillator Handling in JUNO

To guarantee the radiopurity requirements above, the LS undergoes a rigid purifying and screening procedure just before filling it into the CD. Table 3.4 shows the primary contaminants of the LS, their origins, typical contamination in their place of origin, the removal strategy, and JUNO's requirements. Fig. 3.12 shows a schematic layout of the filling and purification systems. The base components, LAB, PPO, and bisMSB, arrive separately onsite. The latter two are filtered and mixed into the master solution if they pass quality control. The LAB is purified in an aluminum column and a distillation tower before it is mixed with the master solution to create the final LS. It then flows into the LS hall just above the CD cavern. There, it is further cleaned with a water extraction and a stripping plant. The purification systems are described in more detail below. As a final check, just before filling into the CD, a fraction of the LS passes through the OSIRIS detector, which will issue a warning if the radiopurity is insufficient. From there, the LS reaches the filling, overflow, and circulation (FOC) system, which pushes the LS into the CD [24].

Radioisotope	Contamination source	Typical value	Removal strategy	JUNO requirement
^{222}Rn	Air and emanation	<$100\,\mathrm{Bq/m^3}$	Stripping	-
^{238}U	Dust in liquid	$\sim 1 \times 10^{-6}\,\mathrm{g/g}$	Distillation and water extraction	<$1 \times 10^{-15}\,\mathrm{g/g}$
^{232}Th	Dust in liquid	$\sim 1 \times 10^{-5}\,\mathrm{g/g}$	Distillation and water extraction	<$1 \times 10^{-15}\,\mathrm{g/g}$
^{40}K	PPO	$\sim 1 \times 10^{-6}\,\mathrm{g/g}$	Distillation and water extraction	<$1 \times 10^{-15}\,\mathrm{g/g}$
^{39}Ar, ^{42}Ar	air	$\sim 1\,\mathrm{Bq/m^3}$	Stripping	-
^{85}Kr	air	$\sim 1\,\mathrm{Bq/m^3}$	Stripping	$1\,\mathrm{\mu Bq/m^3}$

Table 3.4 List of the most important radioisotopes contaminating the LS with their origins and typical concentration. The last two columns present the purification strategies used by JUNO and the JUNO radiopurity requirements. From: [77].

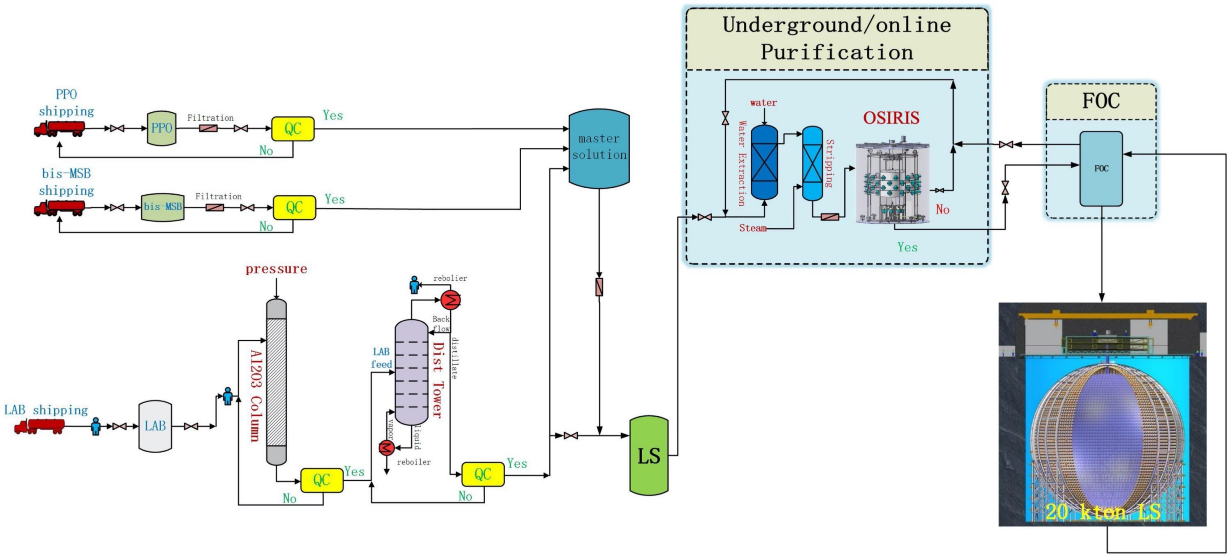

Figure 3.12 Illustration [24] of the LS mixing, purification, and filling. After the base components of the LS arrive on site, they are mixed. Before filling the LS into the CD, it is purified and screened for excessive amounts of contaminants in OSIRIS. See the text for more details.

3.7.1 Aluminum Column

The alumina (Al_2O_3) columns will filter the LAB to enhance the optical properties. Pilot plant experiments helped to find the best design [78]. The system uses aluminum oxide, which is highly adsorptive and binds the LAB impurities. When flowing through, the LAB passes through a fine granulate of aluminum oxide, providing a large surface area with which the LAB comes into contact.

This can significantly enlarge the attenuation length of LAB without introducing other radioactive contaminants above the measurement sensitivity of $\sim 1 \times 10^{-15}\,\mathrm{g/g}$ in [78]. The system comprises three buffer tanks, two alumina filling tanks, and eight filtration columns. Each column is $2.6\,\mathrm{m}$ high with a diameter of $60\,\mathrm{cm}$ [24]. The height-to-diameter ratio will be 3:1 or 4:1 to ensure high purification efficiency. Special care will be taken to carefully handle and pack the alumina to avoid contamination with, e.g., radon.

3.7.2 Distillation

The second stage - distillation - of the purification process further enhances the optical properties of the LAB w.r.t. its absorbance and attenuation length. Additionally, it removes ^{238}U , ^{232}Th , and ^{40}K, some of the most concerning radioactive contaminants. The process exploits mass and heat transfer between the LAB and a gas stream. This is achieved by the equilibrium conditions at each stage of the column. By setting the temperature and pressure, the differing volatilities of the input stream's components cause those with low volatility to end up at the bottom of the system and the high-volatility ones at the top.

The distillation column has a height of $7\,\mathrm{m}$, a width of $2\,\mathrm{m}$ and 6 sieve trays [24, 77]. Preheated ($190\,°\mathrm{C}$) LAB flows into the column against a flow of gaseous LAB, which was produced in a tube-bundle hot oil reboiler. The gas stream is stripped of the contaminants by the above principle and collects at the top. Chilled water cools the gas down in the condenser, making it liquid again. A fraction (<$50\,\%$) of the LAB can be sent back to the beginning before cooling to repeat the procedure and increase the efficiency of the purification. After reaching room temperature in a tank, $1\,\%$ to $2\,\%$ of the LAB move to the next stage - the mixing of the LS - while the rest repeats the loop. The system is constantly kept under a vacuum of $5\,\mathrm{mbar}$. [77] proved that the method decreases contamination with radioactive isotopes and increases the optical transparency of the LAB.

3.7.3 Water Extraction

After mixing, the LS flows underground and into the water extraction plant. Water extraction works on the principle of liquid-liquid extraction. Two immiscible liquids are mixed, and the contaminant moves from the to-be-cleaned liquid to the other because the solvent has a different solubility in the two liquids.

The water extraction system [79] removes ^{238}U and ^{232}Th atoms from the LS, mostly coming from PPO and bis-MSB. The plant comprises a $13\,\mathrm{m}$ turbine extraction tower with a $1\,\mathrm{m}$ diameter and five stages. The turbine mixes the LS and the ultra-pure water provided by the Ultrapure Water (UPW) system. The LS flow rate is $7\,\mathrm{m}^3/\mathrm{h}$ and the water flows at $1.4 - 2.3\,\mathrm{m}^3/\mathrm{h}$. Continuous nitrogen bubbling keeps any residual water in the LS below $200\,\mathrm{ppm}$. The UPW is planned to have ^{238}U and ^{232}Th concentrations < $1 \times 10^{-15}\,\mathrm{g/g}$. Since the water/LS partition coefficient is 10, the LS contamination will be one order of magnitude better, and the system will be upgradeable in the future.

3.7.4 Nitrogen Stripping

The last purification step is nitrogen stripping, which pulls out radioactive gases and gaseous impurities. The LS is preheated before it enters the stripping column. In the column, a current of superheated ultrapure nitrogen, steam, or a mixture of both flows against the LS current. Through desorption, radioactive gases (see Table 3.4) detach from the LS molecules and leave the LS [77].

The stripping column is $9\,\mathrm{m}$ high, and LS enters the plant at $7\,\mathrm{m}^3/\mathrm{h}$ through a set of input fine filters ($50\,\mathrm{nm}$ pore size).[24] It is heated to decrease the LAB viscosity and increase the process efficiency. The counter-current gas stream of the adjustable mixture of ultra-pure nitrogen and UPW steam has a flux of 30-$60\,\mathrm{kg/h}$. The system is in a partial vacuum at $\sim 250\,\mathrm{mbar}$. A $95\,\%$ purification efficiency to remove radon was shown to be possible at pilot plant tests [77]. The final column for JUNO is higher by $50\,\%$ than the one used in [77] leading to the expectation of an even better performance [24].

During the journey of the LS through the purification and mixing pipeline, many small things could go wrong, contaminating the LS without raising alarms. For this reason, the OSIRIS detector will measure a fraction of the LS during the CD filling. The large volume and high sensitivity of OSIRIS allow it to detect ^{238}U and ^{232}Th contaminations down to at least $1 \times 10^{-13}\,\mathrm{g/g}$ within a very short time, immediately identifying severe leaks and alarming the filling to be stopped. Longer measurements will have sensitivities to the $1 \times 10^{-15}\,\mathrm{g/g}$ level. The OSIRIS detector is the next chapter's topic.

Chapter 4

Online Scintillator Internal Radioactivity Investigation System: OSIRIS

JUNO must reach the minimum radiopurity requirements discussed in Sec. 3.6. At the end of the purification chain (see Sec. 3.7), the Online Scintillator Internal Radioactivity Investigation System (OSIRIS) detector will make sure that the LS meets the requirements [29].

OSIRIS contains $18\,\mathrm{ton}$ of the purified LS in a acrylic vessel (AV). 64 PMTs detect the scintillation light, enabling the measurement of radiopurity at least to the IBD level and - depending on the detector performance - to the solar level. For the most sensitive measurements, the LS stays in the detector for weeks or months. During the JUNO CD filling, OSIRIS cannot test the whole LS volume; instead, a fraction is measured, where the LS slowly moves from top to bottom through the AV due to a temperature gradient.

This chapter first outlines the detector design in Sec. 4.1. The detector calibration is discussed in Sec. 4.2, before moving to the software framework of OSIRIS in Sec. 4.3. Lastly, OSIRIS' aspired sensitivity and measurement modes conclude this chapter in Sec. 4.4.

4.1 Detector Design

The detector principle is identical to the JUNO main detector or many other large liquid scintillator detectors [9, 50]. A cylindrical steel tank (height and radius of $9.4\,\mathrm{m}$) acts as a water Cherenkov detector. In the water, a steel frame (SF) holds the PMTs and the AV. The AV contains the LS and is observed by 64 PMTs, which detect the scintillation light. The inner PMTs and the AV form the inner detector (ID). 12 PMTs observe the Cherenkov light in the water, constituting the outer detector (OD). Fig. 4.1 shows a schematic of the detector.

For more detailed information on the detector construction, refer to [29].

Acrylic Vessel (AV)

The AV is a transparent cylinder of $3\,\mathrm{m}$ height and diameter with a wall thickness of $3\,\mathrm{cm}$. It holds $21.2\,\mathrm{m}^3$ of LS. The AV stands on eight acrylic plates mounted on the SF. Since the AV is in direct contact with the LS, it must have as little radioactive contamination as possible. During the AV construction, special precautions were taken to prevent contamination. A special procedure for the creation of acrylic was used. The radiopurity of acrylic samples was confirmed via ICP-MS (inductively coupled plasma-mass spectroscopy). The surfaces were rinsed with deionized water to remove dust.

Steel frame (SF)

The SF has an $8\,\mathrm{m}$ high octagonal shape, holding the AV and PMTs on the inside. The veto PMTs, calibration and sensor systems, and optical separation polyethylene terephthalate (PET) sheets are mounted on the outside. These sheets hang in the SF to prevent light from the outer water tank (WT) from reaching the AV, thereby reducing backgrounds from muons. The SF supports the unfilled AV and compensates buoyancy forces when filled.

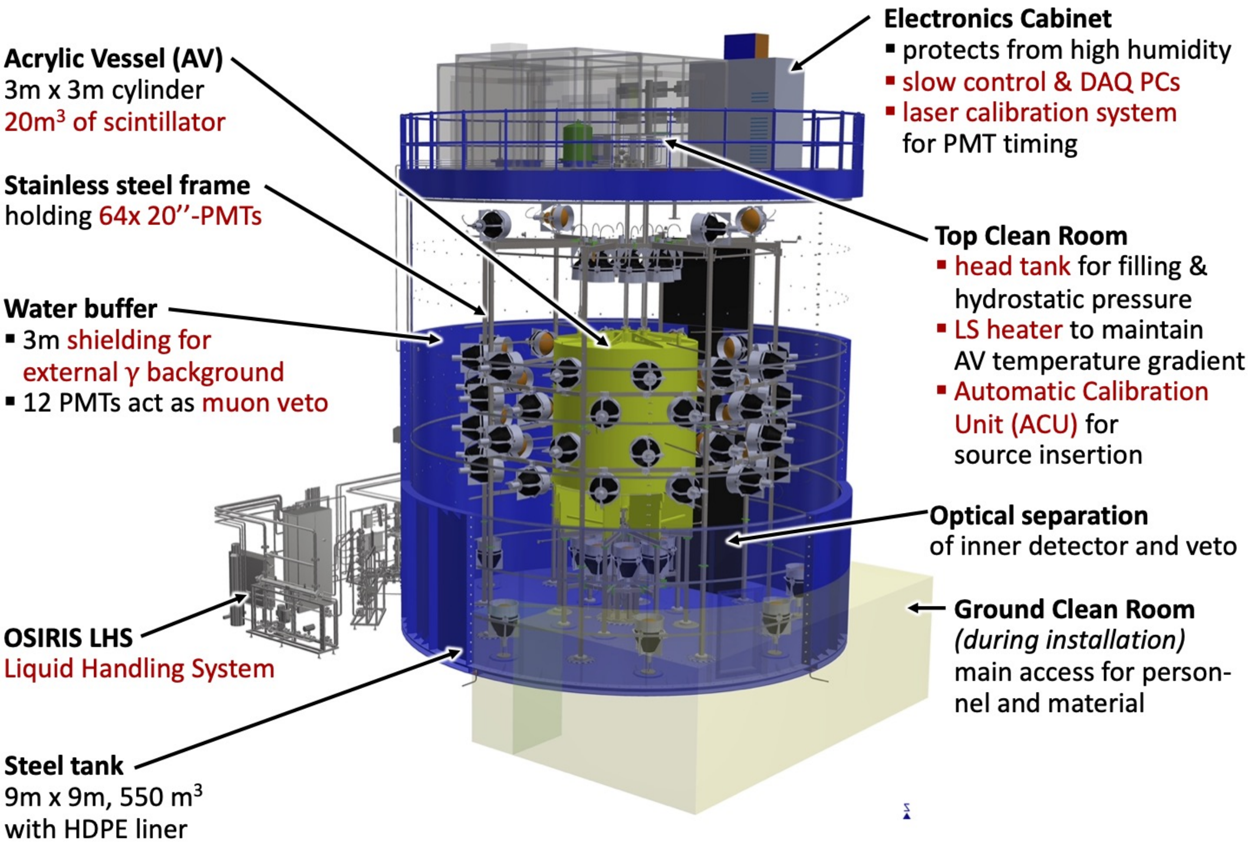

Figure 4.1 Illustration of the OSIRIS detector.

Water tank (WT)

The WT is the $9\,\mathrm{m}$ in height and diameter large steel tank filled with ultrapure water engulfing the AV and SF. It acts as all-around shielding of at least $3\,\mathrm{m}$ against γ-radiation produced in the rock of the Scintillator Hall. The steel tank is bolted together since welding was prohibited in the Scintillator Hall during construction. This makes it much more challenging to make the tank water-tight. A high-density polyethylenes (HDPEs) liner covers every surface, flange, and other details on the inside of the tank to prevent water from leaking and corroding the steel. Despite this, the tank is leaking. The lost water is continuously replenished.

12 PMTs are distributed at the top and bottom of the tank to detect Cherenkov light produced by passing muons. The outside of the PET sheets is white to increase the light yield by reflecting the Cherenkov light. Similarly, the HDPEs liner is covered in white Tyvek foil to increase its reflectivity.

Inner detector PMTs

64 20” Hamamatsu PMTs are arranged as shown in Fig. 4.1. They are attached to the SF, i.d., $1.3\,\mathrm{m}$ from the AV or $2.8\,\mathrm{m}$ from the detector center. The distance decreases the γ-background emitted by the PMT glass. The PMT coverage is $\sim 9\,\%$.

Contrary to the original design [29], OSIRIS does not feature PMTs with a novel design digitalizing the signals at the PMT base. Due to a technical defect, many originally planned PMTs are unusable. Therefore, the OSIRIS detector received spare PMTs and the corresponding data acquisition system (DAQ) from the JUNO main detector [24]. The dedicated underwater boxes had to be fitted to the SF, and the cabling was adjusted accordingly.

Other systems

The liquid handling system (LHS) takes care of filling and exchanging liquids (LS or water) in the AV and WT. It handles the filling with the two operation modes of OSIRIS: batch and continuous mode (see Sec. 4.4). The continuous mode requires a LS heating and a water cooling system. To monitor the liquid filling level and temperature, a multitude of sensors are distributed at strategic locations in the AV and WT.

A clean room sits on top of the WT. It contains the electronics cabinet, housing the DAQ and analysis hardware, and the laser calibration system, which is explained below. Moreover, the clean room also houses the automatic calibration unit (ACU) used before by the Daya Bay collaboration [80].

4.2 Calibration strategies

OSIRIS utilizes two systems for detector calibration: A laser system for PMT timing and charge calibration and a source insertion system for energy and position reconstruction tuning and PMT calibration [29].

The laser system distributes picosecond laser pulses via a fiber network to diffusers inside the detector, from where they are reflected to specific PMTs. The design foresees that the light intensity is in the sub-Poissonian regime. This enables relative timing calibration of the PMTs on a sub-nanosecond level and precise determination of the single photoelectron (p.e.) charges.

The source insertion system makes use of the ACU developed and used by the Daya Bay collaboration [81]. It is located in the calibration house on top of the WT. It has three winches, two holding radioactive sources and the last holding an LED for PMT calibration. One of the radioactive sources is a multi-gamma source comprising the isotopes ^{60}Co, ^{65}Zn, and ^{137}Cs. They feature a combined activity of multiple kBq and cover the energy range from $0.66\,\mathrm{MeV}$ to $2.5\,\mathrm{MeV}$. The LED can provide crosschecks for the laser calibration system and enable the calibration of higher PMT occupancies. The last planned source is a ^{40}K with an activity <$1\,\mathrm{Bq}$. It is supposed to stay in the detector permanently, allowing for constant monitoring of the position of the corresponding peak's energy.

In the context of this work, the calibration systems' usage was limited. Unfortunately, the laser system has not yet been properly tuned. The charge calibration was used; however, the light intensity was too high. This led to a high contamination of multiple p.e. in the charge spectrum. Therefore, only the mean of the single p.e. peak was used. Since the ACU was not operational at the time of writing, the source calibration could not be applied.

4.3 Software Framework for Data Analysis

Since OSIRIS will monitor the radioactive isotope content during the LS filling, the data analysis must proceed in situ, which I will also call *online*. This requires a special DAQ setup, which also influences simulation data. While the detector simulation provides a lot of information on its own, we want to see the impact of the DAQ and online monitoring software on the data processing. Therefore, the simulated data is planned to be handled by the online monitoring software, which puts requirements on its data format.

The general data flow is as follows:

1. The detector DAQ produces data.

2. The EventBuilder (EB) sorts the incoming waveforms by time and converts them to a binary data format.

3. The EB saves the data to the disc and sends it to the RootSorter (RS) online monitoring software.

4. The RS processes the data, provides histograms of the acquired data and saves the processed data to the disc.

Due to the necessary switch of the PMTs, the EB and RS software had to be changed significantly w.r.t. the original design [29]. I oversaw and executed the adjustment and development of the RS in the context of this thesis. Additionally, I wrote documentation for the software and trained new collaborators in its usage.

4.3.1 EventBuilder (EB)

The detector DAQ sends the recorded data to the EB. It acts as the interface between the DAQ and the RS. Before the switch to the JUNO DAQ, the EB was tasked with sorting the incoming waveforms by time and triggering an event if the trigger condition was met. However, the JUNO DAQ triggers on events itself and forwards the current waveform of every PMT. Therefore, every waveform has the same timestamp, and the EB sorting is no longer necessary.

However, the EB is still required to interface between the detector and the RS. The EB packages all waveforms of an event with a header and adds meta-information about the waveforms. It saves the data in a binary file and sends it over ethernet to the RS. Sec. 5.1 describes the data format.

4.3.2 RootSorter (RS)

The OSIRIS RS adapts the RS online/offline analysis toolkit developed at COSY [82]. The RS enables receiving and sending data over TCP/IP, contains classes for data handling, and allows for importing and exporting detector or analysis parameters. Most importantly, it provides a client for online monitoring and analysis. Due to the modularity of the RS, multiple analysis programs can reuse analysis modules, which can also be run in parallel.

In the context of this thesis, I made the RS compatible with the new PMTs. I expanded and integrated several analysis modules, enabling the RS to fully analyze detector data and provide the necessary information, e.g., BiPo rates, to the user. Therefore, OSIRIS can be an alarm system for the LS radiopurity when filling the JUNO CD. The necessary GUI for convenient detector monitoring was also set up. Moreover, the RS writes the processed data to the disc in a comfortable ROOT data structure, drastically reducing disc space usage and facilitating the use of detector data in further offline analyses. Chapter 5 details the RS modules and functionalities.

4.4 Radiopurity Determination Capabilities

The filling of the JUNO CD is planned to commence at a rate of $\sim 6.5\,\mathrm{ton/h}$. This corresponds to roughly one-third of the OSIRIS tank's capacity. Therefore, it is impossible for OSIRIS to screen all of the LS. The traditional method of filling a batch of the LS into the detector and measuring the decays is also untenable because, in the meantime, a large amount of LS would be filled without being screened. Hence, OSIRIS can operate in two modes: *batch mode* and *continuous mode*.

4.4.1 Batch Mode

In this mode, the filled-in LS stays in the detector for days or weeks to reach the detector's design sensitivity threshold of $1 \times 10^{-15}\,\mathrm{g/g}$ and minimal requirement of the JUNO detector (see Sec. 3.6). The new LS is filled at the top and the old LS is drained at the bottom at a rate of $1\,\mathrm{ton/h}$. Fig. 4.2 shows the projected sensitivity of the OSIRIS detector over the measuring time in the presence of externally introduced ^{222}Rn . The detector is designed to reach the IBD contamination level after roughly $10\,\mathrm{days}$ for ^{238}U and for ^{232}Th after only a few days.

4.4.2 Continuous Mode

As mentioned above, the continuous mode is necessary to constantly monitor the LS radiopurity. With a LS exchange rate of $1\,\mathrm{ton/h}$ roughly $15\,\%$ of JUNO's total LS can be screened during filling. Warm LS flows into the AV at the top and, over the course of ca. one day, cools and sinks to the bottom, where it leaves the detector. Cooled water in the WT streams upwards along the AV to stabilize and accelerate the cooling. Since the LS stays only for one day in the detector, this mode is not sensitive to low contamination levels. However, if there is a significant problem somewhere in the LS production and purification pipeline, a large influx of radioisotopes would appear, which would be visible in OSIRIS. Upon an alarm of OSIRIS, the CD filling could be stopped and the problem fixed. This is only possible if the internal radiopurity of the OSIRIS detector is good enough and if not too much external ^{222}Rn is introduced (see Fig. 4.2).

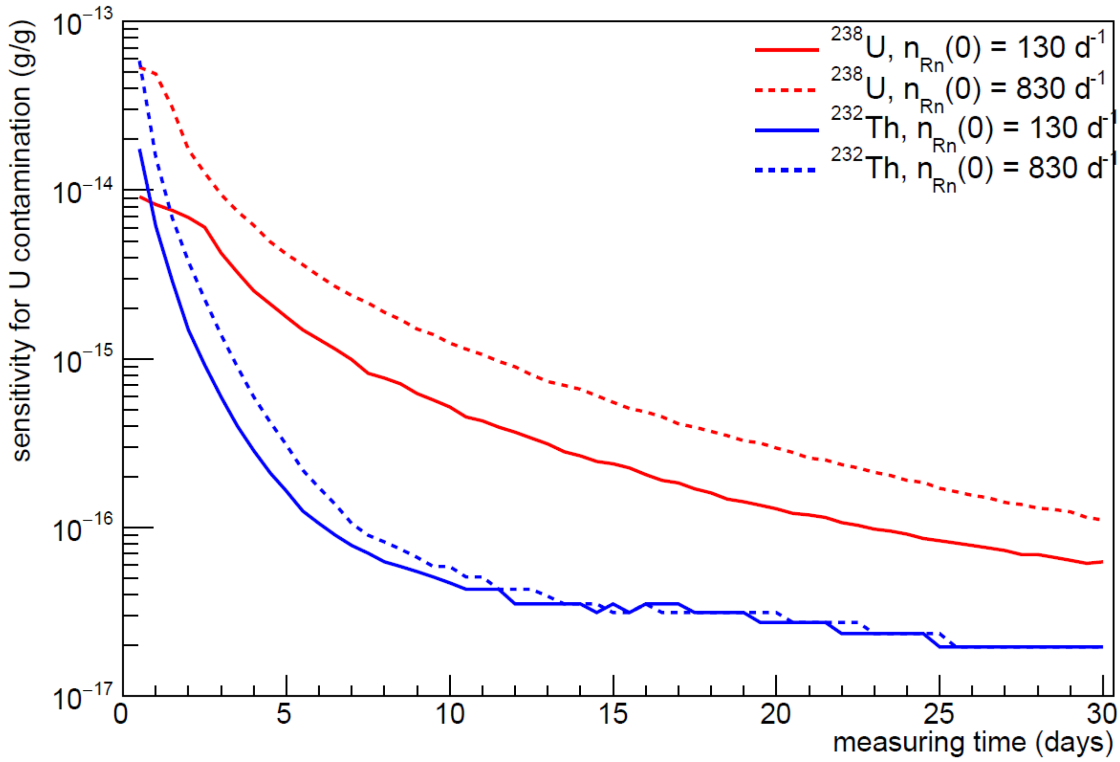

Figure 4.2 The projected sensitivity of the OSIRIS detector to ^{238}U (red) and ^{232}Th (blue) concentrations in the LS as a function of the measuring time. The solid lines assume a ^{222}Rn background of $130\,\mathrm{day}^{-1}$, and the dashed lines a significantly higher rate of $830\,\mathrm{day}^{-1}$. Source: [29].

The online monitoring software RS is of pivotal importance to the goals of OSIRIS. Since its development, maintenance, and supervision were a large part of my work, its features and functionalities are the next chapter's topic. Understanding the RS will help to follow the analyses determining the radiopurity of the LS in chapters 6 and 7.

Chapter 5

The Online Detector Monitoring Software RootSorter

The purpose of the OSIRIS detector is to monitor the radiopurity levels of the liquid scintillator in situ while filling the JUNO CD. This functionality can only be achieved by including an online analysis in the data acquisition and processing chain. The RS, introduced in section 4.3.2, serves this purpose. The RS also provides easily accessible ROOT [83] files. Users can access pre-processed and calibrated detector data, significantly facilitating data analysis.

This chapter will describe in more detail the functionality of the RS. Its development was a significant part of this thesis. Sec. 5.1 describes the read-in of data coming from the EB. In Sec. 5.2, I lay out the waveform reconstruction algorithm developed in this thesis and in Sec. 5.3 I focus on the smoothing filter that the reconstruction algorithm can apply to the data. Sec. 5.4 and Sec. 5.5 describe the event reconstruction and the tools for online PMT and detector monitoring, respectively.

Most analysis-defining variables mentioned below can be chosen before starting the RS analysis. When I mention the values used for the analysis, I will not point out that the value is adjustable.

5.1 Reading Data from the EventBuilder

As described in Sec. 4.3, the EB processes the data from the detector and sends it to the RS. An EB event has the form depicted in Fig. 5.1. Each white cell represents one chunk of data - called a *word* - encoding its information in either 32 or 16 bits. On the left, the format of one EB event is shown. The header (yellow) carries the information on the number of 32-bit words in the event, which is equivalent to the size of the event (in units of 32-bit words). It also specifies the event number, trigger pattern, and the number of subevents.
The subevent header (green) starts with a fixed identifier, the number of words in the subevent. It ends with the event time stamp, given in UNIX time [84] split into seconds and nanoseconds.
Then the *ID data* subevent starts with a fixed identifier and the number of words in it, the **trigger** time stamp, and the number of waveform packets. Afterward, the time-sorted waveform packets are listed (see Fig. 5.1 right). Another subevent header (*External trigger data*) follows in case of an external trigger signal. It has the same format as the ID data except for a different fixed identifier. Normally, it contains only one waveform packet.

The waveform packet's format is shown on the right. Each row represents one 32-bit word comprised of two 16-bit words. The header contains eight words, starting with a fixed value for data validity checking. Since each global control unit (GCU) houses three PMTs, a channel number ranging from zero to two is required. However, data can be collected in low or high gain mode. Therefore, channel numbers zero through two indicate low gain mode, and three through five indicate high gain mode. Channels 0 and 3 belong to the same PMT, 1 and 4 to the second PMT, and 2 and 5 to the third. The next word specifies the number of samples in this waveform. This value is the same for all PMTs and all waveforms in one run. It can be changed, however, in each new run. The RS can process waveform sizes of 600 , 1000, 1008, and 2008 samples.

The cyclic trigger count shows how often each PMT was in an EB event. This is a deprecated field since the waveforms of all PMTs are forwarded by the DAQ once a trigger occurs, making this number always the same as the event number.

The fifth word encodes the firmware version of the GCUs. The remaining three words represent the time stamp of the waveform. The bit values must be concatenated to yield the time in nanoseconds since the start of a global DAQ time, not the UNIX time. This DAQ time has a sampling frequency of $125\,\text{MHz}$, much lower than the analog-to-digital converter (ADC) sampling rate of $1\,\text{GHz}$. Therefore, the real beginning time of a waveform has an uncertainty of $8\,\text{ns}$. The collaboration introduced the *White Rabbit* system to the DAQ chain [85]. With it, the GCUs stay synchronized w.r.t. to the offset between them. Using the laser calibration system, this offset can be taken into account.

The waveform timestamp only has a size of 48 bits. This means that it overflows after roughly $26\,\text{days}$. This means that the time stamp resets to zero, which an analysis spanning data sets of many weeks has to take into account.

Next in the waveform packets are the ADC values of each sample. The current design foresees 600 samples per waveform at a sampling frequency of $1\,\text{GHz}$.

The second-to-last word corresponds to an identifier for the respective GCU (GCU Id)[1]. With the channel number, the GCU Id can be mapped to a PMT identifier (PMT Id) of each waveform.

Importantly, the RS processes one EB event at a time. This means that the read-in starts at the beginning of the current event and stops at the end of its last waveform packet. All analysis modules process this data and fill in the necessary histograms and the output data file. Many modules hold the results of their analysis in temporary storage to make them available to other modules, e.g., many modules need access to the reconstructed waveform data. The RS empties this temporary storage after every EB event to avoid overfilling the computer memory. The RS can, therefore, not access past event data. If data must be available in later events buffer objects with additional storage management are necessary.

The read-in module converts the waveform samples and all other relevant data, e.g., timestamp and PMT Id, from the binary format of the data stream to much easier-to-read decimal or boolean values. These are saved in a special container class, which can be processed by the next analysis modules, especially the waveform reconstruction.

5.2 Waveform Reconstruction

The waveform reconstruction module's task is to use the output of the read-in module, determine the waveform baseline mean and its standard deviation, and identify pulses in the waveform data. Fig. 5.2a shows a raw example waveform and Fig. 5.2b the same waveform after application of the Savitzky-Golay filter (SGF) described in Sec. 5.3. The reconstruction steps below are displayed as additional lines only in Fig. 5.2b because the normal RS analysis always uses the smoothing filter.

The waveform reconstruction starts by calculating the baseline mean μ_baseline and standard deviation σ_baseline of the first 50 samples[2]. They are defined as

$$\mu_\text{baseline} = \frac{\sum_{i=1}^{50} S_i}{50},$$
$$\sigma_\text{baseline} = \sqrt{\frac{\sum_{i=1}^{50}(S_i - \mu_\text{baseline})^2}{50}},$$

where S_i are the values of the waveform samples.

The waveform samples are then multiplied by -1 because the waveforms are negative, and the baseline mean μ_baseline is subtracted from each sample. The range for the baseline determination can be found between the vertical yellow lines in Fig. 5.2b, where the baseline subtraction has already taken

[1] It is actually the backend card to which the GCU is connected.

[2] When the waveform smoothing is enabled, the first few waveforms are not smoothed, and the baseline determination starts with the first smoothed sample. See Sec. 5.3 for more details.

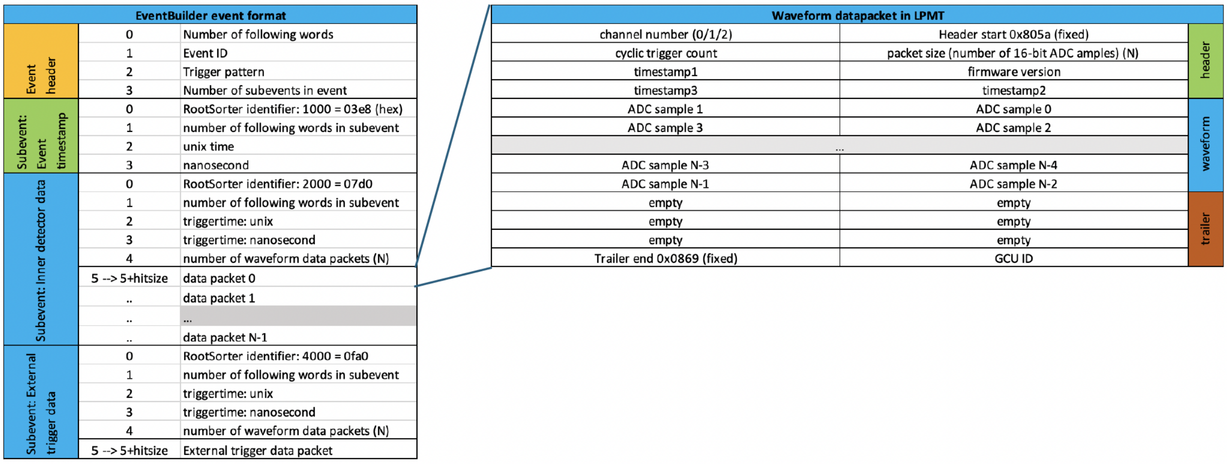

EventBuilder event format		
Event header	0	Number of following words
	1	Event ID
	2	Trigger pattern
	3	Number of subevents in event
Subevent: Event timestamp	0	RootSorter identifier: 1000 = 03e8 (hex)
	1	number of following words in subevent
	2	unix time
	3	nanosecond
Subevent: Inner detector data	0	RootSorter identifier: 2000 = 07d0
	1	number of following words in subevent
	2	triggertime: unix
	3	triggertime: nanosecond
	4	number of waveform data packets (N)
	5 --> 5+hitsize	data packet 0
	..	data packet 1
	..	...
	..	data packet N-1
Subevent: External trigger data	0	RootSorter identifier: 4000 = 0fa0
	1	number of following words in subevent
	2	triggertime: unix
	3	triggertime: nanosecond
	4	number of waveform data packets (N)
	5 --> 5+hitsize	External trigger data packet

Waveform datapacket in LPMT		
channel number (0/1/2)	Header start 0x805a (fixed)	header
cyclic trigger count	packet size (number of 16-bit ADC amples) (N)	
timestamp1	firmware version	
timestamp3	timestamp2	
ADC sample 1	ADC sample 0	waveform
ADC sample 3	ADC sample 2	
...		
ADC sample N-3	ADC sample N-4	
ADC sample N-1	ADC sample N-2	
empty	empty	trailer
empty	empty	
empty	empty	
Trailer end 0x0869 (fixed)	GCU ID	

Figure 5.1 The data format of one event sent from the EB to the RS. An EB event (left) contains N waveform packets (right). The EB event has all waveforms of all PMTs under the *ID data* subevent header. In case of an external trigger signal, the *external trigger data* subevent header is added with the one waveform of the external trigger. Each line represents one 32-bit word containing the information described in the right column.
Each waveform's data is packaged in the waveform packet format (right). Every row contains two 16-bit words. The header and trailer comprise 8 words each, while the number of samples in each waveform can be selected before a run. All of the 16-bit words represent the ADC value of the corresponding sample. To demarcate the beginning and end of a waveform packet, the first word of the header and the last word of the trailer are fixed.

place. Therefore, the waveform baseline is at zero, displayed as the horizontal yellow line. $\sigma_{\mathrm{baseline}}$ is indicated as the red dotted lines above and below the baseline mean line.

The reconstruction algorithm identifies pulses when the signal exceeds $5\ \sigma_{\mathrm{baseline}}$. The pulse is ended when the signal drops below $1\ \sigma_{\mathrm{baseline}}$. If the maximum of the pulse is smaller than $1.5\,$mV or if the time between the start trigger and end trigger is less than $10\,$ns, the pulse is discarded to reduce noise triggers. The pulse height h is the maximum value of the pulse and is represented by the green arrow in Fig. 5.2b. A pulse's start and end times, t_S and t_E, respectively, are defined as the time of the first and last sample larger than $10\% \times h$, respectively, shown as the vertical black lines in Fig. 5.2b.

The charge Q in units of p.e.s of a pulse is the sum of all waveform samples in the range $[t_S, t_E]$ divided by the charge calibration constant of the respective PMT. This charge calibration constant was determined for each PMT individually. For this, the charge spectrum of each PMT was analyzed for a laser calibration data set from March 2024. The charge spectrum exhibits a single p.e. peak whose mean was the calibration constant. The mean was chosen instead of the peak value because it was less distorted by the multiple p.e. contribution. The distortion was unintended, but the illumination of the PMTs by the diffusors was not ideal. The collaboration intends to improve this procedure by taking another data set and including the PMT gain and charge resolution information in calculating the calibration constant.

The algorithm scans the whole waveform for pulses and can find them individually. However, this is not the case if the pulses are so close that they overlap and the signal never falls below the ending threshold. Then, multiple pulses are identified as a singular pulse, as illustrated in Fig.5.3. The black vertical lines indicate the start times of the identified pulses. The first structure clearly contains two separate pulses but is reconstructed as one. In contrast, the second and third pulses are identified correctly. As we will see in Sec. 6.3 and Chapter 7, this deficiency of the waveform reconstruction causes problems with certain types of analyses.

Once the RS has analyzed all waveforms, it removes all waveforms in which no pulse was found. Depending on the PMT Id, the RS categorizes the remaining waveforms as belonging to the ID or OD.

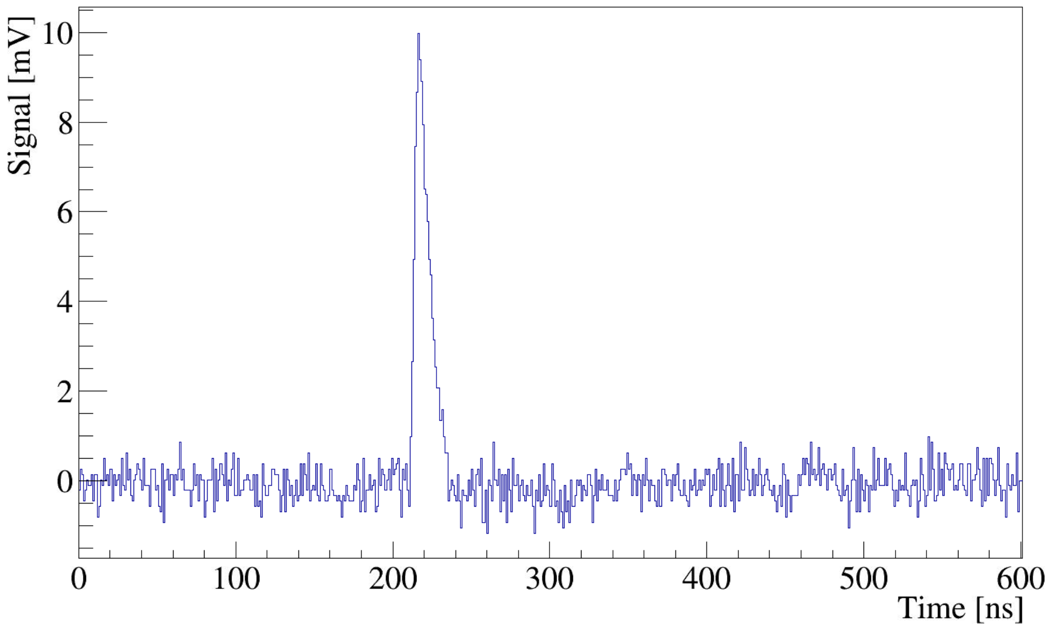

(a)

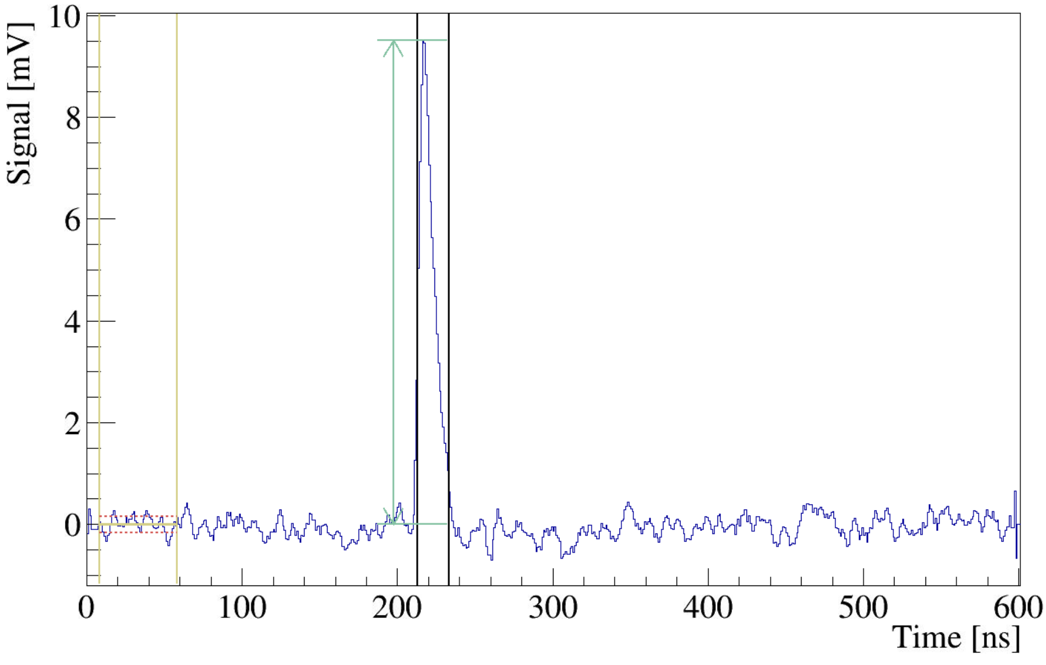

(b)

Figure 5.2 An example waveform, (a) without and (b) with the smoothing filter (see Sec. 5.3) applied. The vertical yellow lines show the range of baseline determination, the horizontal yellow line the reconstructed baseline mean μ_{baseline}, and the dashed red lines delineate the baseline standard deviation $\sigma_{\mathrm{baseline}}$. The green line shows the reconstructed pulse height h. The vertical black lines represent the start and end times of the pulse.

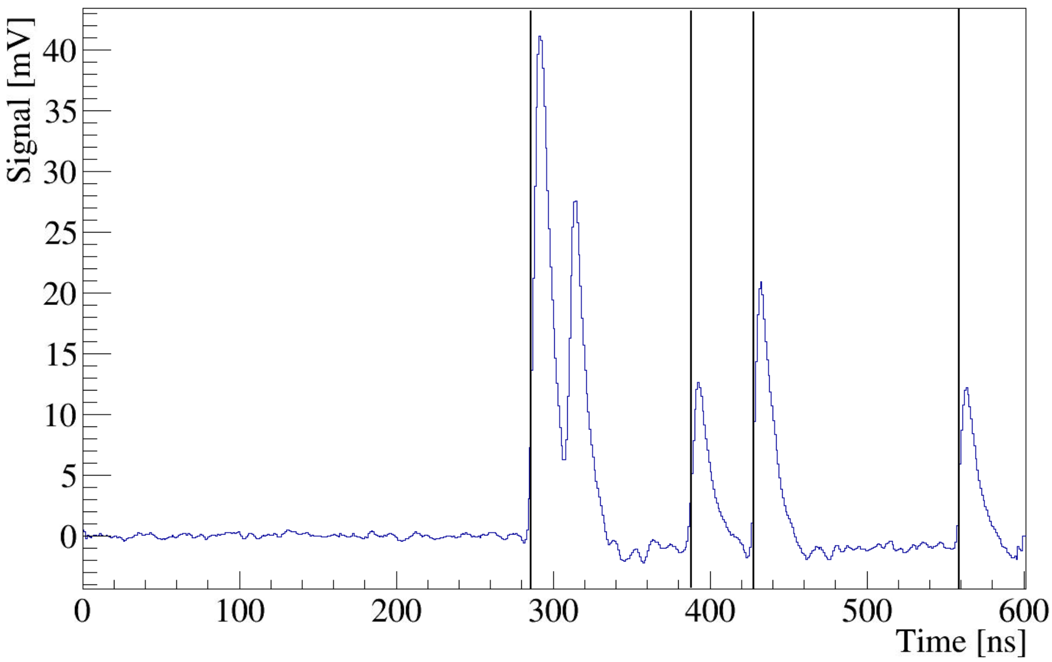

Figure 5.3 An example of a waveform containing multiple pulses. The black lines illustrate the reconstructed start times of pulses. The first structure depicts the deficiency of the waveform reconstruction in identifying pulses when they overlap.

I implemented a smoothing algorithm described below to increase the signal-to-noise ratio of all waveforms. Its implementation and positive effects on the data are discussed below.

5.3 Waveform Smoothing with the Savitzky-Golay Filter

The SGF is a finite impulse response filter commonly used in digital signal processing applications [86, 87]. To suppress noise in the signal, the SGF uses polynomials fitted locally with a least-squares method. The SGF is defined by a window of variable length w and the order of the polynomial p, which is fitted to the signal. These two parameters must be tuned correctly depending on the frequency of the desired signals and unwanted noise. The SGF moves over every data point n and fits the polynomial of order p to the range of data points $[n \pm (w-1)/2]$. This means that w must be odd. Since the first and last $(w-1)/2$ samples do not have $(w-1)/2$ samples to their left and right, the smoothing skips them. Therefore, the baseline determination for smoothed data sets also skips these unsmoothed samples. I adapted the implementation of the SGF developed by M. Tippmann [67].

Fig. 5.2a shows the unsmoothed version of the waveform displayed in Fig. 5.2b. The comparison illustrates the improvement of the baseline variation due to the removal of noise frequencies.

Fig. 5.4 on the left shows zooms into the pulse regions of two waveforms. The unsmoothed waveform is shown as the blue line. The other colors display the SGF smoothed waveforms with different configurations ($p = 5$ for all lines and $w = 11$ (orange), $w = 13$ (green), $w = 15$ (pink), and $w = 17$ (brown)). The figures on the right show the Fourier transforms of these waveforms showing the frequency content of the signal. We observe that the frequency curves diverge - meaning the polynomial fitting removes certain frequencies - around 100 MHz. The brown curve breaks off first because the window for the fit is the longest, making it harder for the fit to follow sharp signal changes. The optimum for the SGF is to follow the blue frequency curve up to the frequencies generated by the real signal and then drop fast toward zero to remove noise signals.

Considering the brown line drops the fastest in Fig. 5.4, it seems like the best choice of these parameter sets. However, this smoothing has a severe effect on the pulses. Fig. 5.5 shows how smoothing affects the normalized pulse height distribution of a data set containing millions of waveforms. The

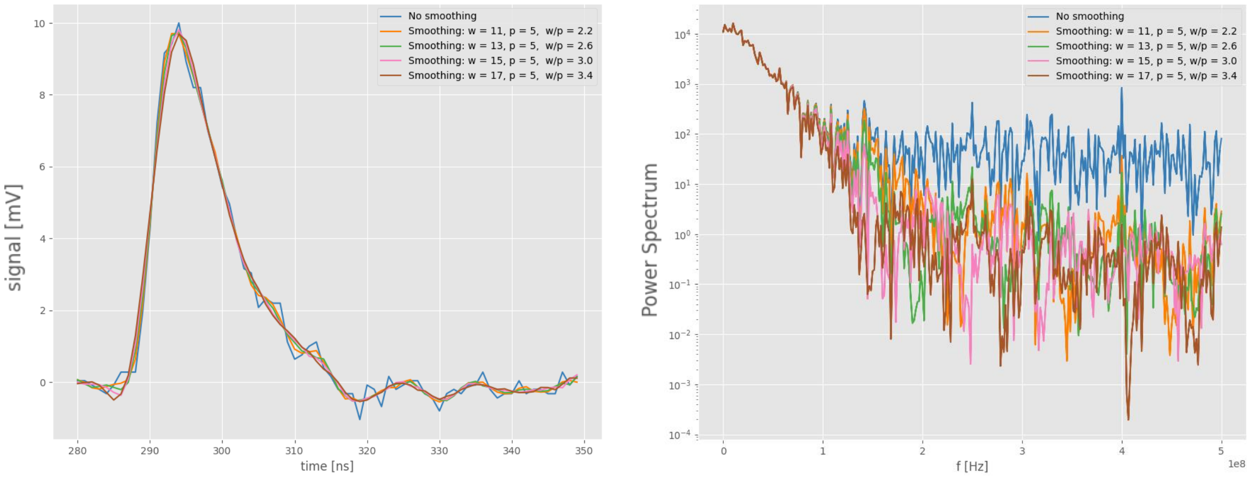

(a)

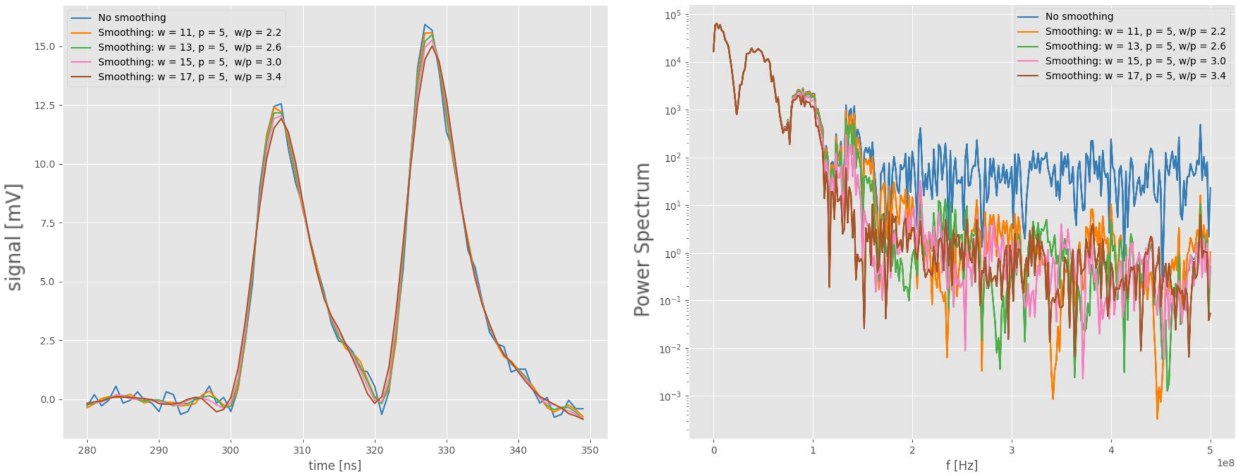

(b)

Figure 5.4 Two examples of waveforms (left) and their Fourier transforms (right). The blue line represents the raw waveform. The other colors show different sets of SGF parameters for the window length w and the polynomial order p.

left figure shows the unsmoothed (red) versus smoothed (black) with the parameters $p = 5$, $w = 17$ - corresponding to the brown lines in Fig. 5.4. By removing frequencies contained in the desired signal, the smoothing alters pulses and, thereby, the pulse height distribution. In contrast, the right figure in Fig. 5.5 shows that sets of smoothing parameters - here $p = 4$, $w = 11$ - that do not affect the pulse heights can be found.

The positive effect of smoothing concerns the reduction of the baseline variation. I measure this via the baseline standard deviation distribution of all waveforms in the investigated data set. Fig. 5.6 shows the unsmoothed standard deviation distribution in blue. I investigated four potential sets of smoothing parameters: $p = 2$, $w = 9$ (orange), $p = 3$, $w = 9$ (green), $p = 4$, $w = 13$ (pink), and $p = 5$, $w = 13$ (brown). The distributions' means shifted to lower values, and their widths decreased. The signal-to-noise ratio f_{SN} of the reconstructed pulses, therefore, increases if we use the simple metric $f_{SN} = h/\sigma_{\text{baseline}}$.

Table 5.1 compares these four sets of parameters and the unsmoothed distributions. The increase of f_{SN} is calculated by dividing the maximum of the unsmoothed σ_{baseline} distribution by the maximum of the respective smoothed σ_{baseline} distribution. This does not even take into account that the full width at half maximum (FWHM) of the σ_{baseline} distribution also decreases which is an additional positive effect.

However, the waveform smoothing doesn't come for free. The benefits of a better signal-to-noise ratio, gained by raising p and w, are counterbalanced by an increase in the computation costs. Therefore,

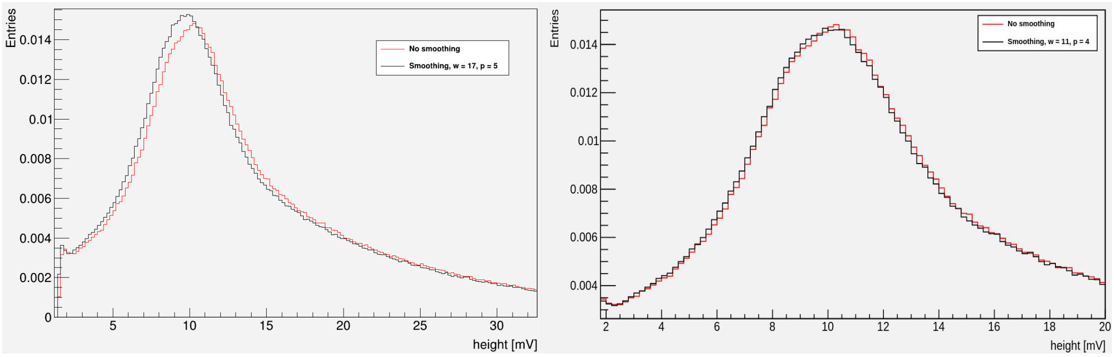

Figure 5.5 Comparisons of the normalized reconstructed pulse height distributions between smoothed and unsmoothed analyses. The red histograms are the unsmoothed data set, and the smoothed ones are shown in black. The left figure shows a smoothing parameter set - $p = 5$, $w = 17$ - which filters out signal frequencies, thereby changing the reconstructed pulse heights. The left shows a usable set - $p = 4$, $w = 11$ - which does not change the distribution.

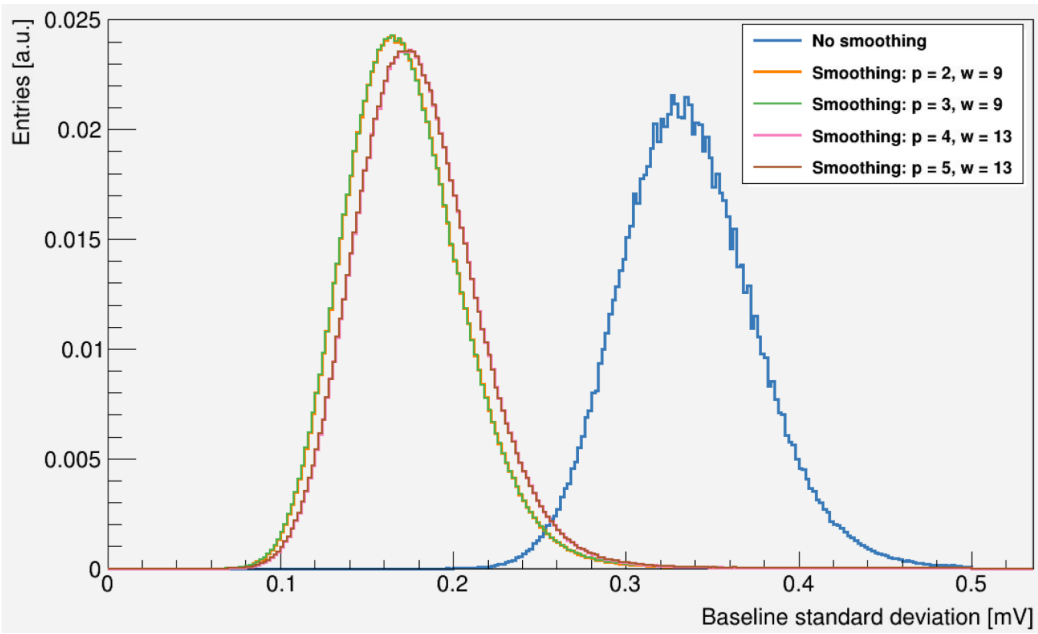

Figure 5.6 Comparison of the reconstructed baseline standard deviation σ_{baseline} distributions between the smoothing parameters listed in Table 5.1. These smoothing settings all reduce the σ_{baseline}, thereby increasing the signal-to-noise ratio f_{SN} of the reconstructed waveforms.

choosing between these sets is a balancing act between these parameters. All of these sets do not change the pulse height distributions. Additionally, the baseline mean distribution does not change, as shown in Fig. 5.7.

Ultimately, I chose the parameters $p = 2$, $w = 9$ for the SGF smoothing since it caused the smallest CPU time increase while the signal-to-noise ratio almost doubled. Better parameters for smoothing might exist, but I tested many more than listed in Table 5.1. Most of them distorted the waveforms too much or had worse improvements.

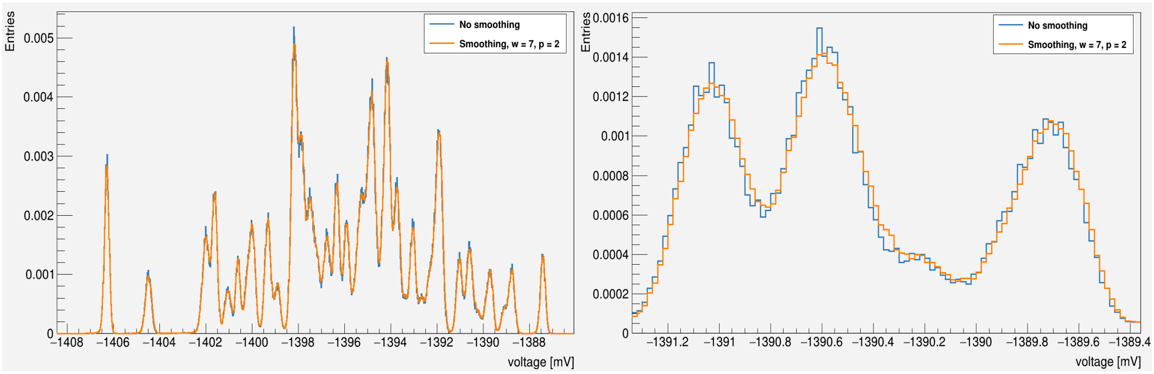

Figure 5.7 Comparison of the reconstructed baseline mean distribution between the unsmoothed and smoothed data set. The left side shows the whole spectrum. It has many peaks because the PMTs have different baselines. The right side shows the zoom into the region $-1391.2\,\text{mV}$ to $-1389.4\,\text{mV}$. Here, the smoothing parameters are $p = 2$, $w = 7$, but the distributions for the parameter sets listed in Table 5.1 are almost the same. The smoothed distribution is almost identical to the unsmoothed one.

Smoothing parameters	p=2, w=9	p=3, w=9	p=4, w=13	p=5, w=13	**no smoothing**
Maximum of σ_{baseline}	0.165	0.165	0.175	0.175	0.327
FWHM of σ_{baseline}	1.98	1.98	1.87	1.87	0.084
CPU time increase	$34\,\%$	$53\,\%$	$47\,\%$	$54\,\%$	-
f_{SN} **increase factor**	1.98	1.98	1.87	1.87	-

Table 5.1 Comparison of the effects between different SGF smoothing parameter sets on the waveform reconstruction. The σ_{baseline} distributions' values are extracted from Fig. 5.6. The CPU time increase was measured by processing the same data set containing 3.5×10^5 detector events with the RS and compared to processing without smoothing. The f_{SN} increase factor is the unsmoothed σ_{baseline} distribution maximum divided by the respective smoothed σ_{baseline} distribution maximum.

5.4 Event Reconstruction

After reconstructing the PMT pulses, the RS must collect the PMT hit signals that originated from the same energy deposition event in the LS. By finding accumulations of multiple hits in a short time window, the *clusterization* algorithm accomplishes this. Some of the pulses that occur in the EB event can arise from, e.g., the dark noise of the PMTs. These pulses would distort event information like the charge or the hit time distribution. It is also possible that two distinct energy depositions happen in one recording window. The clusterization class should also classify such cases as two events.

The clustering is done separately for ID and OD PMTs because the OD PMTs don't add information about the events happening inside the LS. They are used for vetoing and tagging of - mainly - muons.

The clusterization algorithm moves a window of $70\,\text{mV}$ over the recording window of the EB event. Since all PMT waveforms start at the same global time, which is also the start time of the EB event, this scan of the recording window includes all available information about the event. The scanning window moves $1\,\text{ns}$ forward at a time. If at least 5 reconstructed pulses have their start time in the moving window, the clusterization class starts a cluster, which is equivalent to an event. At that point, the end time of the moving window is the trigger time of a cluster, which is also the start time of a reconstructed event. Thereupon, the scanning window is extended to $280\,\text{ns}$ and continues to move over the recording window. The cluster ends when there are less than two hits in the scanning window. Hence, all pulses from the start to the end of the cluster form the cluster.

Since the recording window is $600\,\text{ns}$ long and the minimum length of a cluster is $280\,\text{ns}$, it is theoretically possible to have 2 clusters in one EB event. However, the DAQ triggers in a way that the triggering PMT hits are at least $150\,\text{ns}$ after the recording window starts. Therefore, it is rare for the RS to identify two physical events inside one EB event. If two physical events happen very close to each other in the LS, they are usually identified as only one event. This is why the RS cannot reliably detect fast coincidences like BiPo-212; see Sec. 6.1 for more information.

The clusterization algorithm can return much more information about the cluster, e.g., its end time, the time of its maximum, the total charge of all pulses etc. For the analyses in this work, these do not matter, and I will not discuss them further.

Clusterization is the step after waveform reconstruction to obtain information about the detected physical event. The event reconstruction takes the identified clusters and extracts the event time, energy, and position inside the detector. As mentioned above, the event time is the same as the cluster trigger time. E. Neuerburg implemented a maximum likelihood method based on lookup tables for the energy and position reconstruction [88]. This is used for the position determination. However, it was discovered that the energy reconstruction needs to be changed for correct results. Therefore, an event's energy is calculated as the sum of the charges of all reconstructed pulses in the cluster divided by the calibration constant $C = 220\,\mathrm{p\,e}\,/\mathrm{MeV}$.

This introduces an inaccuracy regarding the energy because it is known that the light yield per deposited energy is position- and energy-dependent (see Sec. 3.3). The collaboration is working on including the source calibration procedure in calculating the calibration constant. This work was still ongoing at the time of writing, and I had to use the above estimation.

After the event reconstruction, the necessary information for the following analyses (Capter 6 and 7) is available. The RS uses the event information to distinguish the events into BiPo-214 or single events. This is described in Sec. 6.2. One of the primary tasks of the RS is the monitoring data stream while it is coming in. This functionality is described next.

5.5 PMT and Detector Monitoring

Since OSIRIS endeavors to give out warnings when the LS quality is lacking, the data analysis must occur online. All of the previous steps happen during data-taking with every EB event. While this allows for monitoring of the radioactivity levels, it also enables detector monitoring. In this work's context, I implemented many detector health indicators. They are useful for data quality checks on the fly and - if necessary - remedy problems immediately.

For example, it can occur that some GCUs lose synchronicity with the EB. Their waveforms are then not properly forwarded and lost. Fig. 5.8a shows the EB event numbers on the x-axis and one dot at the appropriate y-axis position if the event contained a reconstructed hit in the PMT. In the case that a GCU desynchronizes, the rows of the PMTs connected to that GCU are empty in the figure. While not every PMT participates in every event, a problem appears if a whole row stays empty for a long time. Once this is observed, the person in charge of detector operation can restart the system to fix the problem.

Another potential indicator for problems is the rate of incoming EB events shown in Fig. 5.8b. It is normally very stable around $8\,\mathrm{Hz}$. The exact rate depends on the trigger condition of the DAQ. Sudden in- or decreasing rates are cause for investigation.

The RS also provides plots like the event vertex (Fig. 5.8c) or energy distribution (Fig. 5.8d). The essential rates of events identified as, e.g., BiPo coincidences, muons, etc., can also be displayed. Furthermore, waveform reconstruction value distributions for pulse height, charge, start time, end time, hit rate, and baseline mean and standard deviation are available for every PMT.

After introducing the RS functionality, I will discuss one of the most important radiopurity indicators: BiPo coincidences. I will explain what they are and how the RS tags them. Additionally, I will explain how they are the basis for investigating the PSD technique and its current applicability.

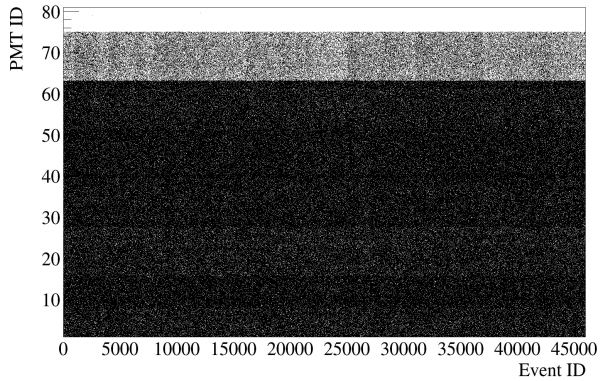

(a) The distribution of PMTs with at least one reconstructed pulse in each EB event. Since there are fewer events with fewer photons in theOD, there are fewer points in theOD PMT number rows, starting at PMT 65. In the case of problems, i.e., a GCU desynchronizing and failing to send data to the EB, the rows of the affected PMT Ids stay empty. This is easy to see and can be reported fast for fixing.

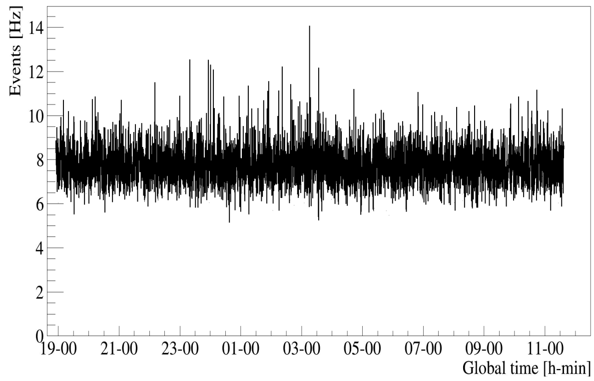

(b) The rate of EB events reaching the RS over time. Extended periods of abnormally high or low rates indicate problems.

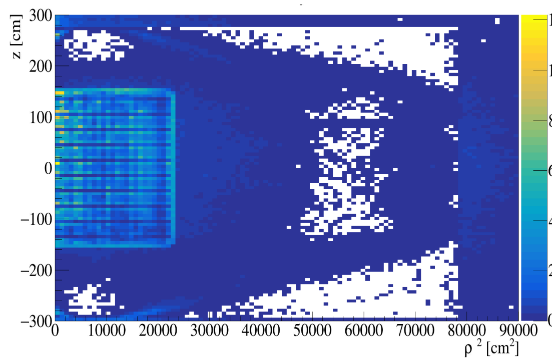

(c) The distribution of the reconstructed vertex as a function of the squared radius ρ^2 (x-axis) and the z-coordinate (y-axis). The color axis on the right shows the number of events in each bin. The rectangular in lighter colors clearly shows the outline of the detector.

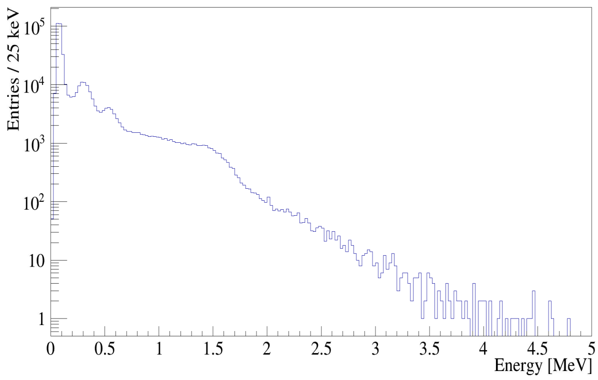

(d) The spectrum of the reconstructed energy spectrum of all processed EB events.

Figure 5.8 Examples of plots produced by the RS for monitoring the OSIRIS detector as shown in the detector graphical user interface.

Chapter 6

Liquid Scintillator Radiopurity Analysis in OSIRIS

The purpose of the OSIRIS detector is to consistently monitor the LS for impurities during the filling of the JUNO CD. Isotopes starting long-lived decay chains are especially dangerous since they cannot be removed from the detector once introduced. OSIRIS will alarm the filling to be stopped if the contamination is too high. In Sec. 6.1, I describe the detection strategy to find one of the mother isotopes of such a *primordial decay chain*, ^{238}U . Sec. 6.2 lays out the data set I use in all following analyses. Lastly, I report the prospects of using PSD techniques to help with event identification between α- and β-events in Sec. 6.3.

6.1 The Uranium and Thorium Decay Chains

^{238}U is the start of one of a long-lived decay chain. Fig. 6.1 shows the isotopes with the largest branching ratios of the chain, their decay modes, and half-lives. Similarly, Fig. 6.2 shows the ^{232}Th decay chain. Due to their extremely long half-lives of $\tau_{\mathrm{U}} = 4.468 \times 10^{9}$ years and $\tau_{\mathrm{Th}} = 1.40 \times 10^{10}$ years ^{238}U and ^{232}Th , respectively, are still present in considerable quantities on Earth. They are produced in stars via the *r-process* [89]. Consequently, all the daughter isotopes are also present in all materials containing ^{238}U. The complex nature of the decay chains and the fact that one cannot 'wait out' the decay of the present uranium or thorium atoms is of major concern in rare-event search experiments like JUNO.

The knowledge of the ^{238}U and ^{232}Th contaminations in the detector is of utmost importance for JUNO's background evaluation. Avoiding the introduction of significant amounts of uranium or thorium is even more important. OSIRIS is JUNO's warning system if the LS, which is about to be filled into the CD, contains threatening levels of uranium, thorium, and other radioactive isotopes.

Since the mother isotope's half-life is much longer than any daughter's, the secular equilibrium equation can be exploited to determine the amount of ^{238}U or ^{232}Th present from the daughter isotope's concentration [90]. This is only possible if none of the daughters is introduced externally, thereby breaking the equilibrium. Under this condition, $N_U \lambda_{\mathrm{U/Th}} = N_d \lambda_d$ holds, where $N_{\mathrm{U/Th}}$ and N_d are the numbers of uranium/thorium and the observed daughter's atoms, respectively, and $\lambda_{\mathrm{U/Th}}$ and λ_d are the decay constants of uranium/thorium and their daughter isotopes, respectively.

Towards the ^{238}U chain's end, we see the β-decay of ^{214}Bi with a half-life of $19.9\,\mathrm{min}$ followed by the α-decay of ^{214}Po with a half-life of only $164\,\mu$s. These two decays have a clear coincidence structure: The decays are separated by a short time difference, and the second (delayed) event has a defined energy because it is an α-decay, which is mono-energetic. By noting that $N_{Po}\lambda_{Po} = N_U \lambda_U = R_{Po}$, where R_{Po} is the observed rate of ^{214}Po decays, we can determine the ^{238}U concentration n_U to be

$$n_U = \epsilon \cdot N_U \lambda_U \frac{M_U}{M_{tot}} = \epsilon R_{Po} \frac{M_U}{M_{tot}}, \tag{6.1}$$

where we introduced $\lambda_U = 4.916 \times 10^{-18}\,\mathrm{s}^{-1}$, the mass of the ^{238}U atom $M_U = 3.95 \times 10^{-25}$ kg, the total mass of LS in OSIRIS $M_{tot} = 18\,$ton, and the efficiency ϵ of detecting BiPo coincidences in the detector.

We can use an equivalent approach to determine the ^{232}Th contamination. However, the half-life of ^{212}Po is much shorter, $T_{1/2} = 300$ ns. The recording window of the DAQ is 600 ns and the pretrigger windows 150 ns, therefore, a significant amount of these coincidences have both decays in one recording window which the current algorithm cannot untangle. Additionally, events in the pretrigger window cannot be triggered, making it an effective deadtime window. Unfortunately, the waveform and cluster reconstruction algorithms of the RS cannot reliably disentangle signal clusters below approximately 600 ns yet.

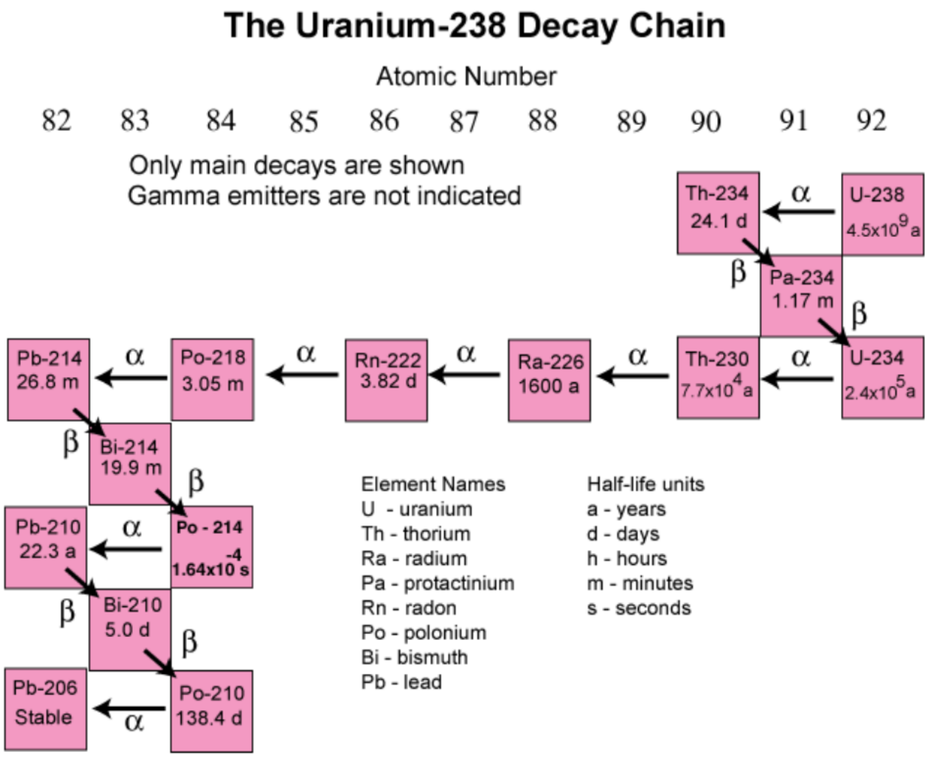

Figure 6.1 The ^{238}U decay chain with its most important isotopes. Source: [91]

One of the main roadblocks for determining the detector's sensitivity to ^{238}U is ^{222}Rn (and ^{220}Rn in the case of ^{232}Th). Due to its inertness and abundance in the air and the many materials from which it can emanate, it can be easily introduced into the detector. Filling and/or circulating LS in the liquid handling system of a detector typically brings a lot of this isotope into the detector [93]. Since ^{222}Rn is also part of both decay chains, introducing ^{222}Rn from other sources disturbs the secular equilibrium between the remaining decay chain and the mother isotopes. This makes the calculation of the ^{238}U and ^{232}Th concentrations in the LS impossible if the amount of externally injected ^{222}Rn is unknown. Therefore, one has to wait until enough external Radon has decayed to reach the detector's sensitivity threshold and/or the level of the ^{238}U concentration. In the case of OSIRIS, the waiting time is multiple weeks.

6.2 OSIRIS Data Set Between 1 June and 26 July 2024

The OSIRIS group filled the detector with LS in the first half of March 2024. On 11 March, the first data of the fully filled detector arrived. In the following months, the main goal was to demonstrate stable detector operation and determine the radiopurity of purified batches of the JUNO LS. Simultaneously, we worked on testing and deploying the various subsystems, such as the calibration units, detector surveillance, and online data monitoring, without interrupting data acquisition.

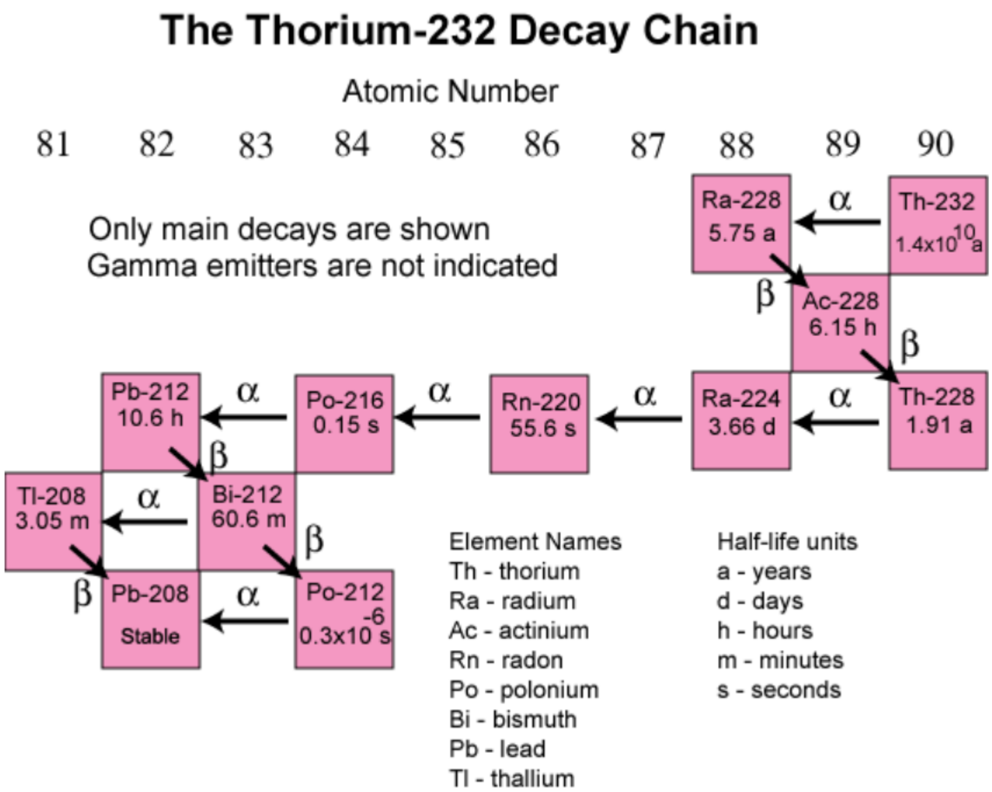

Figure 6.2 The ^{232}Th decay chain with its most important isotopes. Source: [92]

As described in Sec. 6.1, each LS filling or flushing operation introduced external ^{222}Rn , which had to decay before the intrinsic radiopurity of the LS or the sensitivity threshold of the detector could be calculated. The OSIRIS group performed multiple LS exchanges and flushings since March 2024.[1]

This work only considers data taken between 1 June and 26 July. Table 6.1 shows the detector operations that affected the LS in the AV directly around this time period.
AV circulation means that LS is pumped through the circuit formed by the AV, the buffer tank, and the head tank. This means that no new LS is introduced into the system. However, the LS entering the AV during the circulation usually contains more ^{222}Rn than LS, which had stayed inside the AV for an extended period of time. The radon can enter the LS by emanation from, e.g., the piping or if there are leaks in the system [94].
LS exchange refers to introducing new, e.g., freshly purified, LS. These batches normally also contain more ^{222}Rn for the same reasons.

I processed all valid data sets between 1 June and 26 July, 120 data sets in total, with the RS by applying the following selection criteria to identify BiPo-214 coincidences:

1. The time difference between two consecutive events must be within $5\,\mu$s to $1640\,\mu$s. The lower limit serves to exclude BiPo-212 coincidences. The upper limit equals ten half-lives of ^{214}Po .

2. The visible energy of the prompt β-event must be in the interval [0.2, 2.15] MeV. This covers the entire β-spectrum of the ^{214}Bi decay except for the lowest energies. The lower limit excludes accidental coincidences, primarily of ^{14}C , whose energy spectrum ends at 0.2 MeV.

3. The visible energy of the delayed α-event from the ^{214}Po decay must be in the interval [0.4, 0.7] MeV (see Sec. 7.1).

[1]However, the OSIRIS group is still investigating at the time of writing which operations introduce high amounts of ^{222}Rn into the detector because it seems similar operations introduce differing amounts (compare Table 6.1 to the BiPo rate evolution, Fig. 7.3).

Date	Operation	Additional notes
31 May	AV circulation	Duration: 2.2 h, circulated volume: 2 m^3
2 June	AV circulation	Duration: 2.5 h
18 June	AV circulation	Duration: 1 h
20 June	AV circulation	Duration: 1.75 h
21 June	AV circulation	Duration: 6 h
2 July	AV circulation	Duration: 5.75 h, circulated volume: 6 m^3
9 July	AV circulation	Duration: 4 h, circulated volume: 160 L
10 July	3 AV circulations	Total duration: 18 h, circulated volume: ca. 1300 L
11 July	2 AV circulations	Total duration: 4.5 h, circulated volume: 275 L
12 July	2 AV circulations	Total duration: 4.25 h, circulated volume: 275 L
14 July	AV circulation	Duration: 0.25 h, circulated volume: 175 L
15 July	LS exchange	Exchanged volume: 175 L

Table 6.1 Operations performed on the OSIRIS detector between 31 May and 26 July. Unfortunately, the circulated LS volume couldn't be recovered for some operations for which the respective value is missing in the table.

4. A fiducial volume cut restricts the volume in which the events can take place to 1.45 m out of 1.5 m in radius as well as in the absolute value of the z-coordinate. This cut covers $90.3\,\%$ of the AV's volume.

5. The data selection does not include a muon cut. However, the direct muon events produce too much light to survive the energy cuts of the BiPo or singles (see Sec. 7.2) analyses. The muons might induce cosmogenic backgrounds, which are neglected in this work.

If a pair of events was not identified as a BiPo coincidence and the second event happened more than 2 ms after the first, the RS categorized the first event as a single event (see Sec. 7.2).

Fig. 6.3 shows the time difference distribution between the first and second event of coincidences that the RS labeled as a BiPo event. Fitting this distribution with the function $f(t) = N \cdot e^{-\lambda t}$, we expect that λ is the decay constant of ^{214}Po $\lambda_{214Po} = 4.218 \times 10^3$ s^{-1}. The fit returns the best-fit values $N = 5381.06 \pm 22.91$ and $\lambda = (4.2410 \pm 0.0129) \times 10^3$ s^{-1}. The goodness-of-fit $\chi^2/\mathrm{NDF} = 1.65$.

The fit value of λ is 1.71 times the fit uncertainty off the theoretical value, and the goodness-of-fit is not excellent. However, the fit underestimates the data at higher time differences, which is unsurprising but causes the fit value of λ to increase. The larger the time window in which a coincidence can occur, the higher the probability of accidental coincidences.

A different approach is to fit with an exponential plus a constant; see Fig.6.3b. While the fit with the additional constant fits the data better, its decay constant is roughly four-and-a-half times its uncertainty off the expected value. The goodness-of-fit is not perfect ($\chi^2/\mathrm{NDF} = 1.48$), but better than without the constant ($\chi^2/\mathrm{NDF} = 1.65$).

Both fits return a decay constant close to the theoretical value. I apply no additional cuts to clean the data at bigger time differences. Additionally, all the analyses that follow have tighter time difference cuts. Therefore, I conclude that the RS is effective at finding BiPo events. The RS can run with these cuts, making it an excellent tool for selecting BiPo-214 coincidences.

6.3 Studies on the Feasibility of Pulse Shape Discrimination

As described in Sec. 3.5, the pulse shape is defined as the time profile of the emission of photons following an energy deposition in the LS. The pulse shape differs for different particles depositing the energy. The possibility of applying PSD is one of the most advantageous properties of LS detectors. Many experiments have employed PSD to differentiate between various event classes, e.g., alpha/beta [95],

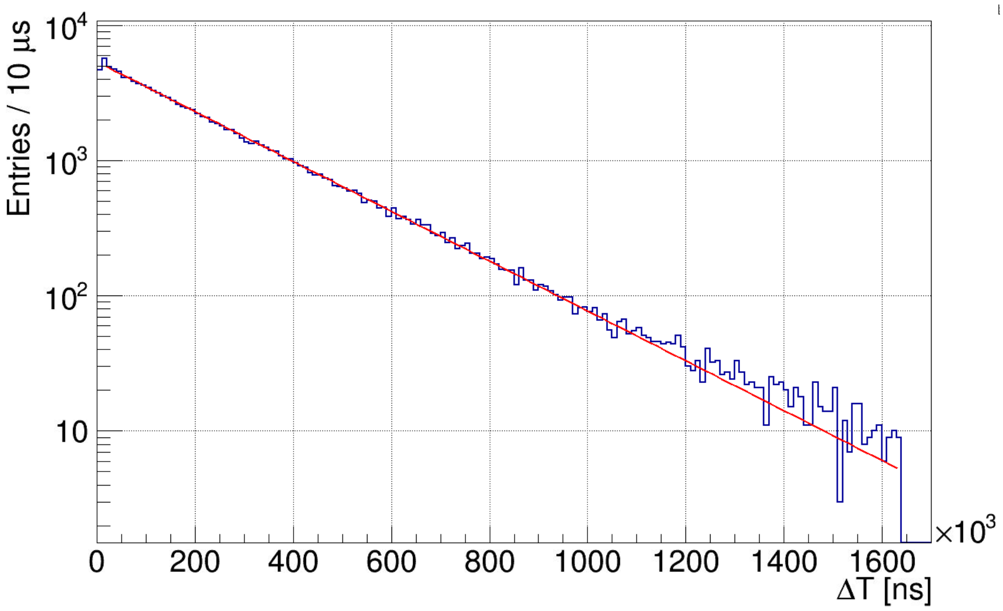

(a) The fit function $f(t) = N \cdot e^{-\lambda t}$ is shown in the red line. N and λ are the free parameters. The best-fit values are $N = 5381.06 \pm 22.91$ and $\lambda = (4.2410 \pm 0.0129) \times 10^3\,\mathrm{s}^{-1}$. The goodness-of-fit $\chi^2/\mathrm{NDF} = 1.65$.

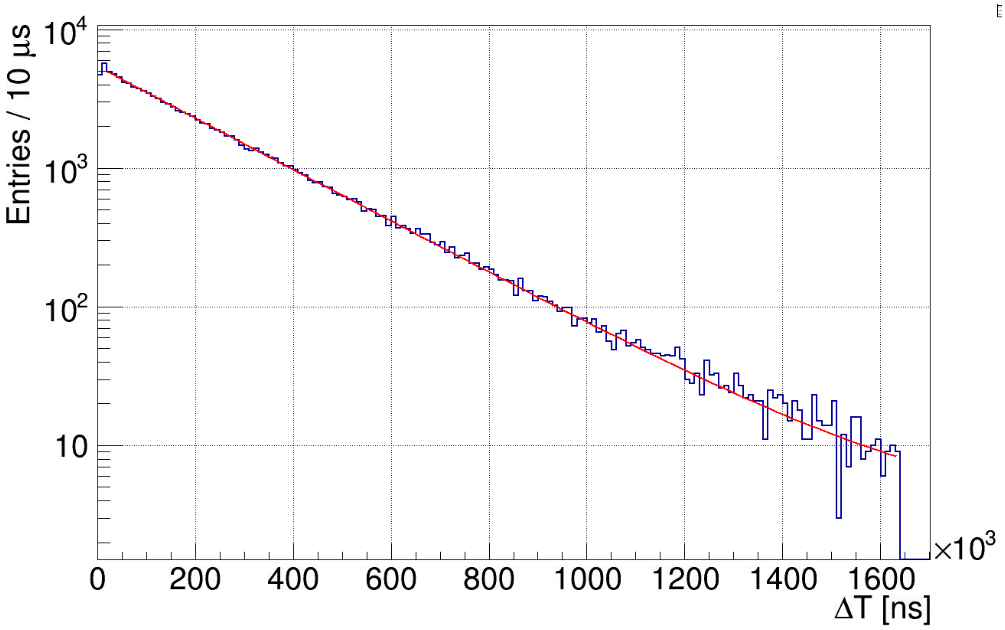

(b) The fit function $f(t) = N \cdot e^{-\lambda t} + C$ is shown in the red line. N, C, and λ are the free parameters. The best-fit values are $N = 5420.06 \pm 22.91$, $C = 3.415 \pm 0.630$ and $\lambda = (4.2890 \pm 0.0157) \times 10^3\,\mathrm{s}^{-1}$. The goodness-of-fit $\chi^2/\mathrm{NDF} = 1.48$.

Figure 6.3 The distribution of the time difference between the prompt and delayed event of coincidences identified as BiPo events by the RS. The theoretical decay constant of ^{214}Po is $\lambda = 4.218 \times 10^3\,\mathrm{s}^{-1}$. (a) and (b) show two different fit functions. While the fit with the additional constant (b) fits the data much better, its decay constant is roughly four-and-a-half times its uncertainty off the expected value. The fit without the constant is only off by less than two times the uncertainty.

electron/gamma [96], electron/neutron [97]. Recently, efforts have focused on applying machine learning techniques [98, 99]. While the PSD capabilities depend heavily on the detector itself and not only on the LS properties, OSIRIS can provide a first look at the performance of the JUNO LS.

I will describe the investigation of the feasibility of PSD in OSIRIS in the following.

6.3.1 Pulse Shape Parameters

In this work, I investigate two methods and compare their PSD performances: the so-called Gatti and tail-to-total (T2T) parameters. In the following, the pulse shape of an event is the signal registered by the detector as a function of time. For the different methods, the signal of an event can be obtained from the data described in Sec. 6.3.2.

I acquire a set of α- and β-decays from the previously described BiPo coincidences. For these, the prompt event is always a β- and the delayed one an α-decay.

The *Gatti* method is defined by the following procedure [100]: We define the average pulse shapes of α- and β-events to be $\overline{\alpha}(t)$ and $\overline{\beta}(t)$, respectively. We separate the signal into discrete steps of length ΔT, where α_i and β_i are the signals of α- and β-events in the ith step. We can define the Gatti weights in each step i as

$$P_i = \frac{\overline{\alpha}_i(t) - \overline{\beta}_i(t)}{\overline{\alpha}_i(t) + \overline{\beta}_i(t)}. \tag{6.2}$$

Multiplying any signal $S(t)$, which is the series of S_i, of unknown origin by the weights P_i and taking the sum over all steps yields the Gatti value of the signal:

$$G = \sum_i S_i \cdot P_i. \tag{6.3}$$

It was shown that the G values form distributions around a positive mean value for α-events and a negative mean value for β-events [100]. This only works if the signals are normalized w.r.t. the charge (area) of the signal. Additionally, the signal must be fully contained in the recording window, i.e., the tail of the signal must reach zero.

The T2T method employs the signal's charge information. We define the signal's tail Q_{tail} as the charge (area) of the signal $S(t)$ from some point in the time window W. The total charge Q_{total} is the integral over all N steps of the signal. Since, in our case, the DAQ always records the signal in discrete steps of length Δt, the charges are:

$$Q_{\text{total}} = \sum_{i=0}^{N} S_i \cdot \Delta t \tag{6.4}$$

$$Q_{\text{tail}} = \sum_{i=W}^{N} S_i \cdot \Delta t \tag{6.5}$$

The T2T value T is then

$$T = \frac{Q_{\text{tail}}}{Q_{\text{total}}}. \tag{6.6}$$

Normalizing the signal is unnecessary, but all signals must be shifted to the same starting time inside their recording window.

6.3.2 Data Set and Event Signal Definitions

Data set

We need events we know are α- or β-events to investigate the PSD capabilities. I used the data set defined above (Sec. 6.2) for this analysis but applied additional cuts. The RS acquired BiPo coincidences by demanding that the two events are to have a temporal separation in the interval of $5\,\mu s$ to $1640\,\mu s$. Additionally, the β- (prompt) event's energy must be between 0.2 MeV to 2 MeV and the α- (delayed) event's between 0.4 MeV to 0.7 MeV (see Sec. 6.2).

These cuts are very general and almost certainly include background events (see the discussion in Sec. 6.2). Additionally, PSD parameter distributions are known to be energy-dependent [101]. Furthermore, the α-energy is a mono-energetic line; hence, we only need to investigate events in the α-energy range. Lastly, the fiducial volume cut (on the radial and z-position of the reconstructed event vertex r and z) is much more restrictive for the reasons below. Therefore, I adjust the cuts to be:

$$
\begin{aligned}
\Delta T &\in [5\,\mu\text{s to } 500\,\mu\text{s}] \\
E_{\text{prompt}} &\in [0.4\,\text{keV to } 0.7\,\text{keV}] \\
E_{\text{delayed}} &\in [0.4\,\text{keV to } 0.7\,\text{keV}] \\
r_{\alpha/\beta} &\in [0\,\text{cm to } 55\,\text{cm}] \\
z_{\alpha/\beta} &\in [-55\,\text{cm to } 55\,\text{cm}]
\end{aligned}
$$

In addition to these cut adjustments, a new selection was introduced to only keep events with the start time between $[200\,\text{ns to } 300\,\text{ns}]$ of the recording window. This cut removes noise events and secondary events in the same recording window.

The PSD analysis relies on the knowledge of the start time of the events' pulse shapes; for the Gatti analysis, the average pulse shape only makes sense if the single pulse shapes that contribute to it are normalized. For the T2T analysis, the tail definition is relative to the start of the pulse shapes. Therefore, all pulse shapes for both PSD procedures are shifted such that the cluster start time calculated by the RS is at 200 ns.

This creates an artifact in the data, which can be seen in, e.g., Fig. 6.4: the hit time distribution has a single very high bin at 200 ns. This appears because the cluster start time calculated in the RS - on which all pulse shapes are aligned - is defined as the hit time of the first photon in the cluster of hits that make up the event. Therefore, every cluster - equivalent to an event or a pulse shape - must have a hit at the cluster start time, resulting in this abnormally high outlier bin. I have tried a different pulse shape alignment strategy by choosing each event's highest bin as the alignment time. However, this decreases the PSD performance and will not be discussed further.

Event signal definition: hit time distribution

An event's signal coming from the detector is the collection of all waveforms of all PMTs. As discussed in Sec. 5.4, after a trigger, the DAQ sends the waveforms of all PMTs forward, regardless of whether the waveform contains a PMT-level trigger. The RS searches for pulses caused by detected photon hits in all waveforms of one event and labels the collection of all hits an event if the trigger conditions described in Sec. 5.4 are met. Therefore, each event is comprised of many PMT hits. In many experiments, e.g., the CTF [95], an event's pulse shape can be constructed as the distribution of hit times over time of all PMT hits making up the event. This is the *hit time distribution*.

Naively, we expect that the temporal resolution and the number of photons emitted in an event will be such that all registered photons can be identified individually. Then, we can assign a hit time for each photon. The hit time distribution only represents the true pulse shape if all - or at least most - photon hits are resolved. As seen in Sec. 5.2, this is unfortunately not the case with the currently implemented waveform reconstruction algorithm in the RS. If the PMT hits are too close together, the combined signal of all hits is reconstructed as a singular hit. This impacts the pulse shape construction and decreases the PSD performance, as shown in Fig. 6.4.

Fig. 6.4a shows the hit time distribution when the β-energy reaches up to 1 MeV. The β-spectrum shows a dip around 245 ns because of the higher energy events, which increase the probability of PMTs being hit by many photons in quick succession. These hits cannot be resolved and distort the spectrum. Similarly, Fig. 6.4b shows the hit time distributions for the data if no fiducial volume cut is applied. Then, the α- and the β-spectra exhibit the dip around the same time. Without the spatial cut, both particle types can have events close to one side of the detector. This, again, leads to a higher probability of PMTs being hit by many photons at once, which cannot be resolved. Avoiding this is one of the reasons for the much more rigorous fiducial volume cut.

Event signal definition: cumulative waveform

Another approach to constructing the pulse shape of an event is to add up all PMT waveforms of the event sample-by-sample. I call this a *cumulative waveform*. This approach's advantage is that it circumvents the problems of the waveform reconstruction's limitations. By adding the waveform signals, all of the information therein is retained. The disadvantage is that PMT effects like the transit-time spread smear out the true hit time of the registered photons and, thereby, the photon emission profile of the event.

In this analysis, the RS calculated the cumulative waveform of each event. First, the RS summed the waveform sample values of all waveforms for all samples. Secondly, it divided all resulting sample values by the number of waveforms. Since all the PMT waveforms are forwarded to the RS, even those without any hits inside, the cumulative waveform can be calculated in two ways. For the cumulative waveform construction, the RS can use only waveforms with reconstructed hits inside or all waveforms. I discovered that there is no difference in the result.

I investigated PSD with the hit time distribution and the cumulative waveform pulse-shape construction methods, as described below.

6.3.3 PSD with Cumulative Waveform Pulse Shapes

The cumulative waveform PSD performance analysis includes the T2T and the Gatti method. In the following, I will use *pulse shape*, *cumulative waveform*, and *waveform* interchangeably to refer to the cumulative waveform pulse shape.

Gatti PSD with cumulative waveform pulse shapes

The Gatti method requires an average cumulative waveform pulse shape for α- and β-events. Multiple approaches are possible to construct the average cumulative waveform pulse shape. Since this average pulse shape must be normalized, normalization by pulse charge or pulse height is possible. One can first sum all waveforms sample-by-sample and then normalize the result. Alternatively, one can first normalize each waveform, then sum all, and then normalize again. I will call these methods 'sumFirst' and 'normalizeFirst,' respectively. This results in four different sequences of constructing the average pulse shape.

To measure each sequence's impact, I calculate the average waveform sample-by-sample. Then, I determine the standard deviation of each sample. The smaller the standard deviation, the more precise the constructed average waveform, which is desirable. This is especially the case for the peak itself and its falling flank because it encodes the time profile of the scintillation light emission process.

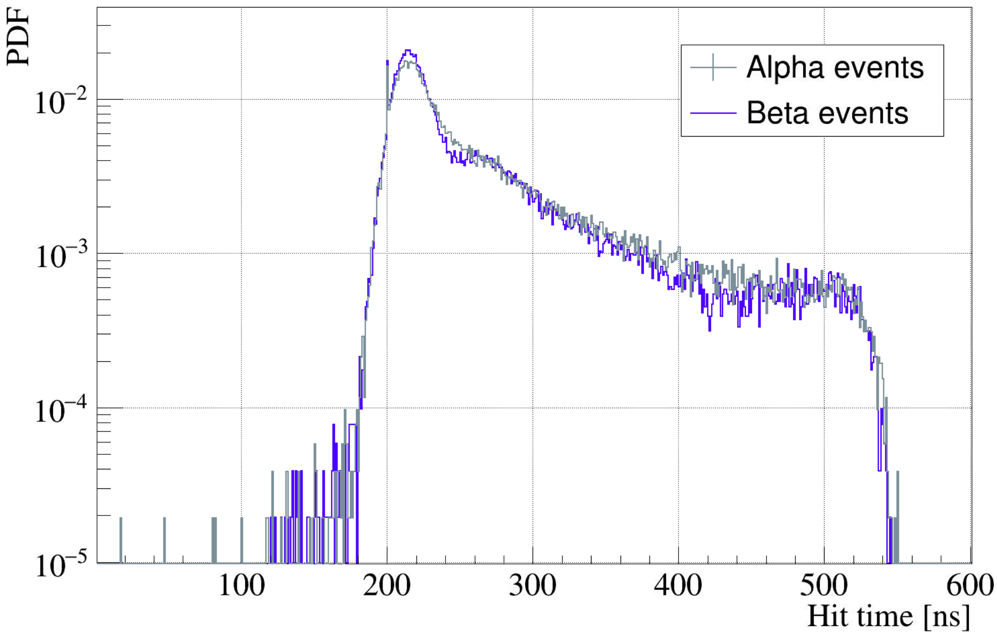

(a)

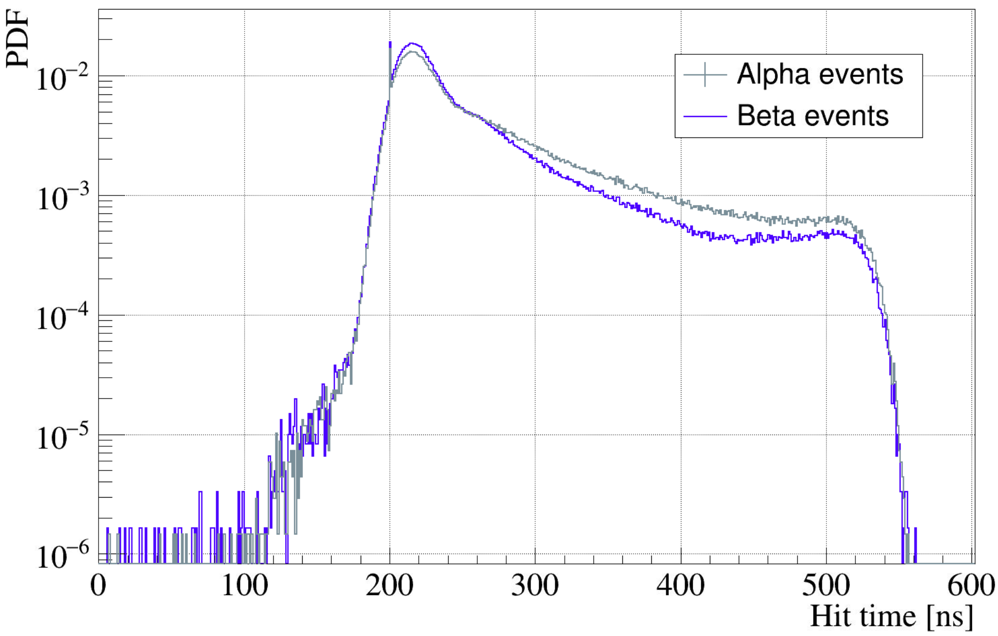

(b)

Figure 6.4 These figures show the impact of insufficient cut parameters on the hit time distributions of α- and β-events. (a) shows tha data set where the β-energy is allowed to reach 1 MeV. (b) depicts the hit time distribution if no fiducial volume cut is applied. We notice that both distributions exhibit a dip around 240 ns to 250 ns. The reason is the inability of the waveform reconstruction to resolve photon hits that are too close together.

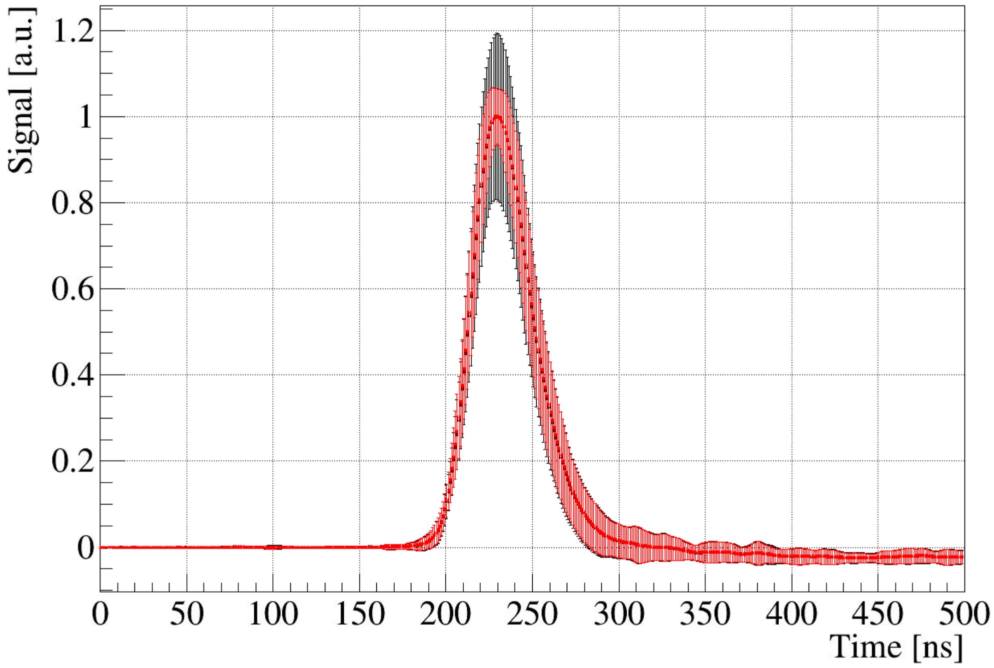

(a) The comparison between the construction by normalizeFirst (red) and sumFirst (black). Since the red band is narrower at every point, I choose to normalize every waveform before summing them to create the average waveform.

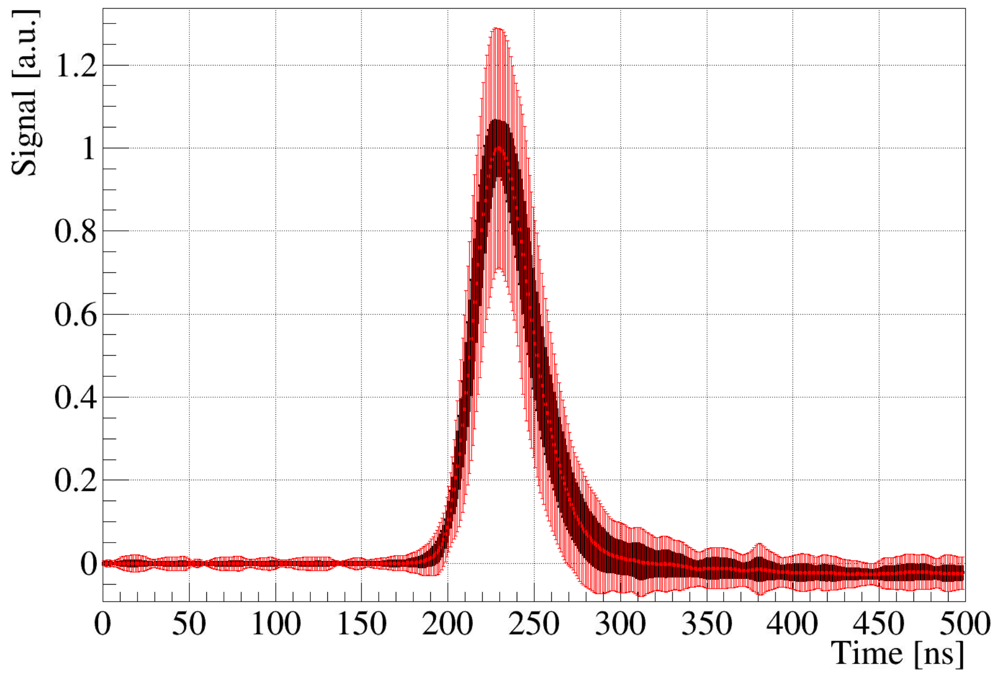

(b) The comparison between the normalization by charge (red) and height (black). Since the black band is narrower at every point, I normalize every waveform by height.

Figure 6.5 Comparisons between two methods of constructing the average cumulative waveform pulse shapes. The bands show the standard deviations.

Fig. 6.5 shows the differences between the methods. The methods behave similarly for α- and β-events; therefore, I show only the comparison for β-events. Similarly, considering sumFirst and normalizeFirst doesn't depend on whether charge or height normalization is used. The same is true for the reverse choice between charge and height normalization, which is the same for normalizeFirst and sumFirst.

Fig. 6.5a compares the differences between sumFirst (black) and normalizeFirst (red). The bands show the standard deviations. The red pulse shape is narrower everywhere or at least as narrow as the black one. This means that it is beneficial to use the sumFirst method.

Fig. 6.5b displays the charge (red) and height (black) normalization methods. The height normalization outperforms the charge method significantly. Therefore, I choose the height normalization.

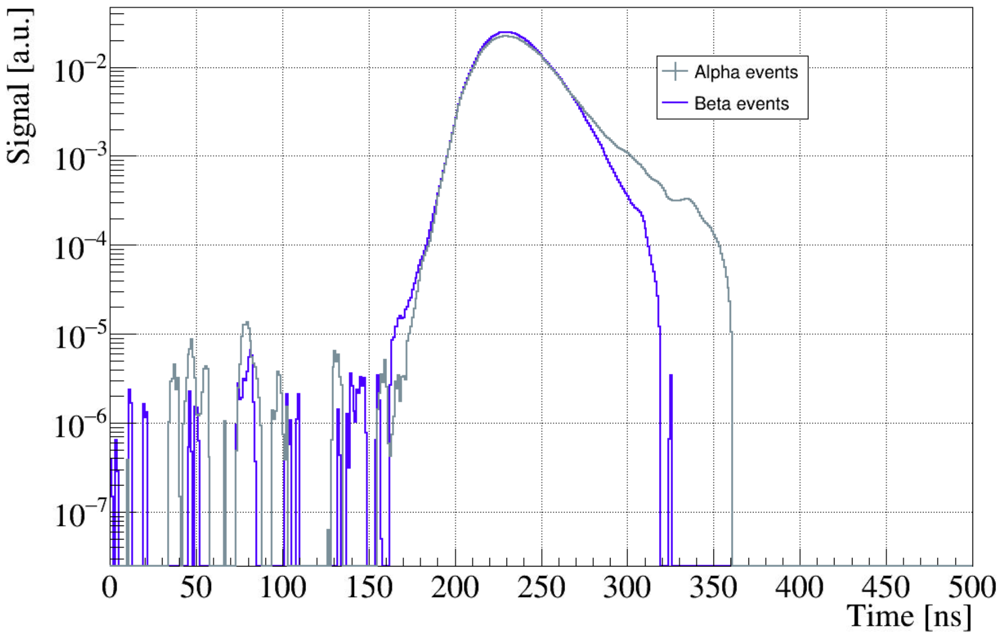

Figure 6.6 The normalized average cumulative waveform pulse shapes for α- (grey) and β-events. The first and last 150 ns are dominated by baseline fluctuations.

In summary, the average cumulative waveform pulse shape is constructed by normalizing each waveform by height first and then sum. Fig. 6.6 shows the resulting average pulse shapes for α- (grey) and β-(blue) events. As expected, the α-waveform has a much longer tail.

Using these average waveforms, we can now determine the Gatti weights of each sample as defined above in Eq. 6.2. Then, following the procedure described above, the distribution of Gatti values of the investigated waveforms arises, as shown in Fig. 6.7a. There is no separation between the distributions of α- (grey) and β-events (blue). To illustrate this point further, Fig. 6.7b shows the surviving fraction of events as a function of the Gatti value. I define survival as the pulse shape having a Gatti value above the threshold, which makes it an α-event. Events below, therefore, are labeled as caused by β-particles. The additional brown line represents the survival probability difference between α- and β-events. Compared to, e.g., [95], this PSD performance is tiny and insufficient as an additional cut parameter for event identification.

Tail-to-total PSD with cumulative waveform pulse shapes

The T2T PSD needs less setup than the Gatti method. We only need to define at which time the tail starts. After investigating the resulting PSD performance for tail definitions in steps of 5 ns, I found that the best performance results from the definition of the tail at 290 ns. Fig. 6.8a shows the T2T value distributions for the two particle types. Compared to Fig. 6.7a, we observe a much better separation; however, there is still a large overlap. Fig. 6.8b shows the resulting survival probabilities. Again, 'surviving' pulse shapes are defined as α-events with higher T2T values than the threshold, and β-events have lower values.

For example, at a cut value of slightly above zero, roughly $95\,\%$ of β-events would be rejected, and around $60\,\%$ of α-events accepted. This $60\,\%$ would be the PSD detection efficiency and the $5\,\%$ surviving electron events the background contamination.

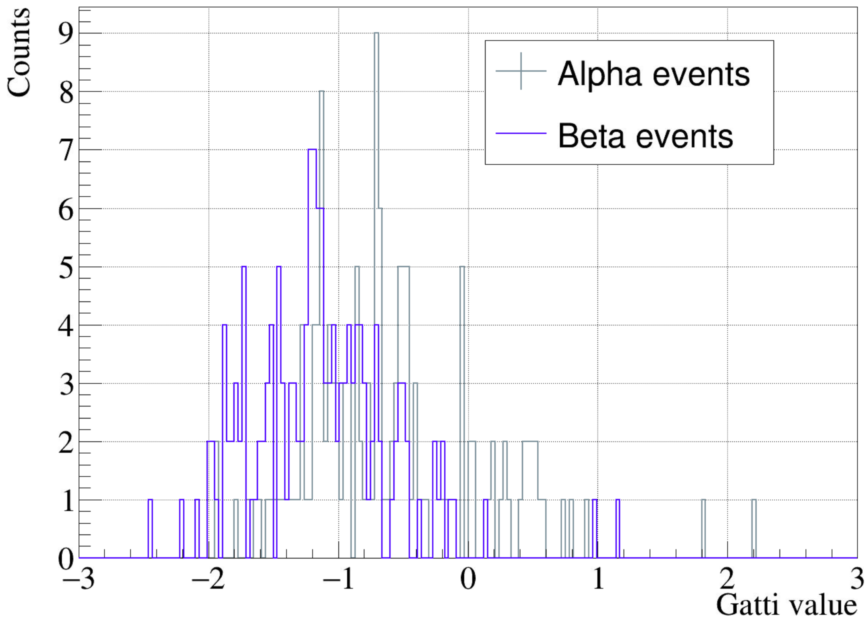

(a)

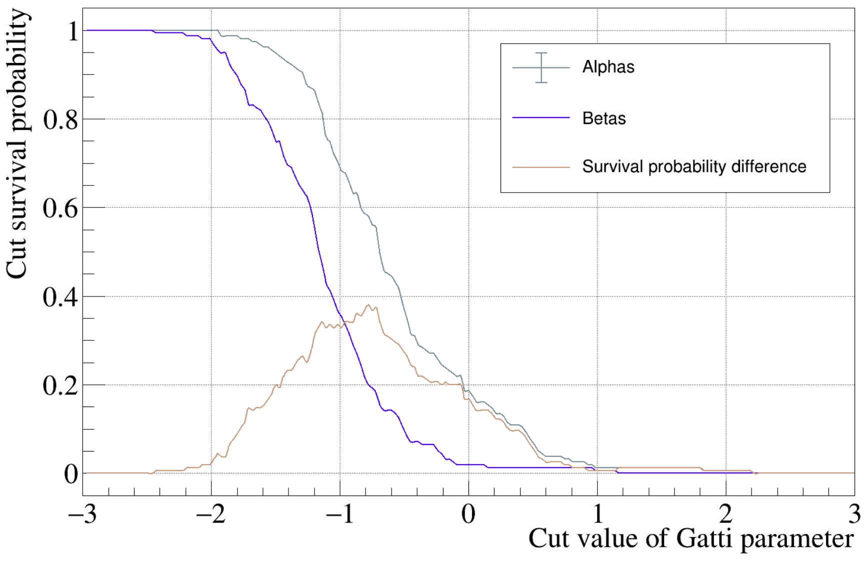

(b)

Figure 6.7 The results of the Gatti PSD method with cumulative waveform pulse shapes. (a) shows the distributions of Gatti values of all investigated events for α- (grey) and β-particles (blue). There is no separation of the distributions. Therefore, this method is not useful for PSD. (b) shows the surviving fraction of events as a function of the threshold value of the Gatti parameter. α-events (grey) have larger Gatti values than the threshold, and β-events (blue) have smaller ones. Electron events with Gatti values higher than the threshold would be misidentified as α-events. α-events with lower values than the threshold would be falsely discarded when applying a PSD cut. The brown line shows the difference of the surviving fraction of α- and β-events.

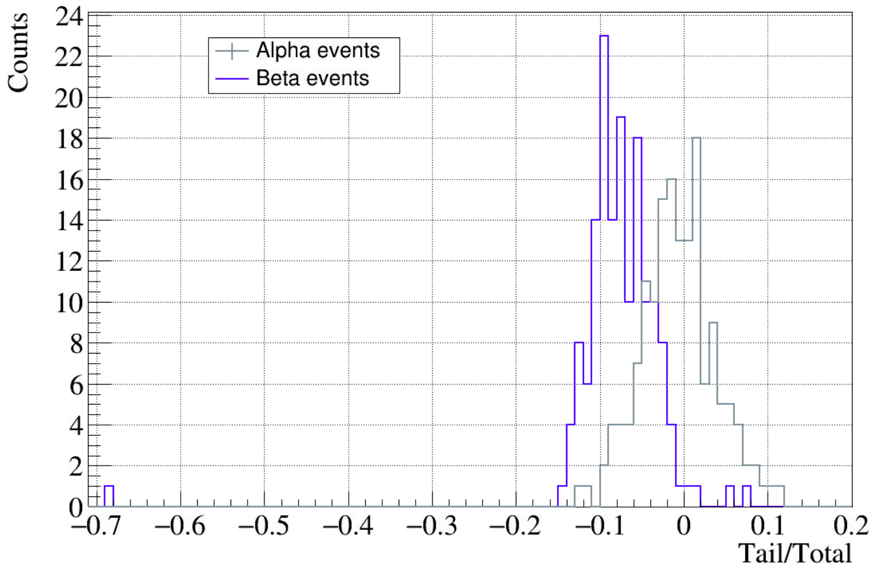

(a)

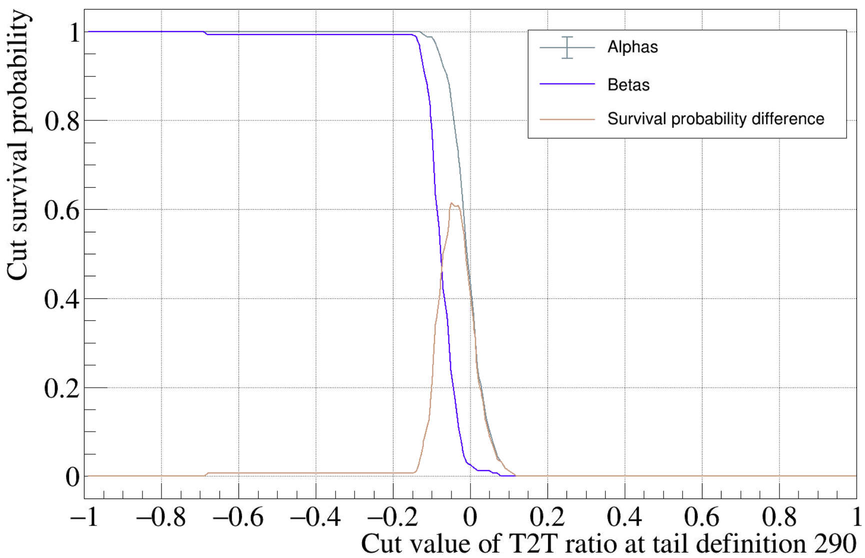

(b)

Figure 6.8 The results of the T2T PSD method for cumulative waveform pulse shapes. (a) shows the distributions of the tail/total ratios of α- (grey) and β-events (blue). The separation is much better than that of the Gatti method. (b) shows the surviving fraction of the two event populations (see description of Fig. 6.7b). The brown line shows the difference of the surviving fractions. It indicates that a survival difference of up to $60\,\%$ is possible.

6.3.4 PSD with Hit Time Distribution Pulse Shapes

I present the PSD performance analysis with hit time distributions only for the T2T method. As for the cumulative waveform method, the Gatti procedure is much worse and offers no additional insight.

Fig. 6.9 shows the hit time distributions of α- and β-events with a linear (Fig. 6.9a) and logarithmic (Fig. 6.9b) y-axis. The resulting T2T value and cut survival probabilities are shown in Fig. 6.10. Fig. 6.10a shows a slightly better separation than Fig. 6.8a, which is confirmed by the cut survival evolution Fig. 6.10b to be $70\,\%$ versus $60\,\%$.

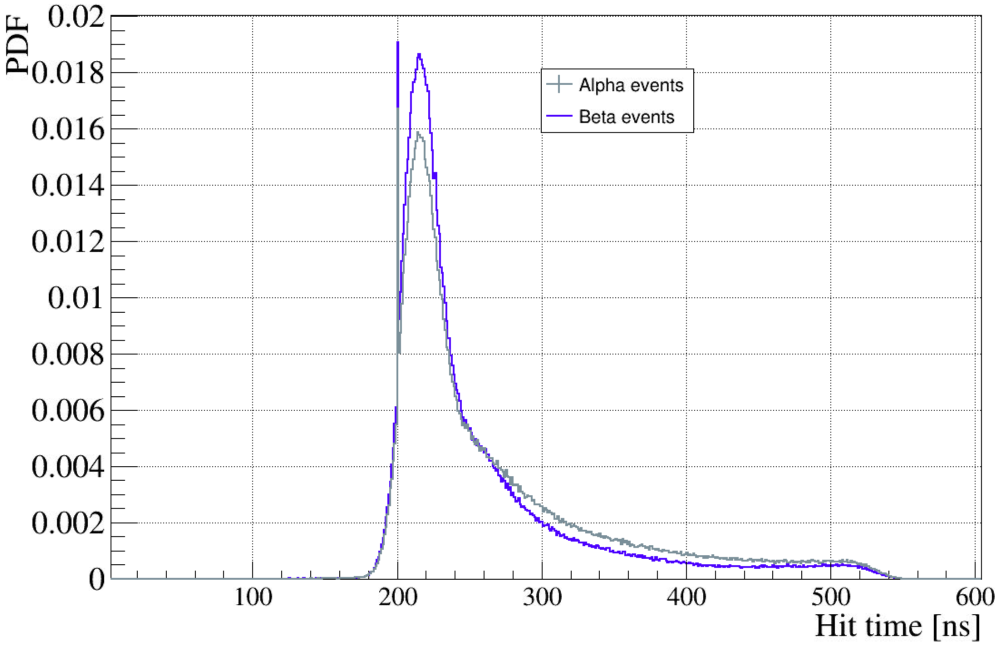

(a)

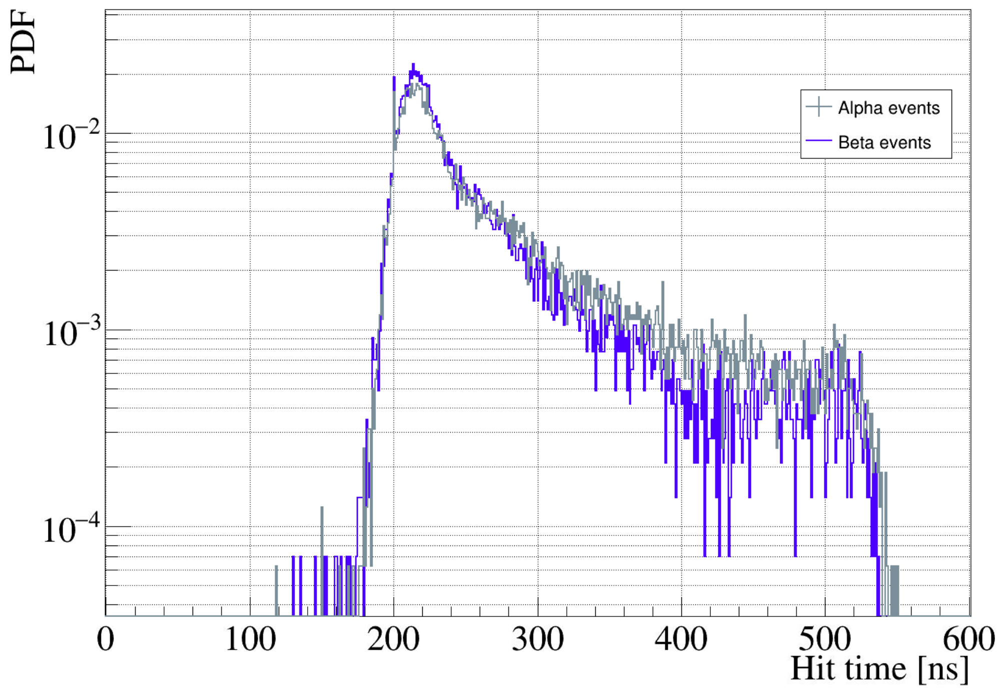

(b)

Figure 6.9 The hit time distributions of α- (grey) and β-events (blue). (a) shows the distributions with a linear and (b) logarithmic y-axis. The very high bin at $200\,\mathrm{ns}$ originates from the event start time calculated by the event reconstruction of the RS (see Sec. 6.3.2).

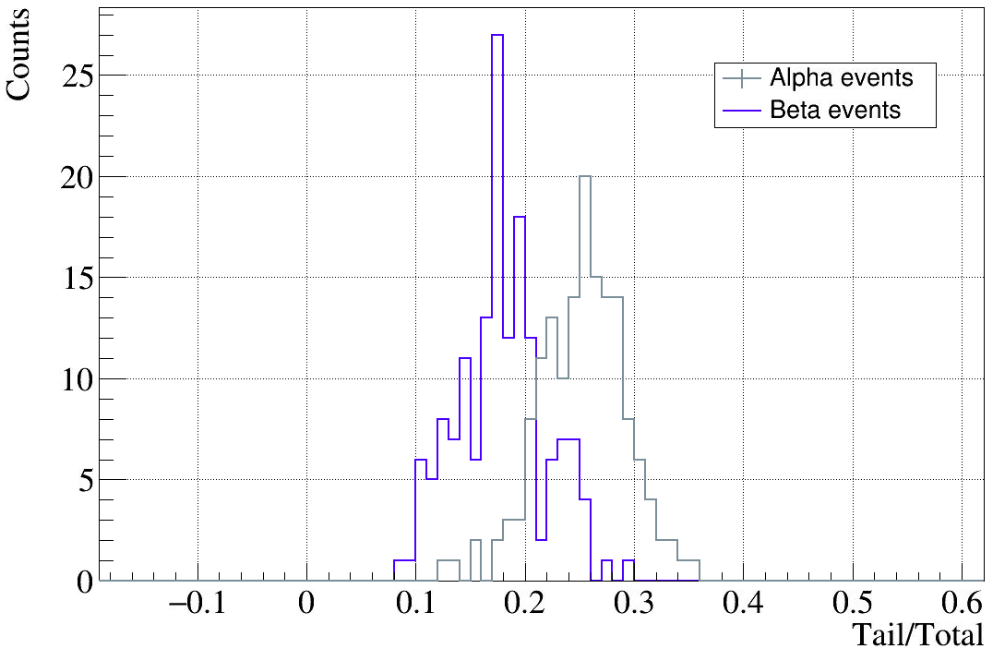

(a)

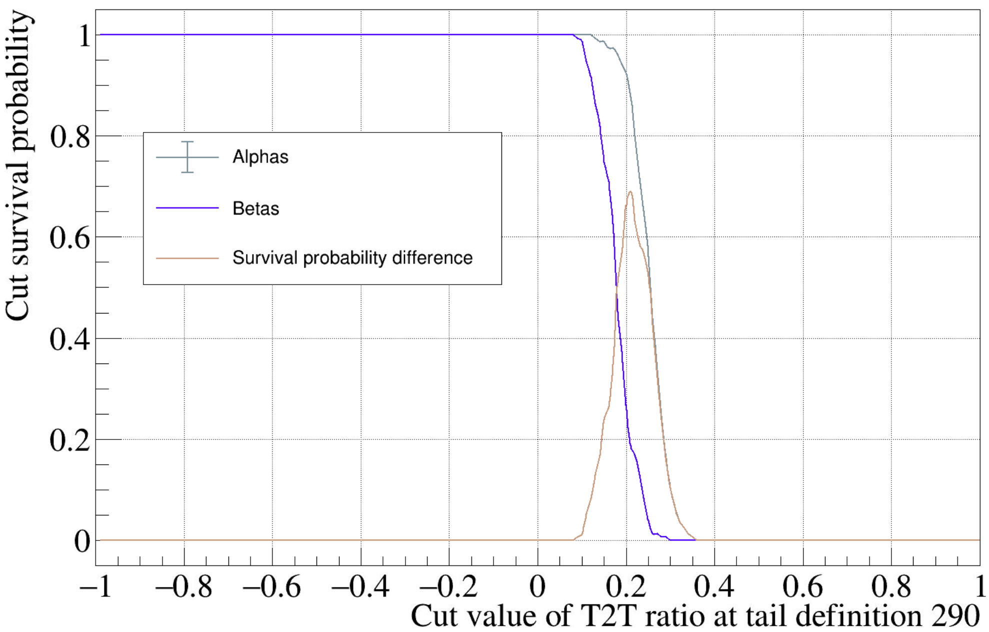

(b)

Figure 6.10 The results of the T2T PSD method for hit time distribution pulse shapes. (a) shows the distributions of the tail/total ratios of α- (grey) and β- (blue) events. The separation is much better than that of the Gatti method. (b) shows the surviving fraction of the two event populations (see description of Fig. 6.7b). The brown line shows the difference of the surviving fractions. It indicates a survival difference of up to $70\,\%$ is possible.

6.3.5 Discussion of the PSD performance

As mentioned above, a PSD performance as good as the one shown in this work might be usable in practical applications. In high-statistics α-particle analyses, where discarding numerous α-events would not significantly impact the results, employing such a PSD parameter may be acceptable since the original number can be reconstructed with the known efficiency. However, the goal is to achieve higher acceptance rates while keeping the number of misidentified events low, as shown, e.g., in [95, 98] with survival rates exceeding $90\,\%$ to $95\,\%$.

While the results are encouraging, there are caveats to them. As described in Sec. 6.3.2, the fiducial volume for the events used in this analysis was as small as possible, $55\,\text{cm}$ out of $150\,\text{cm}$. As explained in Sec. 6.3.2, one of the reasons is that the waveform reconstruction of the RS, which cannot resolve PMT, hits very close to each other. The other reason is the time of flight of the scintillation photons within the detector volume.

A time of flight correction is rectifying the hit time of single photons on the PMT depending on the emission location, namely the vertex of the event. If an event occurs close to one side of the detector, the photons detected by PMTs on the other side are registered with a delay w.r.t. the emission time compared to photons hitting PMTs close to the event vertex. This distorts the light emission profile. OSIRIS is not a huge detector, yet it takes a photon $16.2\,\text{ns}$ to traverse $3\,\text{m}$ because the group velocity of $340\,\text{nm}$ photons is $v_c = 1.86 \times 10^8\,\text{m/s}$ [102]. Since the JUNO LS is a fast scintillator, such delays are detrimental to the PSD performance.

Restricting the fiducial volume minimizes the impact of the photon time of flight in this study. The flight time can still differ by more than $5\,\text{ns}$; further reducing the permissible volume would decrease the number of events even more, leading to too low statistics.

A detector's PSD performance depends on the LS properties and the detector itself, e.g., its resolution, light yield, etc. Dedicated studies have been done on the JUNO LS PSD performance concerning neutron-γ discrimination [75]. In these studies, multiple other LS mixtures were also investigated, and it was found that the best tail definition always lies at the crossing point of the pulse shapes in the falling flank. In the present work, the crossing point lies in the range of $240\,\text{ns}$ to $260\,\text{ns}$ (see Fig. 6.9), which is slightly earlier than the best tail definition, which I found to be at $290\,\text{ns}$. While it is not easily comparable to [75], the difference between the tail definitions might also hint towards improvement potential for the OSIRIS PSD performance.

In conclusion, this work shows that the JUNO LS shows PSD potential for α/β differentiation in the OSIRIS detector, which has also been measured in smaller laboratory experiments [103][2]. I found that the hit time distribution is superior to the cumulative waveform method. Within the scope of this work, the T2T method outperformed the Gatti method. The potential of PSD is a good sign for JUNO, which is planning to use PSD for its physics program [104].

In this work, I have laid the foundations for PSD in OSIRIS. I identified the most promising avenues for the best technique in this detector. However, OSIRIS has room for improvement in the successful implementation of PSD. First, the RS does not apply a time of flight correction to the PMT hit times. The distortion of pulse shapes not happening in the middle of the detector makes PSD impossible. Second, the hit time distribution method requires an improvement of the RS waveform reconstruction since the current version cannot resolve multiple hits on the same PMT, which are close to each other. This also affects PSD performance negatively.

In the future, the flight time correction should be implemented as soon as possible. Also, the OSIRIS group should improve the waveform reconstruction, which might also help with other problems like BiPo-212 coincidence identification. Furthermore, the PSD is energy dependent [101]. In this work, I only investigated the PSD performance at the visible energy of the ^{214}Po decay. The PSD parameters and efficiencies have to be determined anew for other energies.

[2] In the final stage of writing this thesis, it was found that the necessary amount of PPO for JUNO was miscalculated, lowering its amount from $3\,\text{g/L}$ to $2.5\,\text{g/L}$. Laboratory experiments have shown that the PSD performance depends on the PPO concentration and is lower for lower amounts of PPO [75]. The PSD performance might be higher in OSIRIS with the original LS.

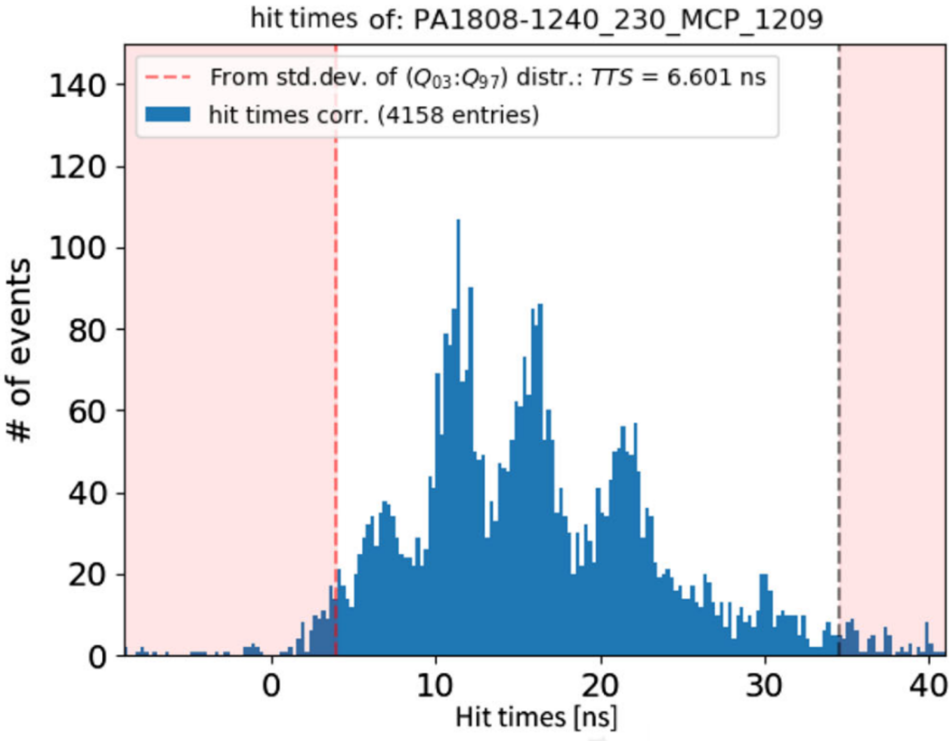

Figure 6.11 Typical relative transit time (TT) distributions for an MCP-PMT (called "hit times"). The TTS is obtained from the standard deviation of the distribution (within the quantiles Q_{03} to Q_{97}. Source: [25].) in case of the NNVT PMTs

However, the largest negative effect on the PSD performance originates from the PMTs. The MCP-PMTs feature a complicated and, especially, broad transit-time spread (TTS). Fig. 6.11 shows the hit time distribution of a typical JUNO multi-channel plate PMT measured during the PMT testing [25]. These PMTs have a TTS value that is several times larger than that of the dynode PMTs used in JUNO [25]. Since PSD relies on the temporal evolution of the light emission process, distortions introduced by the PMTs are detrimental. Under these circumstances, the PSD performance achieved in this work is surprisingly good.

PSD is a useful tool for radiopurity determination by providing an additional criterion events must fulfill. For example, it helps to find α-events that do not have a coincidence structure or where it cannot be reliably found, like the BiPo-212 coincidence in OSIRIS. Since the PSD is restricted to a small fiducial volume, it cannot yet be applied to the radiopurity measurements presented in the next chapter. Therefore, the following investigations of the α-decays of ^{214}Po and ^{210}Po do not include a PSD cut parameter.

Chapter 7

JUNO Scintillator Radiopurity Measurements

The determination of the JUNO LS radiopurity is OSIRIS's main task. I have shown in chapter 6 that the BiPo coincidence of the ^{238}U chain can be tagged reliably with the OSIRIS system. In the following, I will present the first results on the LS radioactivity measurements of the OSIRIS detector. Sec. 7.1 contains the determination of the BiPo rate of the data-taking period between 1 June and 26 July and the derived ^{238}U contamination. In Sec. 7.2, the single events with no temporal coincidence are investigated to determine the contamination of ^{210}Po in the LS. In the end, Sec. 7.3 details the search for additional α-lines in the energy spectrum.

7.1 First results for the ^{238}U contamination using BiPo coincidences

7.1.1 Calculating the BiPo rate

With the RS-processed data set described in Sec. 6.2 the determination of the BiPo rate in the detector is possible. BiPo events are essentially defined as two events with a time difference between $5\,\mu s$ to $1640\,\mu s$. Additionally, the prompt β-event has to have energies between 0.2 MeV to 2 MeV and the delayed α-event energies between 0.4 MeV to 0.7 MeV.[1] For the following analysis, I shrink the allowed time difference between coincident events:
The time difference of the coincident events is maximal $820\,\mu s$ while the lower limit of $5\,\mu s$ stays the same. $820\,\mu s$ corresponds to 5 half-lifes of ^{214}Po. Higher values contribute almost no events but increase the background.

Fig. 7.1 shows the resulting energy spectra (after cuts) of α- (grey) and β- (blue) events. The brown lines correspond to the energy cut values of the β-spectrum, and the black ones to the cuts on the α-energies.

The visible energy of the delayed α-event can be seen in Fig. 7.2. I fit the alpha energy peak with a sum of a Gaussian function and a constant to retrieve the mean energy μ and its standard deviation σ. The fit function is, therefore, defined as

$$f(x) = C + N \cdot \exp(-0.5 \cdot ((x - \mu)/\sigma)^2),$$

where C, N, μ, and σ are the free fit parameters. The best fit values are $C = 46.50 \pm 2.90$, $N = 1770.00 \pm 6.75$, $\mu = (0.544\,40 \pm 0.000\,17)$ MeV, and $\sigma = (0.052\,20 \pm 0.000\,23)$ MeV with a goodness-of-fit $\chi^2/\mathrm{NDF} = 1.34$. Hence the cut values at 0.4 and 0.7 MeV, respectively, correspond to the valid energy interval $[\mu - 2.77 \pm 0.02\sigma, \mu - 2.98 \pm 0.02\sigma]$. This cut allows $(99.58 \pm 0.04)\,\%$ of the α-peak.
The non-zero constant C of this fit suggests a background not addressed by the cuts with a uniform energy distribution. To estimate the impact of these events on the BiPo rate calculation, I calculate the contribution $f_{\text{constant background}} = f_{\text{CB}}$ of this background to the total spectrum:

$$f_{CB} = \frac{\text{number of background events}}{\text{total number of events}} = \frac{N_{\text{bins}} \cdot C}{N_{\text{total}}} = \frac{\frac{0.7-0.4\,\text{MeV}}{0.002\,\text{MeV}} \cdot (46.50 \pm 2.90)}{122\,403} = (5.70 \pm 0.36)\,\%$$

[1] See Sec. 6.2 for all cuts.

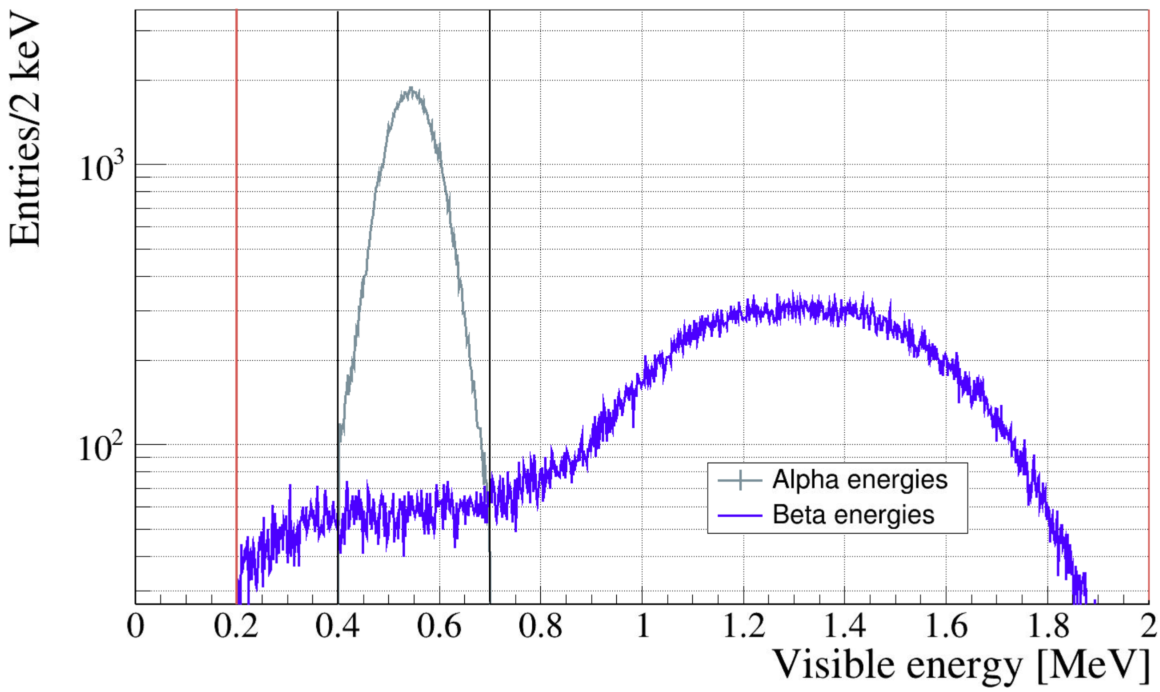

Figure 7.1 The visible energy spectra of the α- and β decays of the BiPo-214 coincidence signal that survived all cuts. The ^{214}Bi -decay energies are shown in blue, and their cut values are the brown vertical lines. The ^{214}Po -energy spectrum is shown in grey, and its cut values are the black vertical lines.

When taking the data, the OSIRIS group could not start and stop each *run* - a continuous recording of the data without breaks - at the same time of day. Generally, runs recorded overnight are roughly twice as long as the daytime runs because the onsite crew handles the data-taking starts and stops. Additionally, some runs are fragmented or cut short due to technical difficulties. Other runs are shorter on purpose to have dedicated small files, i.e., shortly after AV circulations.

I split the data according to detector runs in this analysis and determined the BiPo rate of each run. Fig. 7.3 shows the temporal evolution of the BiPo rate between 1 June and 26 July. The above-described structure of runs leads to some data points having very few events and, hence, large uncertainties. Normally, the rate of each run is the number of BiPo events divided by the length of the run. However, I statistically subtract the constant background contribution f_{CB} defined above from each data point of each run to estimate its impact.

The uncertainty in the x-coordinate is the length of the run. The uncertainty in the y-direction is the sum of the statistical and systematic uncertainty. The statistical uncertainty is $\sqrt{N}$, where N is the number of BiPo events in the run. The systematic uncertainty is the uncertainty of f_{CB}.

The vertical dashed lines show AV circulations or LS exchange times as listed in Table 6.1. It is immediately obvious that highly increased BiPo rates follow these detector operations.

7.1.2 Conversion of the BiPo rate to a ^{238}U contamination

We can now use Eq. 6.1 to convert the BiPo rate to uranium contamination under the assumption of secular equilibrium. The y-axis on the right side of Fig. 7.3 shows the corresponding ^{238}U -contamination of the LS. The calculation of the efficiency ϵ is the product of all the efficiencies below and involves the following considerations:

1. The time difference cut vetoes BiPo coincidences with a smaller or larger separation than the lower or higher cut limit, respectively. This reduces the efficiency of BiPo detection. Under the assumption that the detection probability is not a function of the time difference, this efficiency

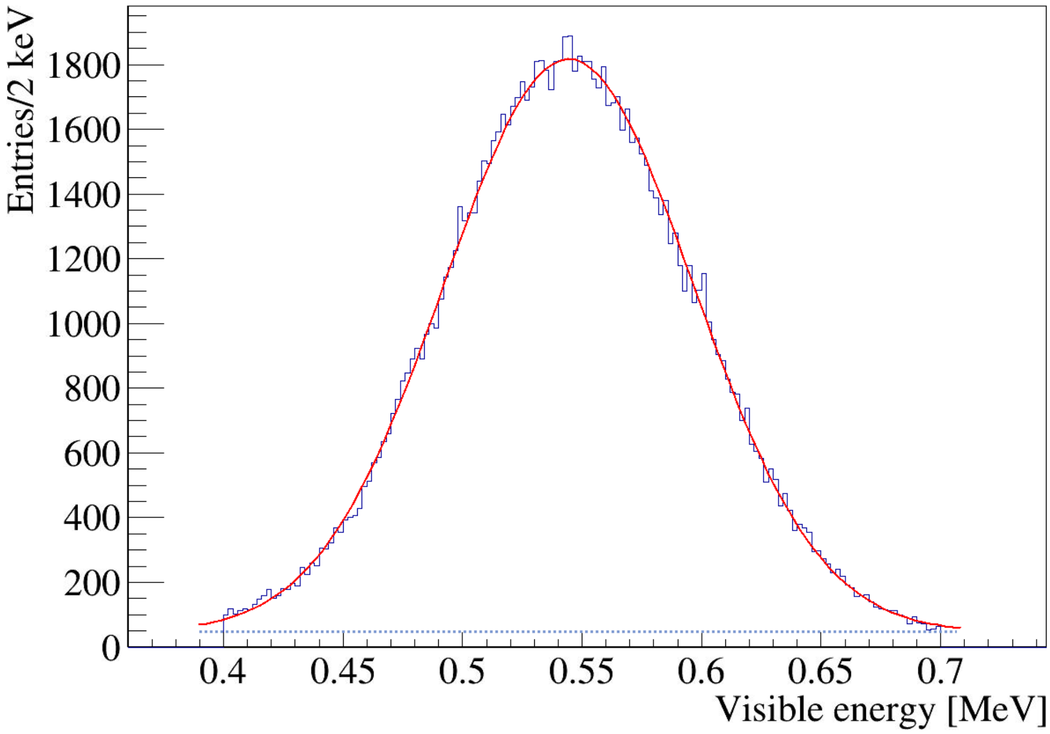

Figure 7.2 The α-energy spectrum shown in Fig. 7.1 together with the fit to the data $f(x) = C + N \cdot \exp(-0.5 \cdot ((x - \mu)/\sigma)^2)$ (shown as the red line). C, N, μ, and σ are the free parameters of the fit. The best-fit values are $C = 46.50 \pm 2.90$, $N = 1770.00 \pm 6.75$, $\mu = (0.544\,40 \pm 0.000\,17)$ MeV, and $\sigma = (0.052\,20 \pm 0.000\,23)$ MeV with a goodness-of-fit $\chi^2/\mathrm{NDF} = 1.34$. The constant C is indicated as the blue dashed line. Its presence suggests background signals not removed by the cuts.

$\epsilon_{\Delta T}$ can be calculated as the probability that the decay happens in the window demarcated by the cut values:

$$\epsilon_{\Delta T} = \frac{\int_{t_1}^{t_2} e^{-t/\tau} dt}{\int_0^\infty e^{-t/\tau} dt} = e^{-t_1/\tau} - e^{-t_2/\tau} = 0.948. \tag{7.1}$$

$t_1 = 5\,\mu\text{s}$ is the lower time difference cut limit and $t_2 = 820\,\mu\text{s}$ is the higher time difference cut limit. $\tau = 236\,\mu\text{s}$ is the ^{214}Po -lifetime.

2. The fiducial volume cut restricts the fraction of the scintillator in which BiPo events are registered. Assuming that the BiPo identification doesn't depend on the event position, its efficiency ϵ_{fV} is

$$\epsilon_{fV} = \frac{V_{fV}}{V_{tot}} = \left(\frac{145}{150}\right)^3 = 0.903. \tag{7.2}$$

3. As described in Sec. 7.1, the α-energy cut has an efficiency $\epsilon_{alpha,E} = (99.58 \pm 0.04)\,\%$.

4. The efficiency of the β-energy cut is hard to precisely estimate without a Monte Carlo simulation. I obtain a conservative estimate assuming the β-energy spectrum is flat from $E = 0$ keV to the energy cut value 200 keV. This almost certainly overestimates the events with β-energies below 200 keV but can act as a lower limit on the efficiency. Setting the number of events to 40 per 2 keV bin implies that 4000 events have been cut. This results in an efficiency of the β-energy determination of $\epsilon_{beta,E} = (96.83 \pm 0.32)\,\%$.

5. Another reduction of the BiPo tagging efficiency comes from the RS tagging algorithm. It checks if two consecutive events fulfill the BiPo conditions. However, it is possible that in between the ^{214}Bi and the ^{214}Po decay, another event happens. If this event doesn't fulfill the α-event conditions,

the BiPo event is not tagged.[2] This can be seen as a detector dead time for BiPos. The average RS event rate λ is roughly 4 Hz. We can use Poisson statistics to calculate the probability of two or more events happening within $\Delta T = 820$ µs (the time difference cut limit) of each other:

$$P(\text{at least one event within }\Delta\text{T}) = 1 - P(0\,\text{events within }\Delta\text{T}) = 1 - e^{-\lambda\cdot\Delta T} = 0.65\%.$$

Therefore, we get the corresponding efficiency $\epsilon_{deadtime} = 99.35\,\%$.

The total efficiency is $82.0\,\%$.

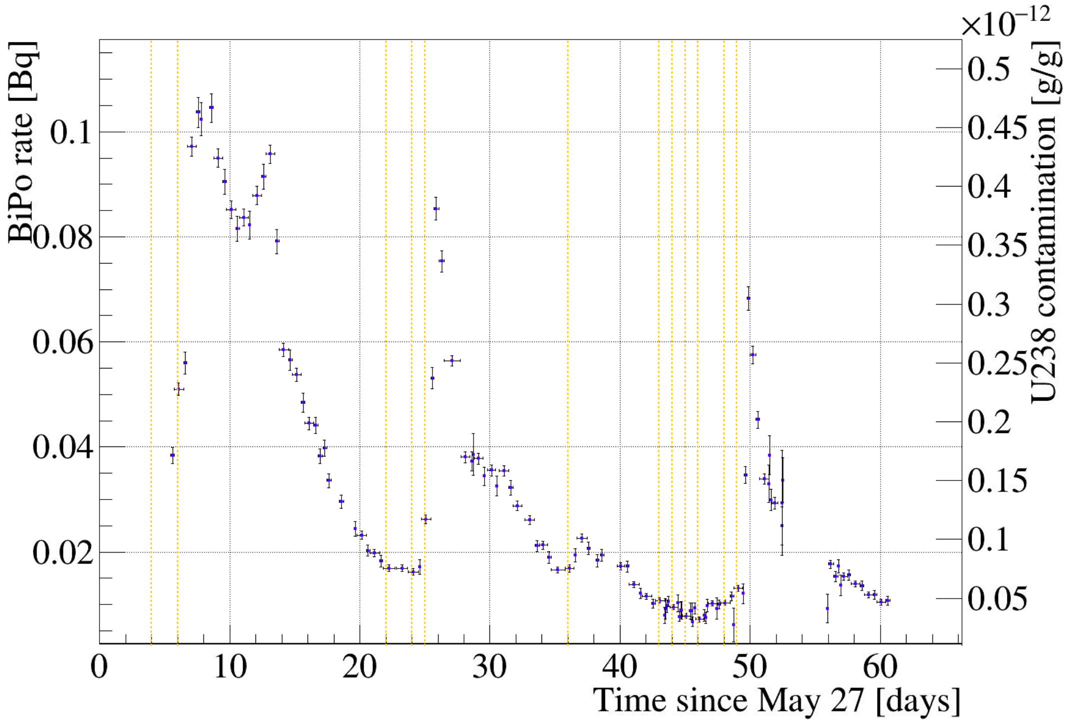

Figure 7.3 The BiPo event rate as a function of time. The data points start on 1 June and end on 26 July. The orange vertical lines indicate the detector circulation operations listed in Table 6.1. After the circulations, the BiPo rate increases rapidly. At the time of writing, it was not clear why some of the detector operations seemingly didn't introduce much or any ^{222}Rn .
The right y-axis shows the corresponding ^{238}U contamination in the LS under the assumption of secular equilibrium between ^{214}Bi and ^{238}U , i.e., only in the flat segments of the rate.

We can now use the BiPo rate evolution to test the hypothesis that the increase in rate after AV circulations is due to newly introduced ^{222}Rn contamination. The slopes of the BiPo rate should follow the exponential decay law $R(t) = Ne^{-t/\tau}$, where N is the normalization constant and τ is the decay time. Fitting this function to the rate, τ should be $\tau_{Rn222} = 5.51$ days [105]. Fig. 7.4a shows this fit to the BiPo rate between day 15.5 and 21.6. The red curve shows the fit function with its $95\,\%$ confidence interval as the red error bars. The best-fit value is $\tau = (5.78 \pm 0.32)$ days, which agrees perfectly with the literature value. However the goodness-of-fit is surprisingly small: $\chi^2/\text{NDF} = 0.636$.

This can be understood by the following considerations:

1. We assume that the data only contains decays from ^{222}Rn introduced with the AV circulation. This neglects other external, continuous sources of contamination and ^{222}Rn from the ^{238}U decay chain.

[2] The in-between event can also fulfill the conditions of the ^{214}Po -decay. This would switch the real α-decay for the accidental background event, but the coincidence would be counted as a BiPo event. Only if another cut removes the false α-event after the RS would the BiPo event be incorrectly discarded. Such events might influence the time difference distribution (see Fig. 6.3) by skewing it to a smaller temporal separation. Considering the probability of any event happening between the BiPo signature calculated here, this effect seems highly unlikely and can be safely neglected.

2. To suppress these other sources, we have to choose a data interval in which the ^{222}Rn from the AV circulation is dominating. This leads to limited data periods in which the fit has too many free parameters, as evidenced by the χ^2/NDF being much smaller than 1.

3. The fit is very sensitive to its range because of the external factors that an exponential law alone does not take into account. Therefore, it is prone to cherry-picking. Fig. 7.4b shows the fit for the range between day 15.5 and 23.5 resulting in $\tau = (5.87 \pm 0.17)$ days and $\chi^2/\mathrm{NDF} = 1.69$.

Nonetheless, the fit lends credence to the hypothesis that the dominating source of BiPo events shortly after the AV circulation operations is ^{222}Rn. The AV circulations always precede the sharp rise of the BiPo rate and subsequent decline with a decay time in the range of ^{222}Rn.

In Fig. 7.4b, the BiPo rate seems to level out. We note this behavior at several points in the BiPo rate (Fig. 7.3), e.g., around days 22, 44, and 60. This is incompatible with the AV circulations being the only source of ^{222}Rn and, therefore, BiPos. The BiPo rate leveling out is expected if there is a constant regeneration of ^{222}Rn due to either an external source, e.g., a leak, or the internal concentration of ^{238}U in the LS.

Thus, assuming a singular introduction of ^{222}Rn by the AV circulation and a constant due to ^{238}U , we can estimate the ^{238}U concentration in the LS.

$$f(t) = Ne^{-t/\tau_{Rn222}} + C. \tag{7.3}$$

Only N and C are free parameters in this fit. Fig. 7.5 shows the fits to the first falling flank of the rate around day 20 (Fig. 7.5a) and the last days (Fig. 7.5b). The red line and error bars are the fit and its $95\,\%$ confidence band, respectively. The dashed orange line indicates the value of the constant C. Fig. 7.5a returns a best-fit-value for $C = (0.0025 \pm 0.0009)$ Bq which converts to a ^{238}U concentration of $(1.11 \pm 0.39) \times 10^{-14}\,\mathrm{g/g}$. The goodness-of-fit is $\chi^2/\mathrm{NDF} = 1.49$. Fig. 7.5b has the best-fit-value $C = (0.0050 \pm 0.0010)$ Bq which is equivalent to a ^{238}U contamination of $(2.23 \pm 0.45) \times 10^{-14}\,\mathrm{g/g}$. The goodness-of-fit is $\chi^2/\mathrm{NDF} = 1.48$.

As above, this fit has to be taken with a grain of salt. Choosing the fit range differently significantly impacts the results. Unfortunately, none of the periods are long enough for the BiPo rate to level out for a long time without disturbance. The last data points of Fig. 7.5b, in particular, only hint at settling on a constant value. Due to technical reasons, the data wasn't accessible for the five days after 26 July.

The periods between days 25 and 50 are not investigated due to the many detector operations in this time period, which makes the fitting more unreliable.

7.1.3 Discussion of the measured BiPo rates

The ^{238}U concentrations calculated from the fits in Fig. 7.5 are only estimates due to the complications described above. However, the fitting of different time intervals with decaying BiPo rates recovers the ^{238}U concentrations of the same order of magnitude of $O(1 \times 10^{-14}\,\mathrm{g/g})$. Even just reading off the values of the flat periods in Fig. 7.3 gives us a similar estimate of several $10^{-14}\,\mathrm{g/g}$ of ^{238}U in the LS. Importantly, these values provide an upper limit on the internal ^{238}U /^{226}Ra contamination.

As discussed in Sec. 3.6, JUNO requires ^{238}U concentrations of $10^{-15}\,\mathrm{g/g}$ or better for determining the neutrino mass ordering. For solar neutrino physics, the radiopurity should be even better by one to two orders of magnitude. Barring significant uncertainties in this work, the measured BiPo rates are much higher than required for the experiment. The factors influencing the contamination calculation that have been neglected in this work will not change the result significantly. Additionally, multiple independent analyses show similar BiPo rates to those presented here.

The most important improvement to this analysis could be the investigation of simulated BiPo events and background. To improve the precision of such analysis, the Monte Carlo simulation will be performed in the near future. This should enable some of the following improvements:

- The precise calculation of the DAQ chain efficiency at general tagging any and, particularly, BiPo events. The simulation would allow us to study the data processed by the RS event-by-event.

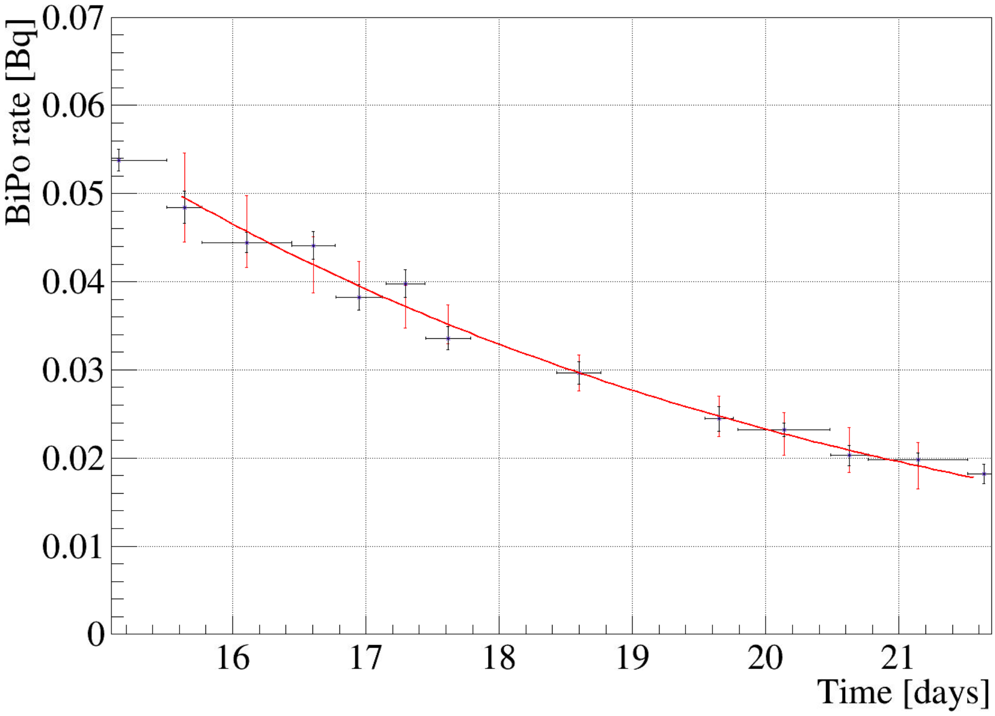

(a) A fit to the first falling flank of the BiPo rate. The best fit values are $\tau = (5.78 \pm 0.32)$ days and $N = (0.74 \pm 0.13)$ Bq. The goodness-of-fit is $\chi^2/\mathrm{NDF} = 0.636$.

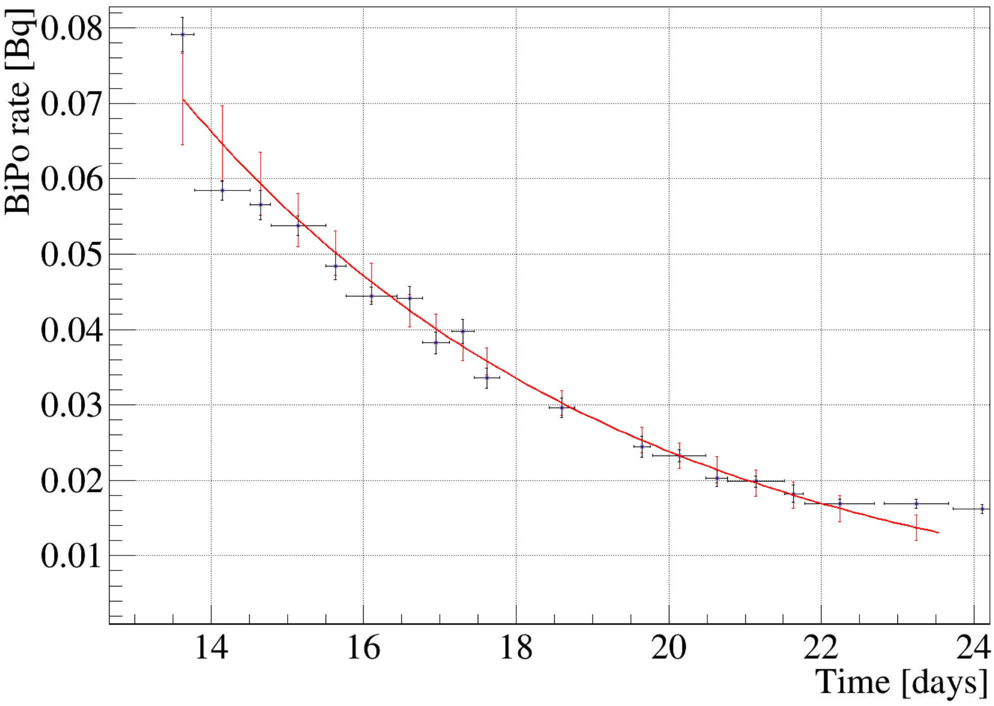

(b) The fit to the region of a slightly enlarged fitting range compared to (a). The best fit values are $\tau = (5.87 \pm 0.17)$ days and $N = (0.720 \pm 0.062)$ Bq. The goodness-of-fit is $\chi^2/\mathrm{NDF} = 1.69$.

Figure 7.4 These figures show two segments of BiPo rate evolution (Fig. 7.3) fitted with the function $f(t) = Ne^{-t/\tau}$, where τ and C are free parameters. The red lines show the best fit to the data points (with black uncertainties). The red error bars show the $95\,\%$ confidence level of the fit. The difference between (a) and (b) shows that the fit results are sensitive to the fit range. The resulting decay time agrees closely with the radon decay confirming that the sharp rise of measured BiPo events in the LS after AV circulations is due to the introduction of external ^{222}Rn .

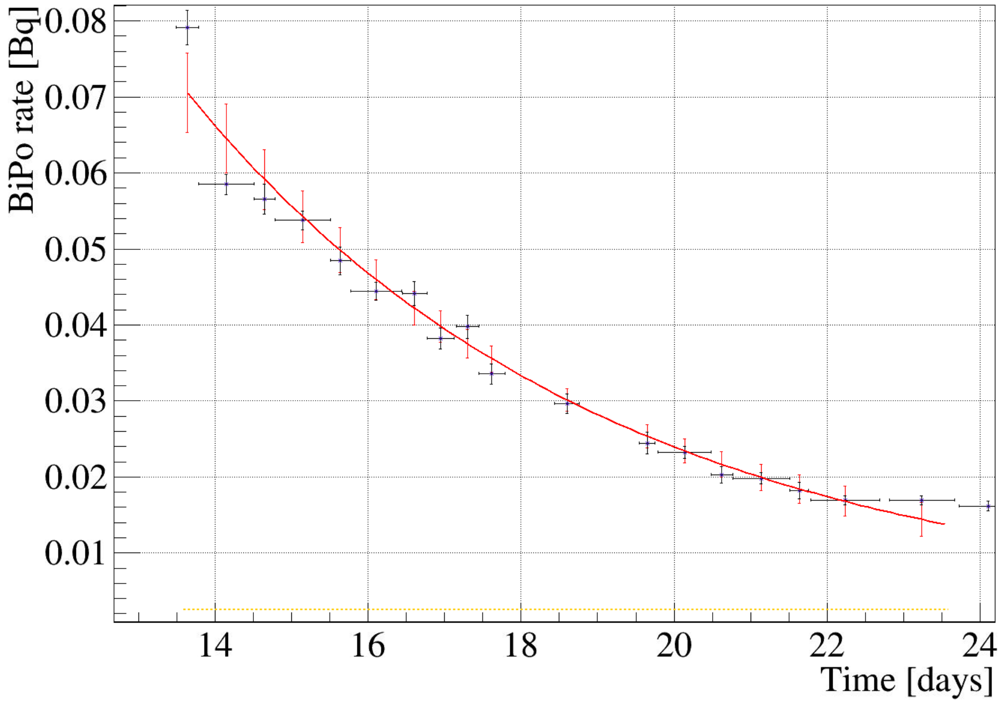

(a) The fit to the first falling flank of the BiPo rate over time. The best fit values are $C = 0.0025 \pm 0.0009 \equiv (1.11 \pm 0.39) \times 10^{-14}$ g/g and $N = (0.810 \pm 0.026)$ Bq. The goodness-of-fit is $\chi^2/\mathrm{NDF} = 1.49$.

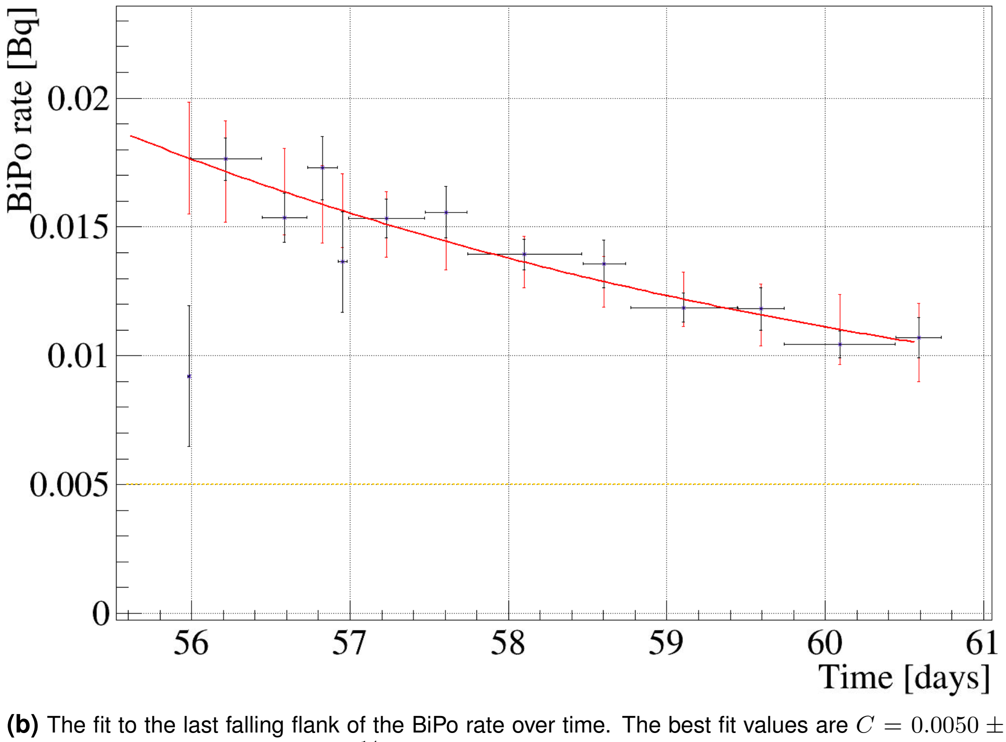

(b) The fit to the last falling flank of the BiPo rate over time. The best fit values are $C = 0.0050 \pm 0.0010 \equiv (2.240 \pm 0.459) \times 10^{-14}$ g/g and $N = (323.76 \pm 36.41)$ Bq. The goodness-of-fit is $\chi^2/\mathrm{NDF} = 1.48$.

Figure 7.5 These figures show two segments of BiPo rate evolution (Fig. 7.3) fitted with the function $f(t) = Ne^{-t/\tau_{Rn222}} + C$, where N and C are free parameters and $\tau_{Rn222} = 5.51$ days is fixed. The red lines show the best fit to the data points (uncertainties in black). The red error bars show the 95 % confidence level of the fit. The orange dashed line shows the best fit of the constant C and can be converted to an equivalent uranium contamination under the assumption of secular equilibrium. The time periods - especially when the rate becomes nearly constant - are very short due to the following detector operations. Longer periods would be beneficial for the determination of the constant C.

- Studying the effects of cuts on the data and background events. I.e., a cut on the spatial separation of the coincident events is often employed in large-scale LS experiments. The separation between the β- and subsequent α-decay is negligible (order of millimeters or less). However, multiple γ's usually accompany the β-decay. These can traverse tens of centimeters before having deposited their entire energy. Therefore, they cause a smearing out of the reconstructed vertex. The robust vertex reconstruction with the RS requires input from the Monte Carlo simulations.
- It might be beneficial to bin the data differently for the rate evolution. The data was binned according to the detector runs in the present work. This leads to some bins having very few events since the corresponding runs were short. Other methods, like bins of the same length in time or the same number of events, might have advantages.
- A longer undisturbed period of running the detector. Such a time period might facilitate better and more reliable fitting results.
- Improving the PSD can help to suppress backgrounds by ensuring that the prompt and delayed event of the coincidence is a β- and α-event, respectively.

The two main potential reasons for this high BiPo rate are

1. the intrinsic contamination of the JUNO LS that OSIRIS measured or
2. an external continuous contamination of the LS in OSIRIS.

It would be troublesome news for the JUNO experiment if the former were true. This means that the purification systems are insufficient to produce clean enough LS. Since the filling of JUNO is scheduled to start around the beginning of 2025, major system changes would presumably delay the experiment significantly. Luckily, this scenario seems unlikely at the time of writing. Independent measurements via neutron activation analysis indicate that the LS is cleaner than measured in OSIRIS.

This leaves OSIRIS as the source of the contamination. While the BiPo rate may be due to ^{238}U introduced into the LS by OSIRIS, it is more likely that external ^{222}Rn enters the LS. One potential entry point is the LHS, where tiny air leaks can introduce detrimental amounts of not only ^{222}Rn but also other isotopes, i.e., ^{85}Kr . Such a scenario can theoretically be tested by discovering an increase in ^{85}Kr in addition to ^{222}Rn . However, even tiny air leaks would likely produce much greater concentrations of ^{222}Rn than in the data.

Another possibility is the emanation of Radon from the surfaces in contact with the LS. In this case, the data would not show an increase in Krypton. The surfaces could be the whole piping system, instrumentation inside the AV like thermometers, or even the AV itself. This possibility is currently under investigation by analyzing the spatial distribution of BiPos and other events.

Yet another reason might be the WT of OSIRIS, which engulfs the AV. Unfortunately, it is not completely water-tight and loses roughly $200\,\mathrm{L/day}$. This loss has to be compensated by constantly filling in new water. The radon concentration in the water is likely higher due to emanation from the piping, equivalent to the discussion above on newly filled LS. The loss and refilling of water create convection in the WT, which might distribute the incoming radon efficiently in the volume. From there, it might emanate through the AV into the LS. In this scenario, the BiPo rate should be higher at the edges of the AV.

Lastly, the radon might originate from the nitrogen blanket on top of the LS in the detector. Increased radon concentrations could travel from the nitrogen into the LS at the touching surface. At the time of writing, this seems to be one of the most likely explanations. Also, in this case, a spatial correlation of BiPo events would be observed with more events at the top of the AV. A radon detector monitoring the nitrogen supply will shine a light on this hypothesis [106].

Based on these early results, studies with a longer data set were performed. Using a strict fiducial volume cut removes events at the edges of the detector where external contamination is most likely to occur. Thereby, the upper limit on the ^{238}U concentration was determined to be roughly

1×10^{-15} g/g [107]. Additionally, neutron activation analysis measurements of the LS after the last purification plant returned a contamination of $< 0.8 \times 10^{-15}$ g/g [108]. These values - should they be achieved after filling the JUNO CD - would be within the design goal. For comparison, Table 7.1 shows the radiopurity w.r.t ^{238}U of four other LS experiments upon filling the detectors. JUNO performs very well compared to many other experiments, except for the famously pristine Borexino/CTF LS.

Experiment	**^{238}U Concentration [1×10^{-15} g/g]**
This work	11 ± 4
Neutron activation analysis of the JUNO LS	$\sim$0.8
CTF [109]	<0.01
Borexino [110]	<0.02
Double Chooz[111]	10.9 ± 0.3
Daya Bay [106]	7.52 ± 1.78

Table 7.1 The ^{238}U concentrations in the respective LS of several experiments.

7.2 First measurements of the ^{210}Po contamination

7.2.1 Determination of the ^{210}Po rate

The introduction of external ^{222}Rn does not only increase the background levels in the short term. Fig. 6.1 shows that there are isotopes of the ^{238}U chain after ^{214}Po which are long-lived relative to the timeframe of detector operation: ^{210}Pb with $\tau_{210\mathrm{Pb}} = 32.2$ years and - to some extent - ^{210}Po with $\tau_{210\mathrm{Po}} = 199.7$ days. ^{210}Pb has an endpoint energy of only 63.5 keV, which is too low to interfere with most analyses. However, the following β-decay of ^{210}Bi has a Q-value $Q_{210\mathrm{Bi}} = 1161.5$ keV and ^{210}Po is an α-decay with $E_{210\mathrm{Po}} = 5407.5$ keV [112, 113].

Moreover, and most importantly, all α-particles can undergo α-n reactions on carbon, e.g., $^{13}\mathrm{C}(\alpha, n)^{16}\mathrm{O}$. These reactions mimic IBD events where the α-particle is the prompt and the resulting neutron the delayed signal. Hence, they are a dangerous background for JUNO's most important goal, the NMO determination. The suppression and knowledge of this background are very important for JUNO. These are backgrounds that we must understand and avoid as much as possible. The mother isotope ^{210}Pb isotopes will not decay for the whole runtime of the JUNO detector. As an example, for Borexino, the ^{210}Bi background was the main obstacle in their discovery of CNO-cycle neutrinos [76]. In the KamLAND experiment, the ^{210}Po background was challenging because the initial ^{210}Po decay was below the detection threshold [114].

We can measure the ^{210}Po concentration in the LS if we can identify the corresponding peak in the single event spectrum. I obtained the single events in the RS as described in 6.2. They are events that have no other event in the following 2 ms, and they cannot be part of a BiPo coincidence.

Fig. 7.6 shows examples of the energy spectrum of two runs. The peak centered around 70 keV results from the detector threshold, and its right flank comprises mainly ^{14}C decays. The next peak at roughly 300 keV is the peak of interest, containing the ^{210}Po alpha peak. In contrast to Fig. 7.6a, Fig. 7.6b contains another peak-like structure at 500 keV. Sec. 7.3 contains the analysis of this peak.

The singles spectrum has many components since it consists of all the events registered outside BiPo coincidences. It includes all signals of long-lived decay chains and other decays, i.e., ^{14}C , ^{85}Kr , etc. Understanding the spectrum fully is not the goal of this work.

I retrieve the number of α-events in the peak by fitting the peak with a Gaussian function plus an exponential function approximating the background:

$$f(E) = N \exp\left(-0.5 \cdot \left(\frac{E - \mu}{\sigma}\right)^2\right) + Ce^{\lambda E}. \tag{7.4}$$

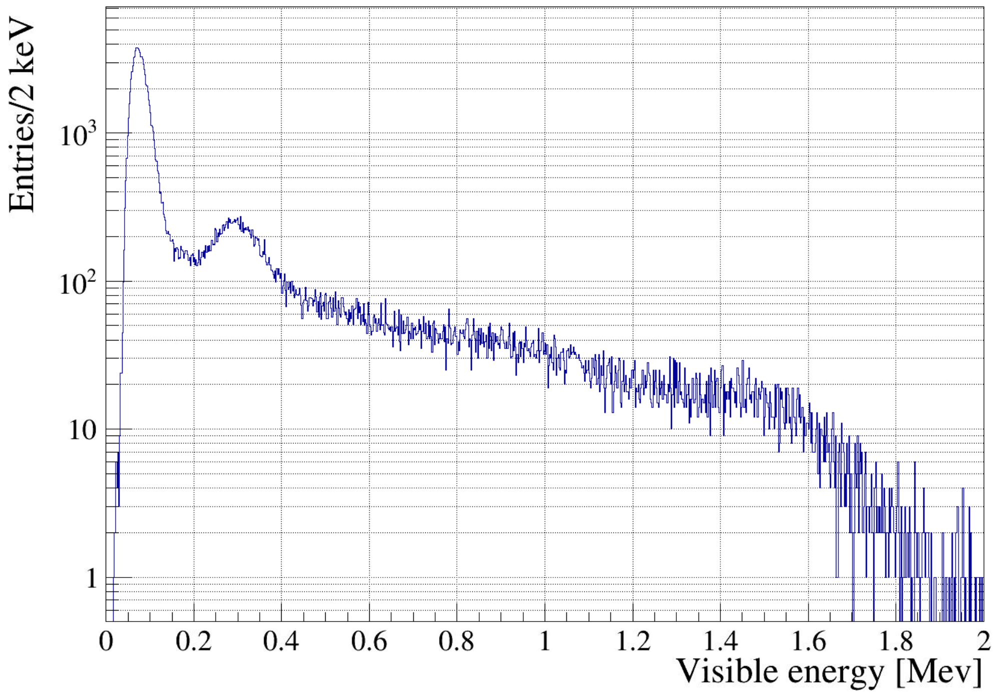

(a) The singles spectrum of a run (Run 24) much later than an AV circulation. Short-lived isotopes introduced during an AV circulation have decayed already and don't distort the spectrum.

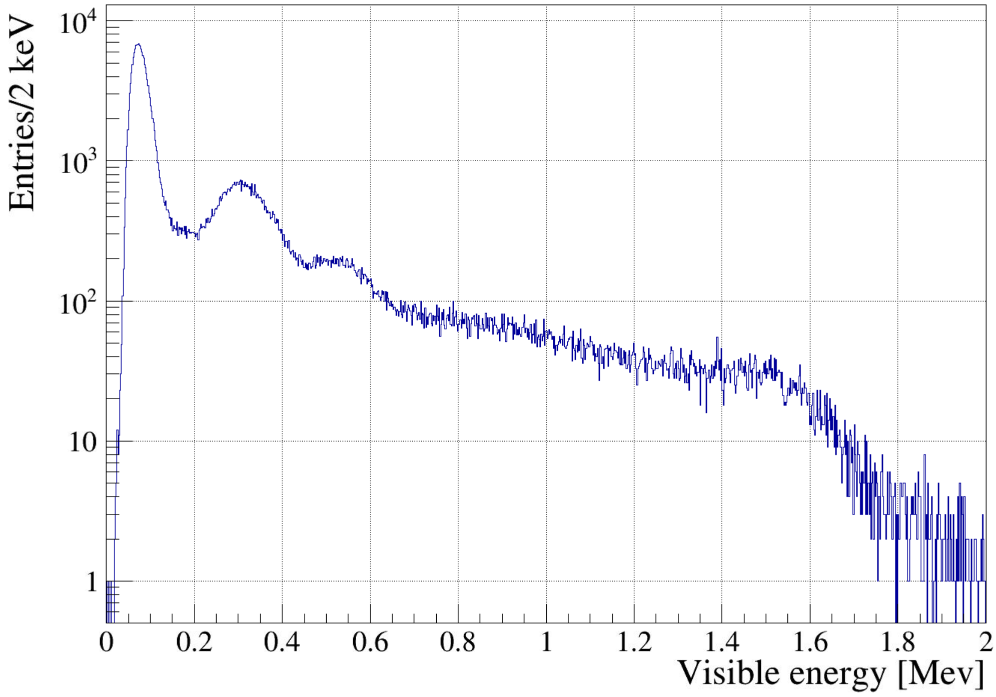

(b) The singles spectrum of a run (Run 9) shortly after an AV circulation. It contains an additional peak-like structure at 500 keV.

Figure 7.6 Two examples of the singles energy spectrum. Both exhibit the detector threshold with the ^{14}C decay flank centered around 70 keV and the peak containing ^{210}Po around 300 keV.

N, μ, σ, λ, and C are the free parameters of the fit. Fig. 7.7 shows two examples of fits. Fig. 7.7b is an example of a bad fit due to a too-small number of events in the run. This leads to large uncertainties of these data points of the singles and ^{210}Po rate evolution plots.

I calculate the rate of α-events in each run by dividing the number of α-events by the length of the run. Fig 7.8 shows the resulting time evolution of this rate. As before, the orange dashed lines indicate the dates of AV circulation operations. We observe increased rates after these, which subsequently fall off.

However, this α-peak is, in reality, comprised of several α-lines which cannot be resolved separately. Table 7.2 lists the daughter isotopes with the highest branching ratios of ^{238}U and their energies. We see that ^{222}Rn and ^{218}Po are α-emitters which have similar energies as ^{210}Po . Therefore, the events caused by these decays will contribute to the 300 keV peak. Fortunately, we note that ^{222}Rn has a much longer lifetime than all following decays until ^{210}Po, including the BiPo coincidence. We can, therefore, assume secular equilibrium between ^{222}Rn, ^{218}Po, and ^{214}Po . We arrive at

$$R_{222Rn} = R_{218Po} = R_{214Po} \tag{7.5}$$

$$\implies R_{210Po} = R_\alpha - R_{222Rn} - R_{218Po} = R_\alpha - 2 \cdot R_{214Po}, \tag{7.6}$$

where R_i are the rates of the respective isotope of one run, and R_α the rate of α-events in the 300 keV peak. With this, we arrive at Fig. 7.9 for the rate evolution of ^{214}Po decays.

Isotope	**Life time τ**	**Energy [keV]**	**Decay mode**
^{238}U	6.45×10^9 years	4200	α
^{234}Th	34.8 days	199	β^-
^{234m}Pa	1.7 min	2290	β^-
^{234}U	3.53×10^5 years	4770	α
^{230}Th	1.15×10^5 years	4690	α
^{226}Ra	2.3×10^3 years	4790	α
^{222}Rn	5.51 days	5490	α
^{218}Po	4.4 min	6000	α
^{214}Pb	38.7 min	1020	$\beta^-\gamma$
^{214}Bi	28.4 min	3270	$\beta^-\gamma$
^{214}Po	236 ms	7690	α
^{210}Pb	32.2 years	63	$\beta^-\gamma$
^{210}Bi	7.23 days	1160	β^-
^{210}Po	200 days	5410	α
^{206}Pb	stable	-	-

Table 7.2 The isotopes with the highest branching ratios of the ^{238}U chain with their respective lifetimes, maximum released energy, and decay mode. Alternative decay branches and the γ-lines accompanying many decays are not listed.

7.2.2 Discussion of the ^{210}Po results

The shape of the ^{210}Po rate is consistent with the expectation. The rate rises shortly after introducing the LS previously stored in the head or buffer tank. While the same in shape as the BiPo rate (Fig. 7.3), at first glance, the ^{210}Po rate reacts faster to the AV circulation between days 40 and 50. However, many runs in this period were short, providing dedicated data sets right after AV circulations. Since the ^{210}Po rate is determined by the fit to the data - instead of event counting as in the case of the BiPo rate - fewer events affect the uncertainty much more, as evidenced by the error bars. Nonetheless, these results provide an upper limit on the ^{210}Po concentration in the LS.

The following are the possible improvements of this analysis:

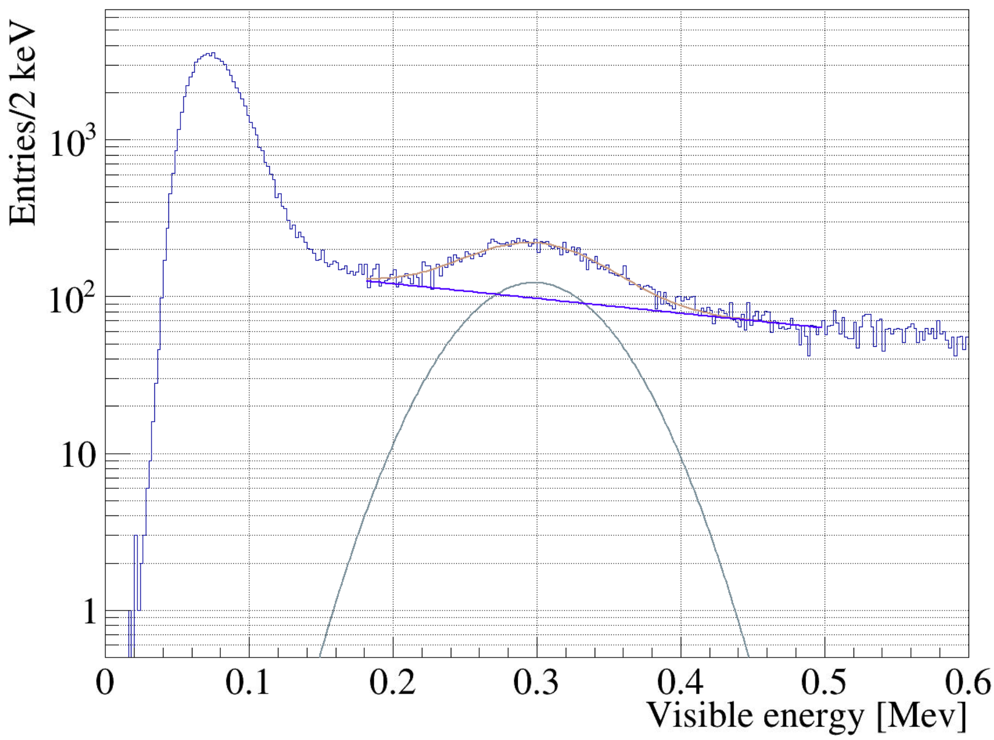

(a) An example for the fit of most data sets (runs). The best-fit values are $N = 122.91 \pm 3.16$, $\mu = (0.290 \pm 0.001)$ keV , $\sigma = (0.045 \pm 0.002)$ keV, $\lambda = (-2.16 \pm 0.13)$ keV^{-1} , $C = 186.09 \pm 10.57$. The goodness-of-fit is $\chi^2/\mathrm{NDF} = 1.09$.

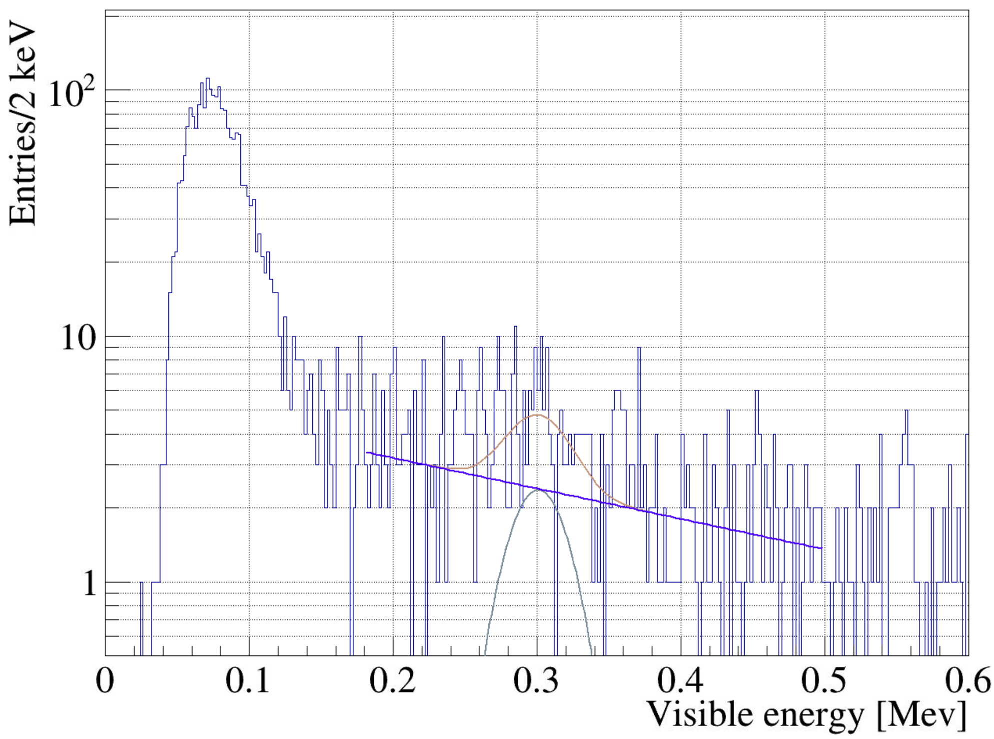

(b) An example for the fit of some data sets (here: Run 93) containing only a few events. In such cases, the result is not reliable and has large uncertainties. The best-fit values are $N = 2.39 \pm 0.80$, $\mu = (0.30 \pm 0.01)$ keV, $\sigma = (0.02 \pm 0.01)$ keV, $\lambda = (-2.85 \pm 0.67)$ keV^{-1}, $C = 5.65 \pm 1.35$. The goodness-of-fit is $\chi^2/\mathrm{NDF} = 0.93$. Even though the quality of the fit is perfect, the uncertainty on μ and σ is much larger than in (a). The integral over the Gaussian returns the number of α-events. Since the width is much smaller than in (a), the rate of α-events in this run is likely underestimated.

Figure 7.7 Two examples of the fit to the α-peak in the singles energy spectrum. The fit function is described by Eq. 7.4. The fit is shown as the brown line. The grey graph displays the α-energies, and the exponential function (blue) approximates the background.

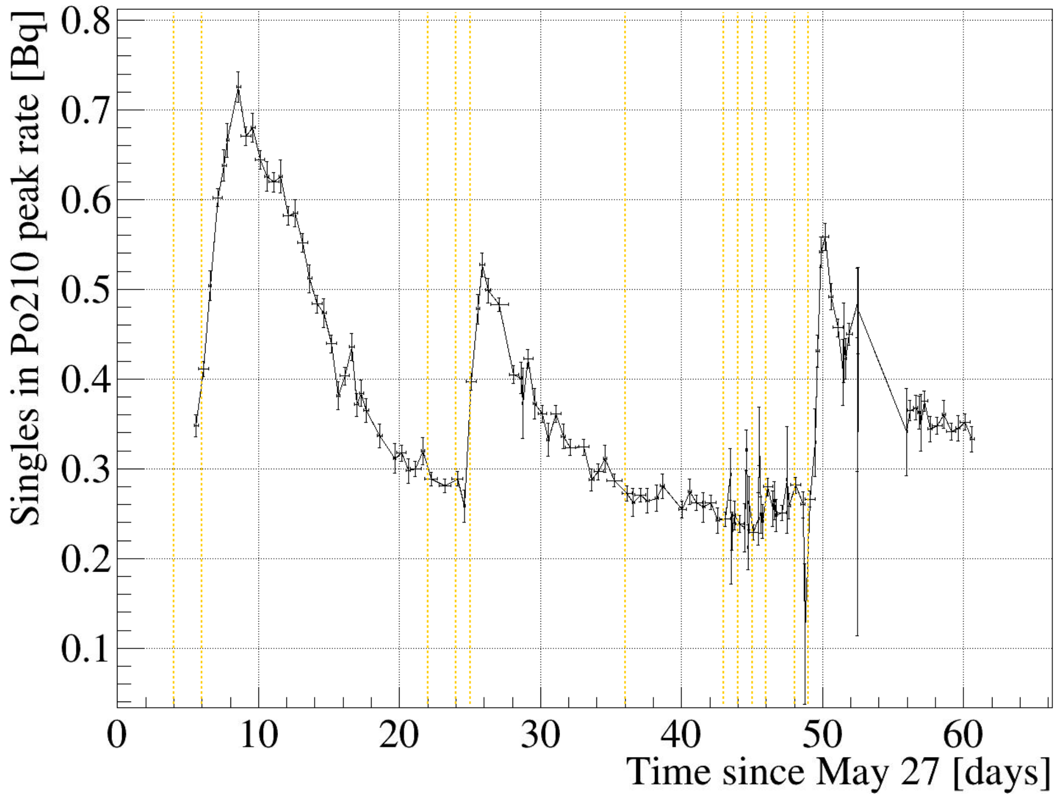

Figure 7.8 The α-event rate of the $300\,\mathrm{keV}$ peak of the singles spectrum as a function of time. The data points start on 1 June and end on 26 July. The orange vertical lines show the detector circulation operations as listed in Table 6.1. After the circulations, the rate increases rapidly.

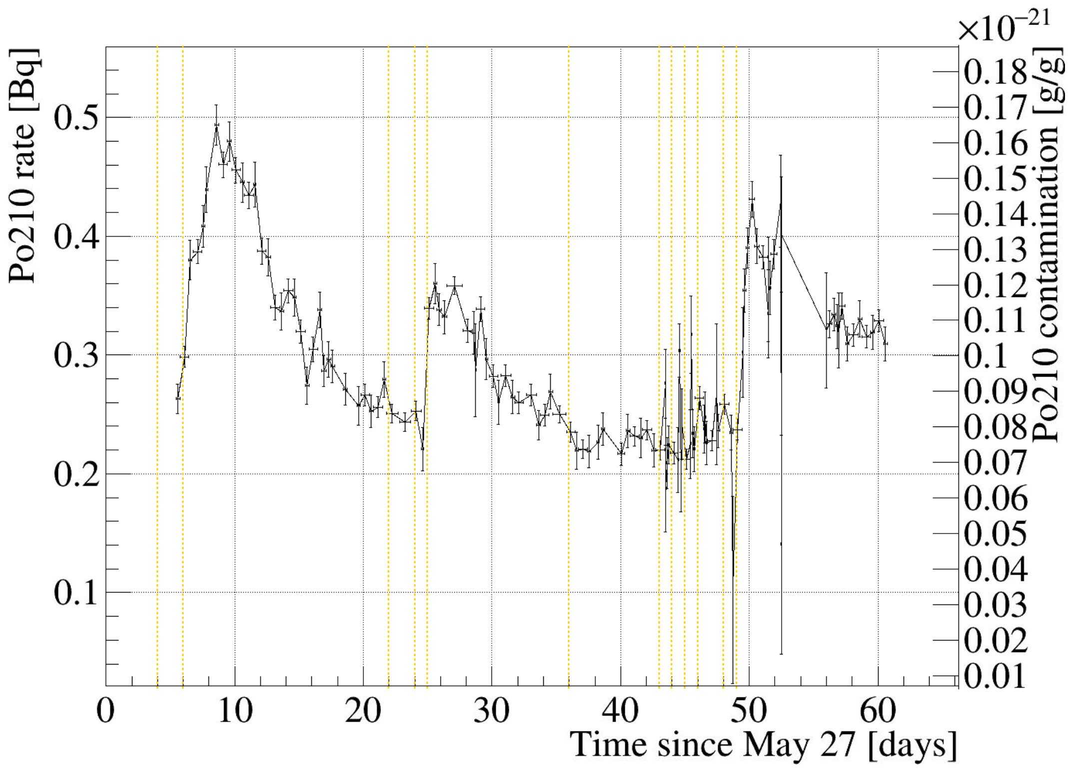

Figure 7.9 The ^{210}Po event rate derived from the α-rate of the singles spectrum (Fig. 7.8) as a function of time. The data points start on 1 June and end on 26 July. The orange vertical lines show the detector circulation operations listed in Table 6.1. The right y-axis shows the corresponding concentration of ^{210}Po in the LS.

- As is the case for the BiPo analysis in 7.1, simulated spectra for efficiency and uncertainty determination were not available. These would help to understand the backgrounds of the fit region. The region is the sum of many β and α-spectra. Indeed, the ^{232}Th chain also contains multiple α-lines, which can contribute to the $300\,\text{keV}$ peak, especially shortly after AV circulations. If true, this would mean that we are overestimating the ^{210}Po content in the peak and, therefore, the ^{210}Po concentration.

- A more powerful PSD can also help to reject non-α-events.

- Improving the BiPo analysis might also help the ^{210}Po determination. However, due to the long half-life of ^{210}Pb, ^{210}Po is often not in secular equilibrium with the BiPo decays [9].

We can compare the obtained ^{210}Po concentration to other experiments. Table 7.3 shows the reported ^{210}Po rates of two Borexino phases and KamLAND between the end of 2011 and mid-2014. In contrast to these publications, the OSIRIS data has only a very light fiducial volume cut applied ($5\,\text{cm}$ in each dimension corresponding to cutting <$10\,\%$ of the volume). On the contrary, Borexino (2020) tried to find the best fiducial volume to reduce the ^{210}Po concentration. The fiducial volume in KamLAND almost halves the available volume because the surface of the inner vessel contained too much ^{210}Po and spoiled the data. The OSIRIS result is an upper limit and will likely be improved in future analyses. The OSIRIS ^{210}Po concentration is already at least a factor of two better than KamLAND's. Compared to the first phase of Borexino, OSIRIS is worse by two orders of magnitude. Since ^{210}Po is the last decay in the ^{238}U chain and since we observe such high BiPo rates (see Sec. 7.1), the observed polonium decays may not show the intrinsic ^{210}Po contamination, but rather be the result of the reason that also likely enhances the BiPo rate.

While Borexino's ^{238}U rate was three orders of magnitude lower than the ^{210}Po rate [9], the ^{238}U rate in this work is only one order of magnitude lower than the ^{210}Po rate (compare the rates in Fig. 7.3 and 7.9). That the ^{210}Po rate is so much closer to Borexino's is a good sign for the purification effort, especially since the elevated BiPo rate feeds the ^{210}Po decays. If the source of the BiPo events is not the intrinsic radiopurity of the LS and if it can be found and fixed, the ^{210}Po contamination might go down significantly.

Experiment	**Reported ^{210}Po rate**	**Comparable ^{210}Po rate [cpd/100 ton]**
OSIRIS (this work)	0.2 - $0.5\,\text{Bq}$	9.6×10^4 - 2.4×10^5
Borexino (phase I) [9]	500 - $8000\,\text{cpd}/100\,\text{ton}$	5×10^2 - 8×10^3
Borexino (2020) [76]	> $11.5\,\text{cpd}/100\,\text{ton}$	> 11.5
KamLAND [115]	3 - $5\,\text{mBq/m}^3$	2.6×10^5 - 4.3×10^5

Table 7.3 The reported and - for comparison - converted ^{210}Po rates in this work, different phases in Borexino[9][76] and KamLAND[115].

Due to the (α,n)-reactions which mimic the IBD signal, ^{210}Po can be a dangerous contamination for JUNO. To estimate its impact on the reactor neutrino program, I use the information gained by the KamLAND collaboration on the rate of (α,n)-reactions [116]. By dividing the number (α,n)-reactions by the total number of ^{210}Po decays, I calculate the probability of such a reaction occurring. With this, I determine the rate of these reactions [111]:

$$R = \frac{cMN}{m\tau N_\alpha} = (0.66 \pm 0.13)\,\text{day}^{-1}, \tag{7.7}$$

where $c = (7 \pm 1) \cdot 10^{-23}$ is the mass concentration of ^{210}Po , $M = 20\,\text{kton}$ the LS mass in the JUNO detector, m the atomic mass of ^{210}Po and τ its lifetime. $N = 182.0 \pm 21.7$ and $N_\alpha = (5.56 \pm 0.22) \cdot 10^9$ were determined in the KamLAND dataset.

Compared to the expected reactor neutrino reactions of $\sim 60\,\text{day}^{-1}$, the calculated rate of background events is low but much higher than foreseen in the NMO determination program [33]. However, the concentration of ^{210}Po measured in this work is at least one order of magnitude higher than the design goal. Additionally, I used the whole detector volume for this approximation. In reality, a fiducial volume cut will be applied for all analyses including in the study predicting JUNO's sensitivity to the NMO [33]. Since these quantities are proportional to the (α,n)-reaction rate, it will decrease as well.

7.3 Search for additional α-Lines

As mentioned before, Fig. 7.6b contains another peak-like structure at $500\,\text{keV}$. This peak appears in runs of days shortly after the AV circulation operations. This suggests that a fast-decaying isotope is introduced during the circulations.

I analyze this secondary peak analogously to the ^{210}Po peak in Sec. 7.2. The difference is that this peak is very small or not detectable in many data sets. I extend the fit region to include the $300\,\text{keV}$ and $500\,\text{keV}$ peaks and the fit function (Eq. 7.4) by an additional Gaussian function:

$$f(E) = N_{300} \exp\left(-0.5 \cdot \left(\frac{E - \mu_{300}}{\sigma_{300}}\right)^2\right) + N_{500} \exp\left(-0.5 \cdot \left(\frac{E - \mu_{500}}{\sigma_{500}}\right)^2\right) + Ce^{\lambda E}. \tag{7.8}$$

N_i, μ_i, σ_i are the Gaussian function parameters, where the index indicates the Gaussian fit to the $300\,\text{keV}$ or $500\,\text{keV}$ peak, respectively. These six parameters, λ, and C, are the free parameters of the fit. The fit does not generally converge meaningfully, especially when the secondary peak is not visible. Therefore, I restrict the available range for the Gaussian functions' fit parameters, assuming peaks at $300\,\text{keV}$ and $500\,\text{keV}$. Without a comprehensive model for the spectrum with all backgrounds, this fit only returns an estimation of the α events.

Fig. 7.10 shows the energy spectra and the fits for two examples: Fig. 7.10a shows Run 9, which took place shortly after an AV circulation, making the secondary peak very pronounced. In contrast, Fig. 7.10b displays Run 114, where the additional peak does not appear.

Isotope	Life time τ	Energy [keV]	Decay mode
^{232}Th	2.03×10^{10} years	4010	α
^{228}Ra	8.31 years	46	$\beta^-\gamma$
^{228}Ac	8.84 h	2140	$\beta^-\gamma$
^{228}Th	2.76 years	5520	α
^{224}Ra	5.28 days	5690	α
^{220}Rn	80.2 s	6290	α
^{216}Po	209 ms	6780	α
^{212}Pb	15.3 h	573	$\beta^-\gamma$
^{212}Bi (64%)	87.4 min	2250	β^-
^{212}Bi (36%)	87.4 min	6050	α
^{212}Po	431 ns	8780	α
^{208}Tl	4.4 min	4990	$\beta^-\gamma$

Table 7.4 The most notable isotopes of the ^{232}Th chain with their respective lifetimes, maximum released energy, and decay mode. Alternative decay branches and the γ-lines accompanying many decays are not listed.

I determine the rate of α-events in analogy to the singles rate in Sec. 7.2 by calculating the number of events in the fitted α-peak and dividing this number by the length of the run. Fig. 7.11 shows the resulting α-rate. The orange lines in Fig. 7.11 display the AV circulations. We observe a rise of the α-rate after the circulations before day 40. The situation for the last six circulations is unclear. Many

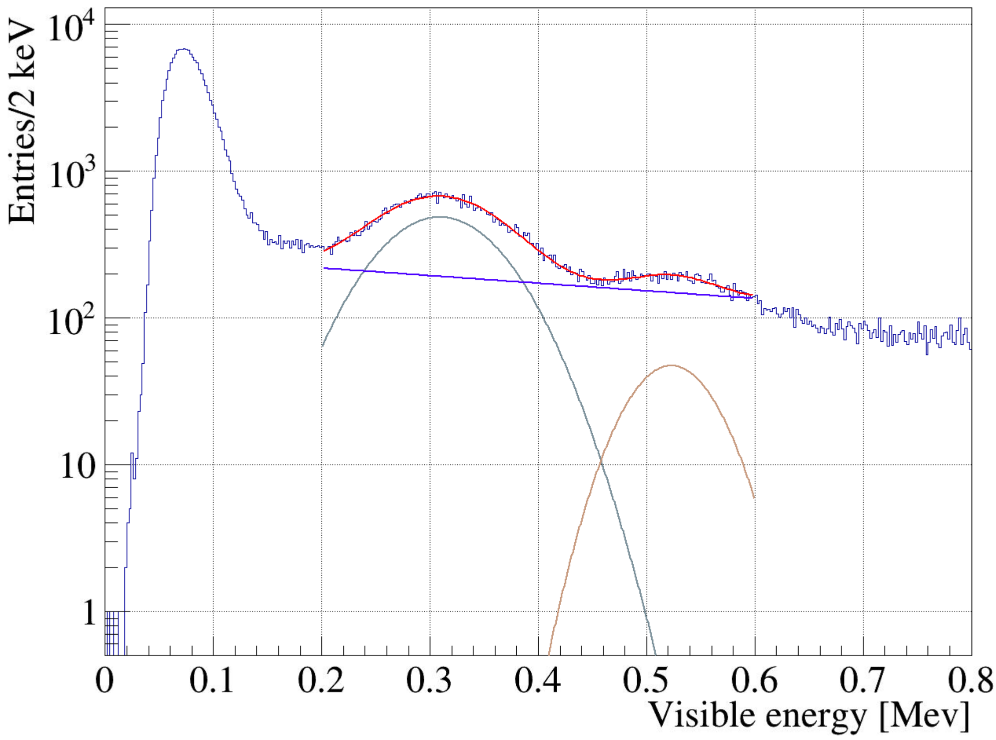

(a) An example (Run 9) for the fit of data set recorded shortly after an AV circulation. The peak at 500 keV is visible. The best-fit values are $N_{300} = 485.24 \pm 8.86$, $\mu_{300} = (0.310 \pm 0.001)$ keV , $\sigma_{300} = (0.054 \pm 0.002)$ keV, $N_{500} = 47.26 \pm 7.04$, $\mu_{500} = (0.520 \pm 0.003)$ keV , $\sigma_{500} = (0.038 \pm 0.008)$ keV, $\lambda = (-1.19 \pm 0.19)$ keV^{-1} , $C = 277.24 \pm 25.54$. The goodness-of-fit is $\chi^2/\mathrm{NDF} = 1.13$.

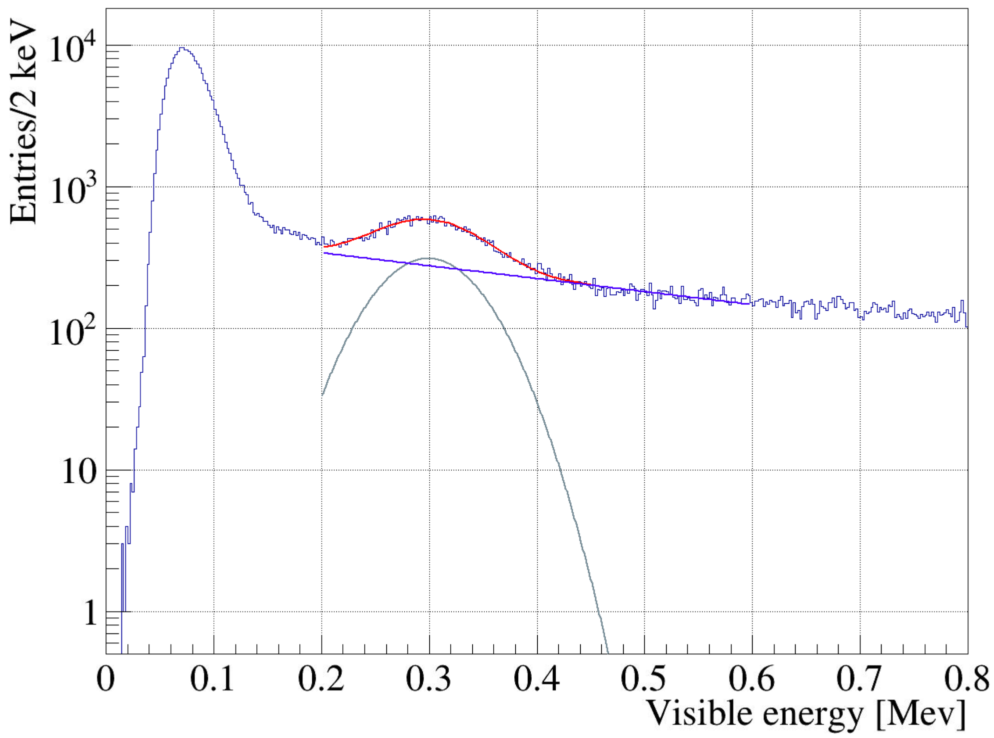

(b) An example (Run 94) for the fit of most data sets where the 500 keV peak has already decayed. The best-fit values are $N_{300} = 310.60 \pm 4.49$, $\mu_{300} = (0.299 \pm 0.001)$ keV , $\sigma_{300} = (0.047 \pm 0.001)$ keV, $N_{500} = 0.000 \pm 0.773$, $\mu_{500} = (0.510 \pm 0.021)$ keV , $\sigma_{500} = (0.030 \pm 0.008)$ keV, $\lambda = (-2.12 \pm 0.02)$ keV^{-1} , $C = 521.28 \pm 2.00$. The goodness-of-fit is $\chi^2/\mathrm{NDF} = 1.30$.

Figure 7.10 Two examples of the fit to both α-peaks in the singles energy spectrum. The fit function is described by Eq. 7.8. The fit is shown as the red line. The grey graph displays the α-events investigated in Sec. 7.2, the brown line represents the secondary α-peak, and the exponential function (blue) approximates the background.

data points after day 40 have large uncertainties because many runs were short. However, there are also data points interspersed with a longer length and, hence, much more statistics. Some of these also show no decay but much smaller uncertainties. This suggests that the fit does not work properly or that almost no new contaminants reached the detector during the later circulations. In general, many data points are compatible with zero.

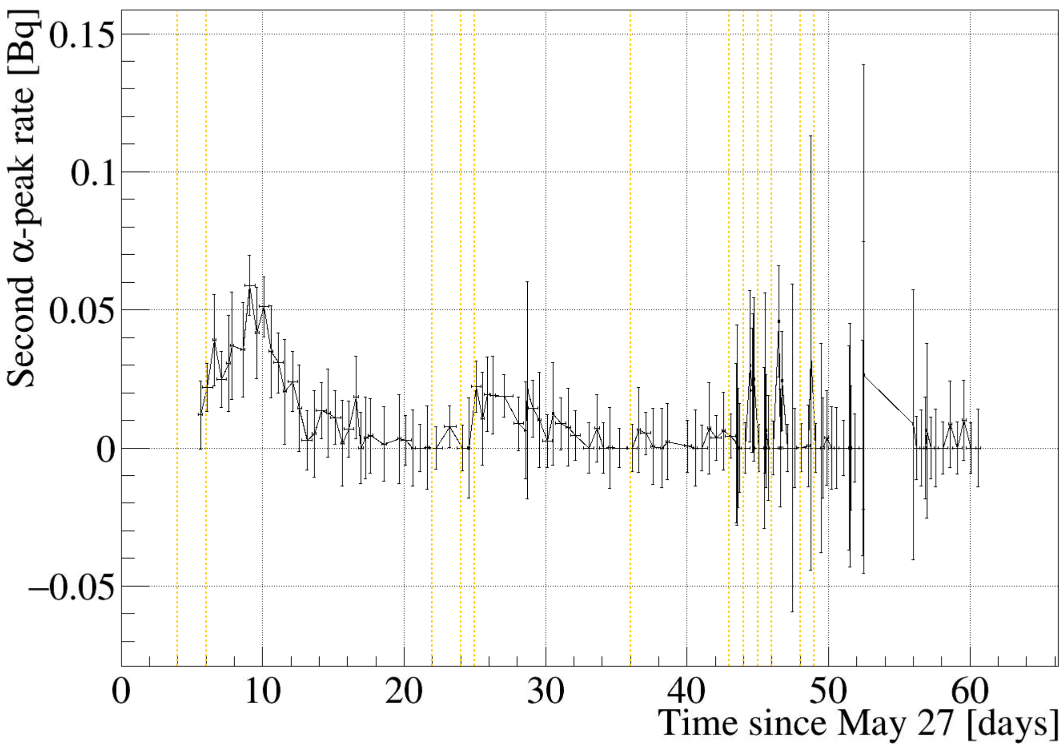

Figure 7.11 The rate of events in the second α-peak of the singles spectrum calculated by fitting it (see Fig. 7.10) for each run and dividing by the run length. The orange lines represent the AV circulations (see Table 6.1).

Assuming it's another α-peak, its mean is approximately $500\,\text{keV}$ visible energy. With a linear energy-to-light conversion from the ^{210}Po peak, this translates to roughly $8700\,\text{keV}$. This peak also seems to decay faster than the BiPo rate investigated in Sec. 7.1. Table 7.4 shows the lifetimes, energies, and decay modes of all ^{232}Th daughters. Together with Table 7.2, we can see that only one α decay has such high energies: ^{212}Po. Furthermore, the ^{232}Th decay chain also contains a radon isotope, ^{220}Rn, that decays much faster to its endpoint ^{208}Tl than ^{222}Rn decays to its endpoint ^{206}Pb. This fits the observation that this additional peak decays faster than the BiPo rate.

However, the visible energy of the second α-peak is the same as that of the ^{214}Po peak (see Fig. 7.2). This can be illustrated in another way by plotting the visible energy of the α-peaks as a function of the energy of their presumed origin. In the case of the second peak in the singles spectrum, the assumption is that it originates from ^{212}Po .

Fig. 7.2 shows the distribution of ^{214}Po α-energies. I take the mean μ_i of the fit as the visible energy of this decay and σ_i as its uncertainty. For ^{210}Po and ^{212}Po , I take the fitted means and sigmas of the singles spectra of all runs - i.e., Fig. 7.7 and Fig. 7.10, respectively - as shown in Fig. 7.12. The mean of these means is the visible energy of the respective peak. Table 7.5 shows the results.

Fig. 7.13 displays the visible energies of the α-decays as a function of the α-energies. Evidently, the second peak cannot be due to ^{212}Po decays. Another possible hypothesis is that it originates from the ^{215}Po decay, which is part of the decay chain of ^{235}U, which also contains a radon isotope, ^{219}Rn. ^{215}Po undergoes α-decay with an energy of $7.38\,\text{MeV}$. However, as Fig. 7.11 shows, the decay time of the contaminants introduced by the AV circulations is in the order of days. Observe, e.g., the decay time of the peak at day 10. The decay chain from ^{219}Rn does not include any dominant decay with a lifetime

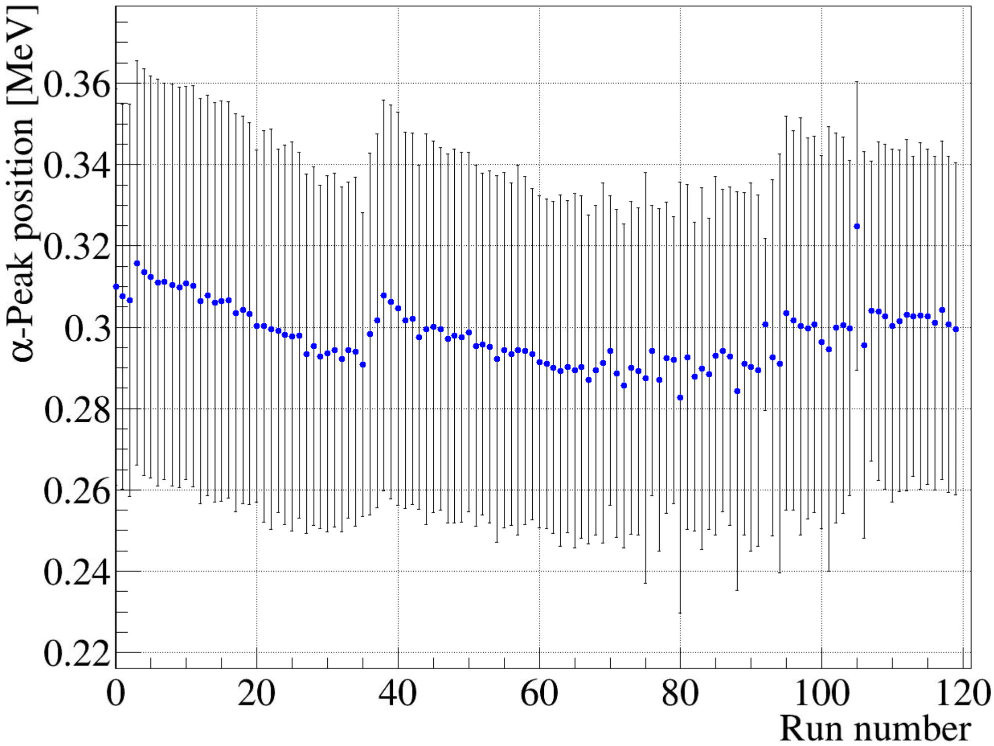

(a) The means of the 300 keV visible energy peak corresponding to the ^{212}Po 5410 keV line.

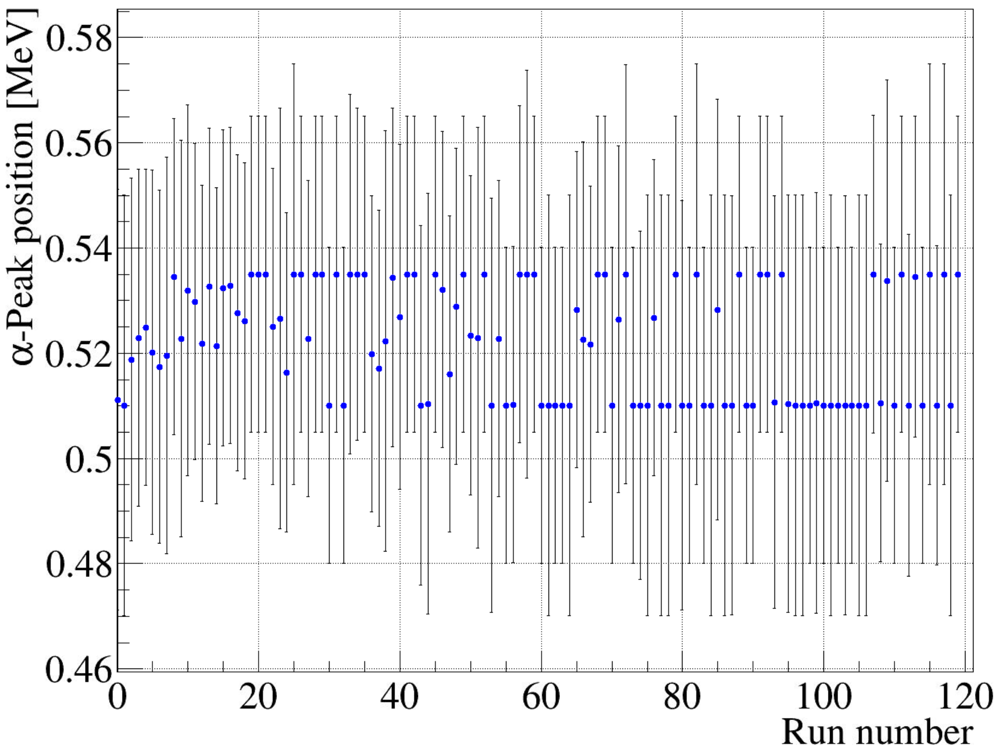

(b) The means of the 500 keV visible energy peak corresponding to the ^{210}Po 8780 keV line.

Figure 7.12 The means of the Gaussians which fit the two α-peaks in the singles spectrum. The blue dots are the mean values, and the black bars are the uncertainties, which are the σ of the fits.

Isotope	α-energy [keV]	Visible energy [keV]
^{214}Po	5410	0.298 ± 0.049
^{210}Po	7690	0.544 ± 0.052
^{212}Po	8780	0.522 ± 0.041

Table 7.5 The energies of the three α-decays, ^{214}Po , ^{210}Po , and ^{212}Po , investigated in this work together with their measured visible energies.

longer than a few minutes. Hence, even if ^{219}Rn is introduced during AV circulations, it would, at most, show up in one detector run, which usually lasts many hours.

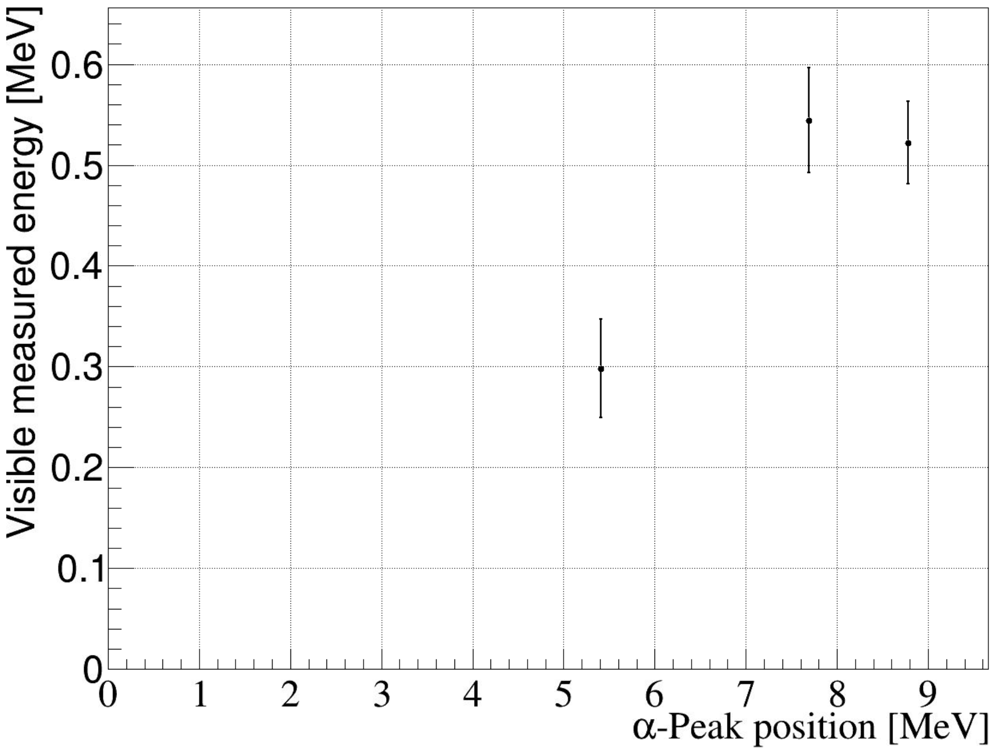

Figure 7.13 The measured visible energies of the α-energy spectra of ^{214}Po , ^{210}Po , and the second α-peak in the singles spectrum as a function of the α-energy of the decay (see Table 7.5).

I constructed the singles spectrum by demanding that each event is not part of a BiPo-214 coincidence and that no other event happened in the $2\,\mathrm{ms}$ after it. Theoretically, this prevents all events in the singles spectrum from being ^{214}Po decays. However, the efficiency of detecting a BiPo coincidence is not $100\,\%$. As discussed in Sec. 7.1, the total efficiency is $82\,\%$, dominated by the fiducial volume cut. Therefore, I expect a contribution of ^{214}Po decays to the singles spectrum.

The maximal height of the BiPo-214 rate around day 8 in Fig. 7.3 is approximately $0.105\,\mathrm{Bq}$, which is efficiency-corrected. Therefore, the rate of ^{214}Po decays showing up in the singles spectrum at this time is $15\,\%$ of this, ca. $0.016\,\mathrm{Bq}$. This is only one-third of the rate observed in Fig. 7.11. Additionally, the decay time of this peak in the α-rate evolution is - while hard to pin down exactly - less than the lifetime of ^{222}Rn from which it would originate; see the discussion in Sec. 7.1.

Therefore, the source of the second α-peak in the singles spectrum is unclear. The fitting of this peak would profit significantly from a complete understanding of the whole spectrum. The peak may be enhanced by other α- or β-spectra. On the other hand, the efficiency of BiPo detection might be overestimated. Both of these problems might be solved by comparison with a simulated spectrum of the detector.

Chapter 8

Conclusions and Outlook

This thesis presents the studies of two properties of liquid scintillators (LS) in the context of the JUNO experiment. The Jiangmen Underground Neutrino Observatory (JUNO) is a $20\,\mathrm{kton}$ LS experiment at the final stage of commissioning in South China. Its main goal is the determination of the neutrino mass ordering (NMO), and it additionally features a rich physics program. For the NMO resolution, the experiment will measure the energy spectrum of $\bar{\nu}_e$ produced in two nuclear power plants at a distance of $52\,\mathrm{km}$.

The measurement of the NMO relies on the resolution of the phase shift between the normal ordering (NO) and inverted ordering (IO) of the oscillated neutrino energy spectrum. This requires an energy resolution of $3\,\%$ at $1\,\mathrm{MeV}$ and excellent knowledge of the absolute energy scale. However, it also depends upon the exact understanding of the light yield as a function of the deposited energy. This function is nonlinear and often differently parametrized depending on the incident particle. Birks' law is a common semi-empirical approach that relies on the experimentally measured parameter kB.

In this work, I investigated the cause of the large systematic uncertainty and subsequent large range of possible kB values resulting from a laboratory-scale experiment to determine the electron nonlinearity in [65]. In that work, a ^{137}Cs source irradiates a sample of the JUNO LS contained in a Teflon cell to which a PMT is attached. This is the light detector, which is operated in coincidence with a high-purity germanium (HPGe) detector that measures the γ's remaining energy after scattering in the LS. kB was found to be between 0.008 and $0.025\,\mathrm{cm/MeV}$.

In the present thesis, I discovered that the light detector features large inhomogeneities of its charge collection depending on where the energy deposition occurred in the cell. The inhomogeneities have a complicated form as they are also charge-dependent, but they can be higher than $10\,\%$ for positions that are only $3.2\,\mathrm{cm}$ apart. These deviations can cause the observed variations of Birks' constant kB. Despite efforts of multiple groups within JUNO, a convincing measurement of the electron nonlinearity is a very challenging task and is an ongoing effort. For JUNO's goal, the measurement is critical and must be addressed. An improved experimental setup incorporating lessons learned in this work is currently under construction at the University of Mainz.

Of course, JUNO's rich physics program also depends on the radiopurity of the LS. For the NMO resolution, the concentrations of the long-lived decay chains starting at ^{238}U and ^{232}Th must not exceed $1 \times 10^{-15}\,\mathrm{g/g}$. To ensure this level of purity, the LS undergoes a rigorous cleaning procedure on-site just before filling into the detector. As a last check, roughly $15\,\%$ of the LS will pass through the OSIRIS detector, ensuring the required contamination levels are not exceeded.

In the context of this work, I have overseen, managed, and developed the first and current working implementation of an online analysis framework for OSIRIS. Since the detector is tasked to warn when the radiopurity is subpar, the incoming data must be analyzed continuously in real-time. The analysis framework RootSorter (RS) builds on an existing implementation developed at the COSY accelerator and was adapted to OSIRIS. After the initially foreseen PMTs became defective, spare ones from JUNO and the corresponding data acquisition system (DAQ) were implemented in OSIRIS. I made the necessary adjustments to the data read-in. Additionally, I developed a waveform reconstruction algorithm and implemented a waveform smoothing filter, which increases the signal-to-noise ratio by a factor of two. Moreover, I proposed and realized a convenient output data format enabling easy access to the processed for offline analyses. Lastly, I made visualizations of the data available for quick online access. Without the functioning RS, this and most other analyses would not have been possible. Since it is an essential tool for the functionality of OSIRIS, it is also critical for the whole JUNO project.

Pulse shape discrimination (PSD) is a powerful and essential tool in many proposed analysis strategies in JUNO. PSD exploits the light emission profile differences between different particle types to identify which particle caused an energy deposition. Differentiating between, e.g., α- and β-particles by their pulse shape can help OSIRIS improve its sensitivity to particular decays. Additionally, the PSD performance in OSIRIS can give hints on its applicability in JUNO. I performed the first PSD study of the JUNO LS in a large-scale detector. By restricting the fiducial volume to the innermost part of the detector, I was able to show that α/β-discrimination performances of close to $70\,\%$ are possible. Considering the very large transit-time spread of the used PMTs, this is a surprisingly good result. By improving OSIRIS' current waveform reconstruction algorithm, it will be possible to apply PSD on the full detector volume, adding a valuable tool to many analysis programs for background rejection.

The ^{238}U and ^{232}Th contaminations of the LS are particularly interesting for JUNO as they are the starting isotopes of very long-lived decay chains. To get a first estimation of the LS radiopurity, I have presented analyses of OSIRIS data taken between 1 June and 27 July 2024. Both isotopes are commonly inferred by a coincidence structure between a bismuth and a polonium isotope. For ^{238}U , the lifetime of ^{214}Po is $236\,\mu s$. Detecting the coincidence between its α-decay and the β-decay of ^{214}Bi was possible with an efficiency of $82.0\,\%$. Multiple circulations/exchanges of the LS tested the detector's functionality and performance in the analyzed period. These usually introduced a high rate of BiPo coincidences, most likely by the import of external ^{222}Rn , which is also part of the ^{238}U chain and followed by the BiPo coincidence. The ^{238}U concentration of the LS can only be inferred from the rate of BiPos under the assumption of secular equilibrium, which is broken when external radon enters the detector.

I confirmed the increase and subsequent decrease in the BiPo concentration upon LS circulations. The decay time of the BiPo rate after a detector operation is consistent with the lifetime of ^{222}Rn. In the periods after the ^{222}Rn had decayed, I calculated the lowest observed ^{238}U concentration in the investigated data set to be $(1.1 \pm 0.4) \cdot 10^{-14}$ g/g; a result agreeing with other data analyses. If this were the intrinsic contamination of the LS, JUNO's whole program would be in jeopardy. However, independent radiopurity measurements - triggered by this OSIRIS data - using neutron activation analysis suggest that the contamination is at $< 0.8 \times 10^{-15}$ g/g. Additionally, more recent results with newer data sets of OSIRIS and a restrictive fiducial volume cut also return an upper limit on the ^{238}U concentration close to 1×10^{-15} g/g. This hints that external backgrounds limit the detector's sensitivity. The OSIRIS group suspects entry points of external radon into the detector and is working hard to fix the cause.

The ^{232}Th chain's BiPo coincidence is experimentally much more challenging because the ^{212}Po has a lifetime of only $433\,ns$. Currently, the RS analysis cannot reliably find coincidences of events separated by less than $600\,ns$ In the future, improving the event-finding algorithm in the RS should be a high priority since determining the ^{232}Th concentration is critical for JUNO.

In the energy spectrum of isolated events, the singles spectrum, all events apart from the identified BiPo coincidences show up, including all other decays from the decay chains. By identifying specific peaks in the spectrum, we can measure the decay rates of different isotopes undergoing α-decay. They can enable cross-checks on the inferred mother isotope concentration. On the other hand, disturbances of the secular equilibrium might necessitate alternative methods to determine the abundance of other isotopes.

^{210}Po ends the ^{238}U decay chain and is an isotope often out of equilibrium with the BiPo coincidences. As ^{210}Pb has a significantly longer lifetime than the BiPo isotopes after which it occurs, the ^{210}Po rate depends on the ^{210}Pb concentration. Due to its ability to initiate $\alpha(^{13}\mathrm{C}, n)^{16}\mathrm{O}$ reactions that mimic the IBD signal, ^{210}Po is a dangerous background for several searches in JUNO, especially the NMO determination. Exploiting the peak in the singles spectrum, I have, for the very first time, determined the ^{210}Po concentration to be around $(7 \pm 1) \cdot 10^{-23}$ g/g. This is almost two orders of magnitude above the design goal. However, even this concentration would introduce a correlated background signal contamination of the reactor neutrino spectrum of, at most, $\sim 1\,\%$. A continuous influx of, e.g., external radon would negatively affect the ^{210}Po concentration. As a radon leak seems likely at the moment, the chances are good that the ^{210}Po rate will decrease significantly once the source of external radon is found and fixed.

I also attempted to identify additional α-lines in the singles spectrum. However, a working detector simulation chain is required to better understand the spectrum.

Without OSIRIS, JUNO would risk highly contaminated LS entering the detector, possibly spoiling the experiment. After the first batches of the JUNO LS were cleaned as foreseen for the experiment, OSIRIS delivered unique data on the LS quality. My contributions to OSIRIS enabled immediate analysis - both offline and online - of the first LS data in March 2024. They were instrumental in assessing the detector's performance and the LS.

To further enhance the analysis of OSIRIS, the RS can be improved. Integrating the detector simulation data information would help identify weaknesses in the analysis chain. Furthermore, it would enable a rigorous treatment of the detection efficiencies for all analyses. An improvement of the waveform reconstruction is necessary to facilitate PSD in the whole detector volume. PSD would pave the way for new analysis approaches and better detection efficiencies. Lastly, by making the event reconstruction more sophisticated, the correct identification of multiple events in one recording window becomes more reliable. This is especially important for the fast BiPo-212 coincidence, which is a powerful tool for the ^{232}Th concentration determination.

Acronyms

ACU automatic calibration unit.

ADC analog-to-digital converter.

AV acrylic vessel.

bis-MSB 1,4-bis(2-methylstyryl) benzene.

CC charged current.

CD central detector.

DAQ data acquisition system.

EB EventBuilder.

ES elastic scattering.

GCU global control unit.

HDPE high-density polyethylene.

HPGe high-purity germanium.

IBD inverse beta decay.

ID inner detector.

IO inverted ordering.

JUNO Jiangmen Underground Neutrino Observatory.

LAB linear alkylbenzene.

LHS liquid handling system.

LPMT large PMT.

LS liquid scintillator.

NC neutral current.

NMO neutrino mass ordering.

NO normal ordering.

OD outer detector.

p.e. photoelectron.

PET polyethylene terephthalate.

PMT photo-multiplier tube.

PMT Id PMT identifier.

PPO 2,5-diphenyloxazole.

PSD pulse shape discrimination.

RLY relative light yield.

RS RootSorter.

SF steel frame.

SGF Savitzky-Golay filter.

SM Standard Model.

T2T tail-to-total.

TT top tracker.

WCD water Cherenkov detector.

WT water tank.

Bibliography

[1] Q. R. Ahmad *et al.* “Direct Evidence for Neutrino Flavor Transformation from Neutral-Current Interactions in the Sudbury Neutrino Observatory”. In: *Phys. Ref. Lett.* 89, 011301 (2005).

[2] Y. Fukuda *et al.* “Evidence of Oscillation of Atmospheric Neutrinos”. In: *Phys. Lett.* 81, 1562 (1998).

[3] N. Schmitz. *Neutrinophysik*. Stuttgart: Teubner Studienbücher, 1997.

[4] Z Maki, M. Nakagawa, and S. Sakata. “Remarks on the Unified Model of Elementary Particles”. In: *Prog. Theor. Phys.* 20 (1968).

[5] B. Kayser. *Neutrinos in Particle Physics, Astrophysics and Cosmology*. CRC Press, 2009.

[6] S. Navas et al. “Review of particle physics”. In: *Phys. Rev. D* 110.3 (2024), p. 030001. 10.1103/PhysRevD.110.030001.

[7] S.M. Bilenky. *On the phenomenology of neutrino oscillations in vacuum*. 2012. arXiv: hep-ph/1208.2497.

[8] J. Hosaka *et al.* “Solar Neutrino Measurements in Super-Kamiokande-I”. In: *Phys. Rev. D* 73, 112001 (2006). arXiv: hep-ex/0508053.

[9] G. Bellini et al. “Final results of Borexino Phase-I on low-energy solar neutrino spectroscopy”. In: *Phys. Rev. D* 89 (11 June 2014), p. 112007. 10.1103/PhysRevD.89.112007. URL: https://link.aps.org/doi/10.1103/PhysRevD.89.112007.

[10] J. L. Hewett *et al. Fundamental Physics at the Intensity Frontier*. 2012. arXiv: 1205.2671.

[11] P. F. de Salas et al. “2020 global reassessment of the neutrino oscillation picture”. In: *JHEP* 02 (2021), p. 071. 10.1007/JHEP02(2021)071. arXiv: 2006.11237 [hep-ph].

[12] P. F. De Salas et al. *Chi2 profiles from Valencia neutrino global fit*. http://globalfit.astroparticles.es/. 2021. 10.5281/zenodo.4726908. URL: %7Bhttps://doi.org/10.5281/zenodo.4726908%7D.

[13] JUNO Collaboration. “Neutrino Physics with JUNO”. In: (2015). arXiv: 1507.05613v1.

[14] H. Minakata *et al.* “Determination of the Neutrino Mass Hierarchy via the Phase of the Disappearance Oscillation Probability with a Monochromatic $\bar{\nu}_e$ Source”. In: *Phys. Rev. D* 76, 053004 (2005). arXiv: hep-ph/0701151.

[15] Steen Hannestad and Thomas Schwetz. “Cosmology and the neutrino mass ordering”. In: *Journal of Cosmology and Astroparticle Physics* 2016.11 (Nov. 2016), p. 035. 10.1088/1475-7516/2016/11/035. URL: https://dx.doi.org/10.1088/1475-7516/2016/11/035.

[16] Amol S. Dighe and Alexei Yu. Smirnov. “Identifying the neutrino mass spectrum from a supernova neutrino burst”. In: *Phys. Rev. D* 62 (3 July 2000), p. 033007. 10.1103/PhysRevD.62.033007. URL: https://link.aps.org/doi/10.1103/PhysRevD.62.033007.

[17] S F King. “Neutrino mass models”. In: *Reports on Progress in Physics* 67.2 (Dec. 2003), p. 107. 10.1088/0034-4885/67/2/R01. URL: https://dx.doi.org/10.1088/0034-4885/67/2/R01.

[18] X. Qian and J. L. Vogel P. *et al. Fundamental Physics at the Intensity Frontier*. 2015. arXiv: 1505.01891.

[19] M. G. Aartsen et al. “Determining neutrino oscillation parameters from atmospheric muon neutrino disappearance with three years of IceCube DeepCore data”. In: *Phys. Rev. D* 91 (7 Apr. 2015), p. 072004. 10.1103/PhysRevD.91.072004. URL: https://link.aps.org/doi/10.1103/PhysRevD.91.072004.

[20] K. Abe et al. “The T2K experiment”. In: *Nuclear Instruments and Methods in Physics Research Section A: Accelerators, Spectrometers, Detectors and Associated Equipment* 659.1 (2011), pp. 106–135. ISSN: 0168-9002. https://doi.org/10.1016/j.nima.2011.06.067. URL: https://www.sciencedirect.com/science/article/pii/S0168900211011910.

[21] B. Abi et al. *Deep Underground Neutrino Experiment (DUNE), Far Detector Technical Design Report, Volume II: DUNE Physics*. 2020. arXiv: 2002.03005 [hep-ex]. URL: https://arxiv.org/abs/2002.03005.

[22] M. G. Aartsen et al. “Combined sensitivity to the neutrino mass ordering with JUNO, the IceCube Upgrade, and PINGU”. In: *Phys. Rev. D* 101 (3 Feb. 2020), p. 032006. 10.1103/PhysRevD.101.032006. URL: https://link.aps.org/doi/10.1103/PhysRevD.101.032006.

[23] Anatael Cabrera et al. “Synergies and prospects for early resolution of the neutrino mass ordering”. In: *Scientific Reports* 12.1 (Mar. 2022), p. 5393. ISSN: 2045-2322. 10.1038/s41598-022-09111-1. URL: https://doi.org/10.1038/s41598-022-09111-1.

[24] “JUNO physics and detector”. In: *Progress in Particle and Nuclear Physics* 123 (0146-6410 2022), p. 103927. https://doi.org/10.1016/j.ppnp.2021.103927. URL: https://www.sciencedirect.com/science/article/pii/S0146641021000880.

[25] Angel Abusleme and et al. “Mass testing and characterization of 20-inch PMTs for JUNO”. In: *The European Physical Journal C* 82.12 (Dec. 2022), p. 1168. ISSN: 1434-6052. 10.1140/epjc/s10052-022-11002-8. URL: https://doi.org/10.1140/epjc/s10052-022-11002-8.

[26] Angel Abusleme and et al. “The JUNO experiment Top Tracker”. In: *Nuclear Instruments and Methods in Physics Research Section A: Accelerators, Spectrometers, Detectors and Associated Equipment* 1057 (0168-9002 2023), p. 168680. https://doi.org/10.1016/j.nima.2023.168680. URL: https://www.sciencedirect.com/science/article/pii/S0168900223006708.

[27] T. Adam et al. “The OPERA experiment Target Tracker”. In: *Nuclear Instruments and Methods in Physics Research Section A: Accelerators, Spectrometers, Detectors and Associated Equipment* 577.3 (2007), pp. 523–539. ISSN: 0168-9002. https://doi.org/10.1016/j.nima.2007.04.147. URL: https://www.sciencedirect.com/science/article/pii/S0168900207007553.

[28] Anna C. Hayes and Petr Vogel. “Reactor Neutrino Spectra”. In: *Annual Review of Nuclear and Particle Science* 66.Volume 66, 2016 (2016), pp. 219–244. ISSN: 1545-4134. https://doi.org/10.1146/annurev-nucl-102115-044826. URL: https://www.annualreviews.org/content/journals/10.1146/annurev-nucl-102115-044826.

[29] Angel Abusleme and et al. *The Design and Sensitivity of JUNO’s scintillator radiopurity predetector OSIRIS*. 2021. arXiv: 2103.16900 [physics.ins-det].

[30] Angel Abusleme and et al. *TAO Conceptual Design Report: A Precision Measurement of the Reactor Antineutrino Spectrum with Sub-percent Energy Resolution*. 2020. arXiv: 2005.08745 [physics.ins-det].

[31] Jie Zhao et al. “Model-independent Approach of the JUNO 8B Solar Neutrino Program”. In: *The Astrophysical Journal* 965.2 (Apr. 2024), p. 122. 10.3847/1538-4357/ad2bfd. URL: https://dx.doi.org/10.3847/1538-4357/ad2bfd.

[32] Angel Abusleme et al. “JUNO sensitivity to 7Be, pep, and CNO solar neutrinos”. In: *Journal of Cosmology and Astroparticle Physics* 2023.10 (Oct. 2023), p. 022. 10.1088/1475-7516/2023/10/022. URL: https://dx.doi.org/10.1088/1475-7516/2023/10/022.

[33] Liang Zhan et al. “Potential to Identify the Neutrino Mass Ordering with Reactor Antineutrinos in JUNO”. In: *Chinese Physics C* (2024). URL: http://iopscience.iop.org/article/10.1088/1674-1137/ad7f3e.

[34] Particle Data Group et al. “Review of Particle Physics”. In: *Progress of Theoretical and Experimental Physics* 2020.8 (Aug. 2020), p. 083C01. ISSN: 2050-3911. 10.1093/ptep/ptaa104. eprint: https://academic.oup.com/ptep/article-pdf/2020/8/083C01/34673722/ptaa104.pdf. URL: https://doi.org/10.1093/ptep/ptaa104.

[35] Angel Abusleme et al. “Sub-percent precision measurement of neutrino oscillation parameters with JUNO”. In: *Chinese Physics C* 46.12 (Dec. 2022), p. 123001. 10.1088/1674-1137/ac8bc9. URL: https://dx.doi.org/10.1088/1674-1137/ac8bc9.

[36] X. Qian et al. *Unitarity Tests of the Neutrino Mixing Matrix*. 2013. arXiv: 1308.5700 [hep-ex]. URL: https://arxiv.org/abs/1308.5700.

[37] Núria Vinyoles et al. “A New Generation of Standard Solar Models”. In: *The Astrophysical Journal* 835.2 (Jan. 2017), p. 202. 10.3847/1538-4357/835/2/202. URL: https://dx.doi.org/10.3847/1538-4357/835/2/202.

[38] Joel N. Butler et al. *Report of the 2021 US Community Study on the Future of Particle Physics (Snowmass 2021)*. Jan. 2023. 10.2172/1922503. URL: https://www.osti.gov/biblio/1922503.

[39] R. Matsumoto et al. “Search for proton decay via $p \to \mu^+ K^0$ in 0.37 megaton-years exposure of Super-Kamiokande”. In: *Phys. Rev. D* 106 (7 Oct. 2022), p. 072003. 10.1103/PhysRevD.106.072003. URL: https://link.aps.org/doi/10.1103/PhysRevD.106.072003.

[40] Angel Abusleme and et al. “JUNO sensitivity on proton decay p $\to$ νK+ searches*”. In: *Chinese Physics C* 47.11 (Nov. 2023), p. 113002. 10.1088/1674-1137/ace9c6. URL: https://dx.doi.org/10.1088/1674-1137/ace9c6.

[41] Sai Wang et al. “Constraining primordial black holes as dark matter at JUNO”. In: *Phys. Rev. D* 103 (4 Feb. 2021), p. 043010. 10.1103/PhysRevD.103.043010. URL: https://link.aps.org/doi/10.1103/PhysRevD.103.043010.

[42] Jia-Shu Lu et al. “Constraining absolute neutrino masses via detection of galactic supernova neutrinos at JUNO”. In: *Journal of Cosmology and Astroparticle Physics* 2015.05 (May 2015), p. 044. 10.1088/1475-7516/2015/05/044. URL: https://dx.doi.org/10.1088/1475-7516/2015/05/044.

[43] Yu-Feng Li, Mark Vagins, and Michael Wurm. “Prospects for the Detection of the Diffuse Supernova Neutrino Background with the Experiments SK-Gd and JUNO”. In: *Universe* 8.3 (2022). ISSN: 2218-1997. 10.3390/universe8030181. URL: https://www.mdpi.com/2218-1997/8/3/181.

[44] Ran Han et al. “Potential of geo-neutrino measurements at JUNO*”. In: *Chinese Physics C* 40.3 (Mar. 2016), p. 033003. 10.1088/1674-1137/40/3/033003. URL: https://dx.doi.org/10.1088/1674-1137/40/3/033003.

[45] Chee Sheng Fong, Hisakazu Minakata, and Hiroshi Nunokawa. “A framework for testing leptonic unitarity by neutrino oscillation experiments”. In: *Journal of High Energy Physics* 2017.2 (Feb. 2017), p. 114. ISSN: 1029-8479. 10.1007/JHEP02(2017)114. URL: https://doi.org/10.1007/JHEP02(2017)114.

[46] Jie Cheng et al. “Neutral-current background induced by atmospheric neutrinos at large liquid-scintillator detectors. I. Model predictions”. In: *Phys. Rev. D* 103 (5 Mar. 2021), p. 053001. 10.1103/PhysRevD.103.053001. URL: https://link.aps.org/doi/10.1103/PhysRevD.103.053001.

[47] Yu-Feng Li and Zhen-hua Zhao. “Tests of Lorentz and CPT violation in the medium baseline reactor antineutrino experiment”. In: *Phys. Rev. D* 90 (11 Dec. 2014), p. 113014. 10.1103/PhysRevD.90.113014. URL: https://link.aps.org/doi/10.1103/PhysRevD.90.113014.

[48] Y. Abe *et al.* “Reactor $\overline{\nu}_\mathrm{e}$ Disappearance in the Double Chooz Experiment”. In: *Phys. Rev. D* 86, 052008 (2012).

[49] G. Bellini. “Final Results of Borexino Phase-I on Low Energy Solar Neutrino Spectroscopy”. In: *Phys. Rev. D* 89, 112007 (2014).

[50] K. Eguchi *et al.* “First Results from KamLAND: Evidence for Reactor Antineutrino Disappearance”. In: *Phys. Ref. Lett.* 90, 021802 (2003).

[51] K. P. C. Vollhardt and N. E. Schore. *Organic Chemistry*. W. H. Freeman, 1994.

[52] J. B. Birks. *The Theory and Practice of Scintillation Counting*. First Edition. Pergamon Press, 1964.

[53] J. B. Birks. *The Scintillation Process in Organic Systems*. Vol. 7. IRE Trans. Nuc. Sci., 1964. 10.1109/TNS2.1960.4315726.

[54] A. Jabłoński. “Efficiency of Anti-Stokes Fluorescence in Dyes”. In: *Nature* 131 (1933), pp. 839–840.

[55] “Applications of Liquid Scintillation Counting”. In: *Applications of Liquid Scintillation Counting*. Ed. by DONALD L. HORROCKS. Academic Press, 1974, p. iv. ISBN: 978-0-12-356240-1. https://doi.org/10.1016/B978-0-12-356240-1.50002-0. URL: https://www.sciencedirect.com/science/article/pii/B9780123562401500020.

[56] V. Zimmer. “Studies of Proton Recoil in Organic Liquid Scintillators used in Present and Future Neutrino Detectors”. PhD thesis. Technical University of Munich, 2015.

[57] T. Marrodán Undagoitia. “Measurement of light emission in organic liquid scintillators and studies towards the search for proton decay in the future large-scale detector LENA”. PhD thesis. Technical University of Munich, 2008.

[58] M. Kasha. “Characterization of electronic transitions in complex molecules”. In: *Discuss. Faraday. Soc.* 9, 14 19 (1950).

[59] R. Voltz and G Laustriat. “Radioluminescence des milieux organiques”. In: *J. Phys. France.* 29 (1968). 10.1051/JPhys:01968002902-3015900.

[60] L. Urbán *et al. GEANT4 Ionization class.* URL: https://geant4-userdoc.web.cern.ch/UsersGuides/PhysicsReferenceManual/html/electromagnetic/electron_incident/ionisation/eion.html#continuous-energy-loss (visited on 10/11/2024).

[61] M.J. Martin and S.M. Seltzer. “Tables of Energy Losses and Ranges of Electrons and Positrons”. In: *Nat. Acad. Sci. -Natl. Res. Council Publ.* 1133 (1964).

[62] J. Sawatzki. “Sensitivity Study of the Neutrino Mass Hierarchy Determination in JUNO Using Reactor Antineutrinos”. Master thesis. Technical University of Munich, 2014.

[63] Stephen M. Seltzer and Martin J. Berger. “Improved procedure for calculating the collision stopping power of elements and compounds for electrons and positrons”. In: *The International Journal of Applied Radiation and Isotopes* 35.7 (1984), pp. 665–676. ISSN: 0020-708X. https://doi.org/10.1016/0020-708X(84)90113-3. URL: https://www.sciencedirect.com/science/article/pii/0020708X84901133.

[64] D. Adey et al. “A high precision calibration of the nonlinear energy response at Daya Bay”. In: *Nuclear Instruments and Methods in Physics Research Section A: Accelerators, Spectrometers, Detectors and Associated Equipment* 940 (2019), pp. 230–242. ISSN: 0168-9002. https://doi.org/10.1016/j.nima.2019.06.031. URL: https://www.sciencedirect.com/science/article/pii/S016890021930871X.

[65] K. Schweizer. “Determination of the Nonlinearity Parameter for LAB-based Liquid Scintillators”. Master thesis. Technical University of Munich, 2017.

[66] Chen-Kai Qiao, Jian-Wei Wei, and Lin Chen. “An Overview of the Compton Scattering Calculation”. In: *Crystals* 11.5 (2021). ISSN: 2073-4352. 10.3390/cryst11050525. URL: https://www.mdpi.com/2073-4352/11/5/525.

[67] Marc André Tippmann. “Comprehensive photosensor research for large liquid scintillator neutrino detectors”. en. PhD thesis. Technische Universität München, 2021, p. 855. URL: https://mediatum.ub.tum.de/1611529.

[68] D. Dörflinger. “High Precision Measurement of Proton Recoil Quenching Factors in Liquid Scintillators”. Master thesis. Technical University of Munich, 2023.

[69] N. Y. Kim and G. Kim. “Measurement of the Compton-electron Response in Liquid Scintillator”. In: *Transactions of the Korean Nuclear Society Virtual Autumn Meeting* (Oct. 2021).

[70] H. Wan Chan Tseung, J. Kaspar, and N. Tolich. “Measurement of the dependence of the light yields of linear alkylbenzene-based and EJ-301 scintillators on electron energy”. In: *Nuclear Instruments and Methods in Physics Research Section A: Accelerators, Spectrometers, Detectors and Associated Equipment* 654.1 (2011), pp. 318–323. ISSN: 0168-9002. https://doi.org/10.1016/j.nima.2011.06.095. URL: https://www.sciencedirect.com/science/article/pii/S0168900211013908.

[71] C Aberle et al. “Light output of Double Chooz scintillators for low energy electrons”. In: *Journal of Instrumentation* 6.11 (Nov. 2011), P11006. 10.1088/1748-0221/6/11/P11006. URL: https://dx.doi.org/10.1088/1748-0221/6/11/P11006.

[72] Belina von Krosigk. “Measurement of proton and α–particle quenching in LAB based scintillators and determination of spectral sensitivities to supernova neutrinos in the SNO+ detector”. en. PhD thesis. Technische Universität Dresden, 2015. URL: https://snoplus.phy.queensu.ca/theses/bvk.pdf.

[73] C Aberle et al. “Large scale Gd-beta-diketonate based organic liquid scintillator production for antineutrino detection”. In: *Journal of Instrumentation* 7.06 (June 2012), P06008. 10.1088/1748-0221/7/06/P06008. URL: https://dx.doi.org/10.1088/1748-0221/7/06/P06008.

[74] S. Westerdale et al. “Quenching measurements and modeling of a boron-loaded organic liquid scintillator”. In: *Journal of Instrumentation* 12.08 (Aug. 2017), P08002. 10.1088/1748-0221/12/08/P08002. URL: https://dx.doi.org/10.1088/1748-0221/12/08/P08002.

[75] Raphael Matthias Stock. “Development and Characterization of Novel Liquid Scintillators for the Detection of Neutrinos In Large Volume Detectors”. en. PhD thesis. Technische Universität München, 2024. URL: https://mediatum.ub.tum.de/???.

[76] D. Basilico et al. “Final results of Borexino on CNO solar neutrinos”. In: *Phys. Rev. D* 108 (10 Nov. 2023), p. 102005. 10.1103/PhysRevD.108.102005. URL: https://link.aps.org/doi/10.1103/PhysRevD.108.102005.

[77] P. Lombardi and et al. “Distillation and stripping pilot plants for the JUNO neutrino detector: Design, operations and reliability”. In: *Nuclear Instruments and Methods in Physics Research Section A: Accelerators, Spectrometers, Detectors and Associated Equipment* 925 (2019), pp. 6–17. ISSN: 0168-9002. https://doi.org/10.1016/j.nima.2019.01.071. URL: https://www.sciencedirect.com/science/article/pii/S0168900219301299.

[78] Zhihang Zhu et al. “Optical purification pilot plant for JUNO liquid scintillator”. In: *Nuclear Instruments and Methods in Physics Research Section A: Accelerators, Spectrometers, Detectors and Associated Equipment* 1048 (2023), p. 167890. ISSN: 0168-9002. https://doi.org/10.1016/j.nima.2022.167890. URL: https://www.sciencedirect.com/science/article/pii/S0168900222011822.

[79] Jiaxuan Ye and et al. “Development of water extraction system for liquid scintillator purification of JUNO”. In: *Nuclear Instruments and Methods in Physics Research Section A: Accelerators, Spectrometers, Detectors and Associated Equipment* 1027 (2022), p. 166251. ISSN: 0168-9002. https://doi.org/10.1016/j.nima.2021.166251. URL: https://www.sciencedirect.com/science/article/pii/S016890022101086X.

[80] F. P. An *et al. New measurement of θ_{13} via neutron capture on hydrogen at Daya Bay*. 2016. arXiv: 1603.03549.

[81] J. Liu et al. “Automated calibration system for a high-precision measurement of neutrino mixing angle $\vartheta 13$ with the Daya Bay antineutrino detectors”. In: *Nuclear Instruments and Methods in Physics Research Section A: Accelerators, Spectrometers, Detectors and Associated Equipment* 750 (2014), pp. 19–37. ISSN: 0168-9002. https://doi.org/10.1016/j.nima.2014.02.049. URL: https://www.sciencedirect.com/science/article/pii/S0168900214002332.

[82] V. Hejny, M. Hartmann, and A. Mussgiller. “RootSorter: A New Analysis Framework for ANKE”. In: (2002).

[83] ROOT Analysis Framework Webpage. URL: http://root.cern.ch/ (visited on 10/19/2017).

[84] N. Matthew and R. Stones. *Beginning Linux Programming*. Wiley, 2011. ISBN: 9781118058619. URL: https://books.google.de/books?id=vvuzDziOMeMC.

[85] Javier Serrano et al. “THE WHITE RABBIT PROJECT”. In: 2009. URL: https://api.semanticscholar.org/CorpusID:54113364.

[86] Abraham. Savitzky and M. J. E. Golay. “Smoothing and Differentiation of Data by Simplified Least Squares Procedures.” In: *Analytical Chemistry* 36.8 (1964), pp. 1627–1639. 10.1021/ac60214a047. eprint: https://doi.org/10.1021/ac60214a047. URL: https://doi.org/10.1021/ac60214a047.

[87] “Top 10 Articles.” In: *Analytical Chemistry* 72.9 (2000), 324 A–329 A. 10.1021/ac002801q. eprint: https://doi.org/10.1021/ac002801q. URL: https://doi.org/10.1021/ac002801q.

[88] Elisabeth Neuerburg. “Event Reconstruction in OSIRIS”. en. Rheinisch-Westfälische Technische Hochschule (RWTH) Aachen, 2024. URL: https://www.institut3b.physik.rwth-aachen.de/global/show_document.asp?id=aaaaaaaacmzuzax.

[89] E. Margaret Burbidge et al. “Synthesis of the Elements in Stars”. In: *Rev. Mod. Phys.* 29 (4 Oct. 1957), pp. 547–650. 10.1103/RevModPhys.29.547. URL: https://link.aps.org/doi/10.1103/RevModPhys.29.547.

[90] M. de Bruin. In: *Pure and Applied Chemistry* 54.8 (1982), pp. 1533–1554. doi:10.1351/pac198254081533. URL: https://doi.org/10.1351/pac198254081533.

[91] U.S. Geological Survey. *Uranium*. URL: https://pubs.usgs.gov/of/2004/1050/uranium.htm (visited on 10/02/2024).

[92] U.S. Geological Survey. *Thorium*. URL: https://pubs.usgs.gov/of/2004/1050/thorium.htm (visited on 10/02/2024).

[93] L. Niedermeier. “High Efficiency Purification of Liquid Scintillators for the Solar Neutrino Experiment Borexino”. PhD thesis. Technical University of Munich, 2005.

[94] G. Alimonti et al. “The liquid handling systems for the Borexino solar neutrino detector”. In: *Nuclear Instruments and Methods in Physics Research Section A: Accelerators, Spectrometers, Detectors and Associated Equipment* 609.1 (2009), pp. 58–78. ISSN: 0168-9002. https://doi.org/10.1016/j.nima.2009.07.028. URL: https://www.sciencedirect.com/science/article/pii/S0168900209014247.

[95] H.O. Back et al. “Pulse-shape discrimination with the Counting Test Facility”. In: *Nuclear Instruments and Methods in Physics Research Section A: Accelerators, Spectrometers, Detectors and Associated Equipment* 584.1 (2008), pp. 98–113. ISSN: 0168-9002. https://doi.org/10.1016/j.nima.2007.09.036. URL: https://www.sciencedirect.com/science/article/pii/S0168900207020761.

[96] B. Philhour et al. “Simulations of pulse shape discrimination (PSD) techniques for background reduction in germanium detectors”. In: *Nuclear Instruments and Methods in Physics Research Section A: Accelerators, Spectrometers, Detectors and Associated Equipment* 403.1 (1998), pp. 136–150. ISSN: 0168-9002. https://doi.org/10.1016/S0168-9002(97)01071-1. URL: https://www.sciencedirect.com/science/article/pii/S0168900297010711.

[97] Willem G. J. Langeveld et al. “Pulse Shape Discrimination Algorithms, Figures of Merit, and Gamma-Rejection for Liquid and Solid Scintillators”. In: *IEEE Transactions on Nuclear Science* 64.7 (2017), pp. 1801–1809. 10.1109/TNS.2017.2681654.

[98] D. Basilico et al. “Optimized α/β pulse shape discrimination in Borexino”. In: *Phys. Rev. D* 109 (11 June 2024), p. 112014. 10.1103/PhysRevD.109.112014. URL: https://link.aps.org/doi/10.1103/PhysRevD.109.112014.

[99] S. Dutta et al. “Pulse shape simulation and discrimination using machine learning techniques”. In: *Journal of Instrumentation* 18.03 (Mar. 2023), P03038. 10.1088/1748-0221/18/03/P03038. URL: https://dx.doi.org/10.1088/1748-0221/18/03/P03038.

[100] E Gatti and F De Martini. *A new linear method of discrimination between elementary particles in scintillation counters; Nouvelle methode lineaire de discrimination entre particules elementaires dans des compteurs a scintillation; Novyj linejnyj metod diskriminatsii ehlementarnykh chastits v stsintillyatsionnykh schetchikakh; Nuevo metodo lineal de discriminacion entre particulas elementales en contadores de centelleo*. Apr. 1962.

[101] R.F. Lang et al. “Improved pulse shape discrimination in EJ-301 liquid scintillators”. In: *Nuclear Instruments and Methods in Physics Research Section A: Accelerators, Spectrometers, Detectors and Associated Equipment* 856 (2017), pp. 26–31. ISSN: 0168-9002. https://doi.org/10.1016/j.nima.2017.02.090. URL: https://www.sciencedirect.com/science/article/pii/S0168900217303133.

[102] H.S. Zhang et al. “Refractive index in the JUNO liquid scintillator”. In: *Nuclear Instruments and Methods in Physics Research Section A: Accelerators, Spectrometers, Detectors and Associated Equipment* 1068 (2024), p. 169730. ISSN: 0168-9002. https://doi.org/10.1016/j.nima.2024.169730. URL: https://www.sciencedirect.com/science/article/pii/S0168900224006569.

[103] X. Li and et al. “Timing properties and pulse shape discrimination of LAB-based liquid scintillator”. In: *Chinese Physics C* 35.11 (Nov. 2011), p. 1026. 10.1088/1674-1137/35/11/009. URL: https://dx.doi.org/10.1088/1674-1137/35/11/009.

[104] J. Cheng et al. “Pulse shape discrimination technique for diffuse supernova neutrino background search with JUNO”. In: *Eur. Phys. J. C* 84.482 (May 2024). 10.1140/epjc/s10052-024-12779-6. URL: https://doi.org/10.1140/epjc/s10052-024-12779-6.

[105] E. Bellotti et al. “Precise measurement of the 222Rn half-life: A probe to monitor the stability of radioactivity”. In: *Physics Letters B* 743 (2015), pp. 526–530. ISSN: 0370-2693. https://doi.org/10.1016/j.physletb.2015.03.021. URL: https://www.sciencedirect.com/science/article/pii/S0370269315001847.

[106] Hans Theodor Josef Steiger. “Development of a low level radioactive liquid scintillator and of the detector monitoring system for the JUNO neutrino experiment”. en. PhD thesis. Technische Universität München, 2020, p. 211. URL: https://mediatum.ub.tum.de/1539429.

[107] M. Wurm. *Private communication*. Private communication. Oct. 2024.

[108] JUNO. *Private communication*. Private communication. Oct. 2024.

[109] Marianne Göger-Neff. “Development of a liquid scintillator and of data analysis methods for BOREXINO”. en. PhD thesis. Technische Universität München, 2001, p. 135. URL: https://mediatum.ub.tum.de/602872.

[110] C. Arpesella et al. “First real time detection of 7Be solar neutrinos by Borexino”. In: *Physics Letters B* 658.4 (2008), pp. 101–108. ISSN: 0370-2693. https://doi.org/10.1016/j.physletb.2007.09.054. URL: https://www.sciencedirect.com/science/article/pii/S0370269307011732.

[111] Michael Franke. “The neutrino experiment Double Chooz and data analysis with the near detector”. en. PhD thesis. Technische Universität München, 2016, p. 154. URL: https://mediatum.ub.tum.de/1291361.

[112] M. Shamsuzzoha Basunia. “Nuclear Data Sheets for A = 210”. In: *Nuclear Data Sheets* 121 (2014), pp. 561–694. ISSN: 0090-3752. https://doi.org/10.1016/j.nds.2014.09.004. URL: https://www.sciencedirect.com/science/article/pii/S0090375214006589.

[113] K. Murray Matthews, Chang-Kyu Kim, and Paul Martin. “Determination of 210Po in environmental materials: A review of analytical methodology”. In: *Applied Radiation and Isotopes* 65.3 (2007), pp. 267–279. ISSN: 0969-8043. https://doi.org/10.1016/j.apradiso.2006.09.005. URL: https://www.sciencedirect.com/science/article/pii/S0969804306003290.

[114] T. Araki et al. “Measurement of Neutrino Oscillation with KamLAND: Evidence of Spectral Distortion”. In: *Phys. Rev. Lett.* 94 (8 Mar. 2005), p. 081801. 10.1103/PhysRevLett.94.081801. URL: https://link.aps.org/doi/10.1103/PhysRevLett.94.081801.

[115] Benda Xu. “Observation of Geoneutrinos at KamLAND during Reactor Shutdown”. In: 2014. URL: https://api.semanticscholar.org/CorpusID:124133953.

[116] S. Abe et al. “Precision Measurement of Neutrino Oscillation Parameters with KamLAND”. In: *Phys. Rev. Lett.* 100 (22 June 2008), p. 221803. 10.1103/PhysRevLett.100.221803. URL: https://link.aps.org/doi/10.1103/PhysRevLett.100.221803.

Acknowledgements

Last but certainly not least, I want to thank everyone who made this thesis possible.

First of all, I want to express my gratitude to my professor, Lothar Oberauer, who gave me the opportunity to pursue this research. Thank you, Lothar, for always believing in me, especially when the times were tough!

I want to thank my group, current and former members, for supporting me, for valuable discussions and input, and for creating a great work atmosphere; in no particular order: Simon Appel, Birgit Neumair, Marc Tippmann, Raphael Stock, Ulrike Fahrendholz, Julia Sawatzki, Meishu Lu, Matthias Maier, Dominik Jeschke, Jan Plössner, Korbinian Stangler, Vincent Rompel, David Dörflinger, Selina Rudolph, Sara Braun, Lennard Kayser, Elias Fischer, Simon Csakli, Luca Schweizer. In particular, thank you to my office colleagues for making good and bad times better! Special thanks to Ulrike for proofreading this work.

To my other group, the OSIRIS gang, thank you so much for immediately making me feel welcome! To Prof. Michael Wurm for letting me be a part of the project. Kai Loo, thank you for helping me find my way around the RootSorter, for always listening, and for the great support. Philipp Kampmann for teaching me the basics. Arshak Jafar, Tobias Sterr, Rosmarie Wirth, Cornelius Vollbrecht, Lukas Bieger, Oliver Pilarczyk, and Meishu for the memes, for suffering together through the commissioning of the detector, the conversations, and the great atmosphere!

Thank you to the whole E15 for being a great workplace. Special thanks to Paola Mucciarelli and Sabine Wenzel for helping with all the administrative things and always finding a way to make things possible and easier for me.

I thank Prof. Stefan Schönert for letting me be a part of this chair.

I was lucky enough to also find friends among my coworkers. Thank you, Simon, for teaching me the way of the coffee, tolerating my frustrated sighs, and helping whenever necessary. Thank you to the horror game group, (Cr)andi, (L)andi, Cristoph, and Moritz for always listening, having someone to rant, and being good friends. Special thanks to Andi L. for being a sunshine in my life!

I also must endeavor to convey my gratitude to my gracious friend Andrej Lier for prospecting for the blemishes of half of this thesis in a minuscule measure of time, even though it possesses zero literary substance. ;-)

A big thank you to my family: my mother, Benni, Happi, Peli, and Lisi. Thank you for helping me through tough times, having many laughs together, and tolerating my lack of responses. Stay awesome, and I love you guys!

Lastly, thank you to my amazing girlfriend! Thank you, Rita, for always being there for me, for supporting me in every way possible, for listening to my rants and overly long and complicated stories, and for singing with me! Thank you for being you! Спасибо, моя Любовь!